

Jian Wang

From local to global:  
Complex behavior of spatiotemporal systems  
with fluctuating delay times



Jian Wang

**From local to global:  
Complex behavior of spatiotemporal systems  
with fluctuating delay times**



TECHNISCHE UNIVERSITÄT  
CHEMNITZ

**Universitätsverlag Chemnitz**  
2014

## **Impressum**

### **Bibliografische Information der Deutschen Nationalbibliothek**

Die Deutsche Nationalbibliothek verzeichnet diese Publikation in der Deutschen Nationalbibliografie; detaillierte bibliografische Angaben sind im Internet über <http://dnb.d-nb.de> abrufbar.

Zugl.: Chemnitz, Techn. Univ., Diss., 2014

Technische Universität Chemnitz/Universitätsbibliothek

**Universitätsverlag Chemnitz**

09107 Chemnitz

<http://www.bibliothek.tu-chemnitz.de/UniVerlag/>

### **Herstellung und Auslieferung**

Verlagshaus Monsenstein und Vannerdat OHG

Am Hawerkamp 31

48155 Münster

<http://www.mv-verlag.de>

ISBN 978-3-944640-11-2

<http://nbn-resolving.de/urn:nbn:de:bsz:ch1-qucosa-133734>

**From local to global:  
Complex behavior of spatiotemporal systems  
with fluctuating delay times**

von der Fakultät für Naturwissenschaften  
der Technischen Universität Chemnitz  
genehmigte Dissertation zur Erlangung des akademischen Grades  
doctor rerum naturalium  
(Dr. rer. nat.)

vorgelegt von M. Sc. Jian Wang  
geboren am 17.05.1982 in Shanghai, V.R. China  
eingereicht am 16.08.2013

Gutachter:  
Prof. Dr. Günter Radons  
Prof. Dr. Karl Heinz Hoffmann

Tag der Verteidigung: 05.02.2014



---

## Bibliografische Beschreibung

Wang, Jian

**From local to global: Complex behavior of spatiotemporal systems with fluctuating delay times**

Technische Universität Chemnitz, Fakultät für Naturwissenschaften

Dissertation (in englischer Sprache), 2013

115 Seiten, 83 Abbildungen, 58 Literaturzitate

## Referat

Ziel der vorliegenden Arbeit ist die Untersuchung der Einflüsse der zeitlich fluktuierenden Verzögerungen in räumlich ausgedehnten diffusiven Systemen. Durch den Vergleich von Systemen mit konstanter Verzögerung bzw. Systemen ohne räumliche Kopplung erhält man ein tieferes Verständnis und eine bessere Beschreibungsweise der Dynamik des räumlich ausgedehnten diffusiven Systems mit fluktuierenden Verzögerungen.

Im ersten Teil werden diskrete Systeme in Form von diffusiven Coupled Map Lattices untersucht. Als die lokale iterierte Abbildung des betrachteten Systems wird die logistische Abbildung mit Verzögerung gewählt. In diesem Teil liegt der Fokus auf Musterbildung, Existenz von Multiattraktoren und laufenden Wellen sowie der Möglichkeit der vollen Synchronisation. Masterstabilitätsfunktion, Lyapunov Exponent und Spektrumsanalyse werden benutzt, um das dynamische Verhalten zu verstehen.

Im zweiten Teil betrachten wir kontinuierliche Systeme. Hier wird die Fisher-KPP Gleichung mit Verzögerungen im Reaktionsteil untersucht. In diesem Teil liegt der Fokus auf der Existenz der Turing Instabilität. Mit Hilfe von analytischen und numerischen Berechnungen wird gezeigt, dass bei fluktuierenden Verzögerungen eine Turing Instabilität auch in 1-Komponenten-Reaktions-Diffusionsgleichungen gefunden werden kann.

## Schlagworte

Reaktions-Diffusionsgleichung, Coupled Map Lattice, Hutchinson Gleichung, Fisher-KPP Gleichung, logistische Abbildung with Verzögerung, Systeme mit fluktuierenden Verzögerungen, Musterbildung, Synchronisation, Stabilitätsanalyse, Masterstabilitätsfunktion, Multiattraktor, Turing Instabilität, laufende Wellen.





---

## Abstract

The aim of this thesis is to investigate the dynamical behaviors of spatially extended systems with fluctuating time delays. In recent years, the study of spatially extended systems and systems with fluctuating delays has experienced a fast growth. In ubiquitous natural and laboratory situations, understanding the action of time-delayed signals is a crucial for understanding the dynamical behavior of these systems. Frequently, the length of the delay is found to change with time. Spatially extended systems are widely studied in many fields, such as chemistry, ecology, and biology. Self-organization, turbulence, and related nonlinear dynamic phenomena in spatially extended systems have developed into one of the most exciting topics in modern science.

The first part of this thesis considers the discrete system. Diffusively coupled map lattices with a fluctuating delay are used in the study. The uncoupled local dynamics of the considered system are represented by the delayed logistic map. In particular, the influences of diffusive coupling and fluctuating delay are studied. To observe and understand the influences, the results for the considered system are compared with coupled map lattices without delay and with a constant delay as well as with the uncoupled logistic map with fluctuating delays. Identifying different patterns, determining the existence of traveling wave solutions, and specifying the fully synchronized stable state are the focus of this part of the study. The Lyapunov exponent, the master stability function, spectrum analysis, and the structure factor are used to characterize the different states and the transitions between them.

The second part examines the continuous system. The delay is introduced into the reaction-term of the Fisher-KPP equation. The focus of this part of study is the time-delay-induced Turing instability in one-component reaction-diffusion systems. Turing instability has previously only been found in multiple-component reaction-diffusion systems. However, this work demonstrates with the help of the stability exponent that fluctuating delay can result in Turing instability in one-component reaction-diffusion systems as well.

**Key Words:** Reaction-diffusion system, coupled map lattice, delayed logistic map, system with fluctuating delays, Hutchinson's equation, Fisher-KPP equation, pattern formation, synchronization, master stability function, multiattractor, Turing instability, traveling wave solution.



# Contents

<b>1</b>	<b>Introduction</b>	<b>13</b>
1.1	Motivation . . . . .	13
1.2	Model . . . . .	14
<b>2</b>	<b>Physical and Mathematical Backgrounds</b>	<b>17</b>
2.1	Mathematical tools . . . . .	17
2.1.1	Lyapunov exponent . . . . .	17
2.1.2	Structure factor . . . . .	18
2.1.3	Window function . . . . .	19
2.1.4	Master stability function . . . . .	21
2.2	Dynamic properties of the basic systems . . . . .	23
2.2.1	Hutchinson's equation . . . . .	23
2.2.2	Delayed logistic map . . . . .	26
2.3	Dynamics of spatially extended systems . . . . .	29
2.3.1	Turing instability . . . . .	30
2.3.2	Traveling wave solutions . . . . .	34
<b>3</b>	<b>Coupled Map Lattices</b>	<b>37</b>
3.1	Coupled map lattices without delay and with constant delay . . . . .	37
3.1.1	Coupled map lattice without delay . . . . .	37
3.1.2	Coupled map lattice with constant delay . . . . .	49
3.2	Analysis of the bifurcation point shift . . . . .	54
3.3	Coupled map lattices with fluctuating delay . . . . .	62
3.3.1	Synchronized periodic delay . . . . .	62
3.3.2	Nonsynchronized periodic delay . . . . .	78
<b>4</b>	<b>Partial Differential Equations</b>	<b>83</b>
4.1	Necessary conditions for Turing instability . . . . .	83

4.2	Influence of fluctuating delay in ODE's . . . . .	84
4.3	Linear stability analysis for PDE's . . . . .	89
4.3.1	General form and linear stability analysis for stable equilibria . . .	90
4.3.2	Linear stability analysis for the Fisher-KPP equation with delay . .	93
4.4	Results for PDEs . . . . .	95
4.4.1	Step-shaped delay with $\tau_1 = 1$ , $\tau_2 = 2$ , $T_p = 2$ , and $T_1 = 1$ . . . . .	95
4.4.2	Step-shaped delay with $\tau_1 = 1$ , $\tau_2 = 2$ , $T_p = 20$ , and $T_1 = 10$ . . . .	103
4.4.3	Sine-shaped delay with $\tau_M = 1.5$ , $\tau_A = 0.5$ , and $\omega = \pi$ . . . . .	105
4.4.4	Sine-shaped delay with $\tau_M = 1.5$ , $\tau_A = 0.5$ , and $\omega = \frac{1}{\pi}$ . . . . .	107
<b>5</b>	<b>Summary and Outlook</b>	<b>111</b>

# 1 Introduction

## 1.1 Motivation

The study of spatially extended systems and the study of delay systems are two advancing fronts in nonlinear science. Both the spatial extension and the time delay of a signal can influence the system dynamics and make the system more complicated. Hence the study of such systems is of great interest. For instance, the time-delay systems used to model retarded actions are relevant in many fields, such as optics [1], machining [2–5], biology, or physiology [6, 7]. And for spatially extended systems, the self-organization of patterns and structures under far-from-equilibrium conditions, turbulence, and other related nonlinear dynamic phenomena, can occur in a wide variety of different fields. Consider, for instance, the chemical and biological patterns in reaction-diffusion systems, vortex formation in connection with chemical, optical, hydrodynamic, or magnetohydrodynamic turbulence and technical applications in connection with liquid crystal displays or pulse compression in optical communication systems [8, 9]. The study of these phenomena is one of the most exciting topics in modern science. In recent years, the study of composed systems has become more common, for instance, studying networks with delayed feedback [10–12], the existence of traveling waves in the presence of time-delay in spatially extended systems [13, 14], and the pattern dynamics in reaction-diffusion systems with time delay [15, 16].

In the last several years, the research of our group has focused on dynamical systems with temporally fluctuating delay, systems ranging from discrete iterated maps to ordinary differential equations [17–22]. The findings suggest that due to the fluctuating delay times, complex behavior will appear in these systems. The stability of a system can not only be strengthened but also weakened by fluctuating delay. Due to the fluctuating delays, a part of the Lyapunov spectrum becomes equal to negative infinity and leads to a dimension collapse [20]. The temporal behavior of the dimension collapse and its dependence on the system

parameters are complex. For example, in a simple map system with a delay fluctuating between two values, the parity of the difference between the two delay values determines the collapsed dimension. Going one step further, the complex behavior of spatially extended systems with fluctuating delay times is investigated. The influence of fluctuating delay times on, for instance global stability, multiple attractors, pattern formations, spatial non-localization, etc., are studied. The analysis of stability characteristics provides important information on the system dynamics.

## 1.2 Model

The considered system is based on a typical partial differential equation

$$\frac{\partial u(x,t)}{\partial t} = f(u(x,t)) + D\Delta u(x,t), \quad (1.1)$$

where  $x$  and  $t$  are time and space variables, respectively. In such systems, there is a local reaction term  $f(u)$  and a spatially diffusive coupling term  $D\Delta u$ , with the diffusion coefficient  $D$ , resulting in a so-called reaction-diffusion equation. When the diffusion coefficient  $D = 0$ , the system reduces to an ordinary differential system, in which a time delay was introduced and which has been investigated for a long time. The general form of the system considered in this thesis is

$$\frac{\partial u(x,t)}{\partial t} = f(u(x,t), u(x, t - \tau(t))) + D\Delta u(x,t), \quad (1.2)$$

where  $\tau(t)$  is the temporally fluctuating time delay. In particular, here the famous Hutchinson's equation

$$\dot{u}(t) = au(t)(1 - u(t - \tau)) \quad (1.3)$$

is used as an example for the reaction term. This equation was introduced by Hutchinson [23] as an ecological model. It is also referred to as the delayed logistic equation. So the continuous model studied here has the form

$$\frac{\partial u(x,t)}{\partial t} = au(x,t)(1 - u(x,t - \tau(t))) + D\Delta u(x,t). \quad (1.4)$$

The case with a time delay of  $\tau = 0$  is the famous Fisher-KPP equation [24, 25]. The Fisher-KPP equation is one of the simplest models of a nonlinear reaction-diffusion equation. It was introduced by Fisher in 1927 as a model of species diffusion and has also been used later to study the propagation of flames and nuclear reactors.

For the discrete system studied in this thesis, a coupled map lattice with the form

$$u_{n+1}^i = f(u_n^i) + D(u_n^{i+1} + u_n^{i-1} - 2u_n^i) \quad (1.5)$$

is used, and the delay is introduced into the reaction function  $f$ . Note that the diffusive coupling here is different from the form proposed in [26] by Kaneko

$$u_{n+1}^i = (1 - \varepsilon)f(u_n^i) + \frac{\varepsilon}{2}(f(u_n^{i+1}) + f(u_n^{i-1})), \quad (1.6)$$

where  $\varepsilon = \frac{D}{2}$ .

A simple model, which is used here, is the delayed logistic map

$$u_{n+1} = f(u_n, u_{n-T}) = au_n(1 - u_{n-T}). \quad (1.7)$$

This model was chosen because it can be viewed as the discretization of the continuous model in Eq.(1.4).

Assume a system

$$\frac{\partial u(x,t)}{\partial t} = g(u(x,t), u(x,t - \tau)) + D\Delta u(x,t). \quad (1.8)$$

The simplest method to simulate the partial differential equation numerically is the FTCS (Forward-Time Central-Space) method. It is a finite difference method based on central difference in space and the forward Euler method in time. For a general reaction-diffusion equation (1.1) in one dimension, one can derive the following equation via FTCS:

$$\frac{u_j^{n+1} - u_j^n}{\Delta t} = g(u_j^n, u_j^{n-T}) + D\left[\frac{u_{j+1}^n - 2u_j^n + u_{j-1}^n}{(\Delta x)^2}\right]. \quad (1.9)$$

## 1.2. MODEL

---

Here  $n$  is the index of the temporal discretization and  $j$  is the index of the spatial discretization.  $\Delta t$  and  $\Delta x$  are the step sizes for time and space, respectively, and  $T = \tau/\Delta t$ . For reaction-diffusion systems, the FTCS method gives first-order convergence in time  $\Delta t$  and second-order convergence in space  $\Delta x$  and is conditionally stable. Eq.(1.9) can be rewritten as a coupled map lattice

$$u_j^{n+1} = u_j^n + \Delta t g(u_j^n, u_j^{n-\tau}) + \frac{D\Delta t}{(\Delta x)^2} (u_{j+1}^n + u_{j-1}^n - 2u_j^n), \quad (1.10)$$

which has the same form as Eq.(1.5). With such models, one has only one nonlinear delay term in the system. And it is relatively easy to investigate and understand the influence of delay in the discrete models, Eq.(1.10).



## 2 Physical and Mathematical Backgrounds

This chapter explains the physical and mathematical backgrounds that are important for the current study. For instance, the considered spatio-temporal system consists of a local process and spatial coupling. Thus, understanding the dynamic behaviors of local processes is necessary. Some mathematical tools are introduced for investigating and understanding dynamic behaviors.

### 2.1 Mathematical tools

#### 2.1.1 Lyapunov exponent

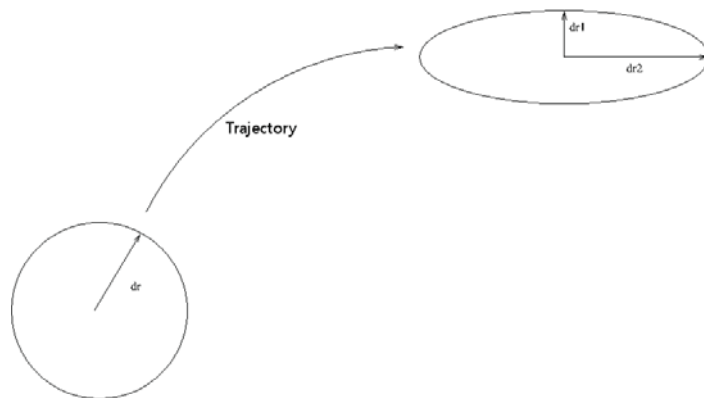


Figure 2.1: Schematic diagram for Lyapunov exponent: the evolution of a circle after several iterations.

## 2.1. MATHEMATICAL TOOLS

---

The Lyapunov exponent of a dynamical system, an exponent which is named after A.M. Lyapunov [27], is a quantity that characterizes the rate at which two slightly different trajectories in phase space separate from each other. Quantitatively, two trajectories in phase space with an initial separation  $\delta\mathbf{Z}_0$  diverge exponentially at a rate

$$\lambda = \lim_{t \rightarrow \infty} \frac{1}{t} \ln \frac{|\delta\mathbf{Z}(t)|}{|\delta\mathbf{Z}_0|}, \quad (2.1)$$

where  $\lambda$  is the Lyapunov exponent.

For high-dimensional systems the rate  $\lambda$  can be different for different orientations of the initial separation vector  $\delta\mathbf{Z}_0$  (see Fig.2.1). Thus, there is a spectrum of Lyapunov exponents, with the total number equal to the dimension of the phase space. It is common to use the largest exponent in the spectrum, the Maximal Lyapunov exponent (MLE), to determine the stability of system.

- When the MLE is positive, the neighboring trajectories will separate exponentially and the system is chaotic.
- When it is negative, the system has a stable stationary state or a periodic state.
- When it is zero, limit cycles or a quasiperiodic orbit can be obtained.

### 2.1.2 Structure factor

The consideration of spatially extended systems requires the classification of the different type of spatio-temporal structures. One mathematical tool for achieving this is the structure factor. Originally, the structure factor was used in condensed matter physics and crystallography to describe how a material scatters incident radiation [28, 29].

There are two types of structure factors. One is the static structure factor, which is measured without resolving the energy of the scattered particle, and is defined as the Fourier transformation of the scalar quantity. The other is the dynamic structure factor, which is used in the energy-resolved case. The structure factor is most often denoted as  $S(\vec{k}, \omega)$ , with wave vector  $\vec{k}$  and frequency  $\omega$ . The dynamic structure factor is defined as

$$S(\vec{k}, \omega) = \frac{1}{2\pi} \int_{-\infty}^{\infty} F(\vec{k}, t) e^{i\omega t} dt \quad (2.2)$$

Here  $F(\vec{k}, t)$  is the so-called intermediate scattering function, which is the spatial Fourier transform of the van Hove function  $G(\vec{r}, t)$  [30–32]

$$F(\vec{k}, t) = \int_{-\infty}^{\infty} G(\vec{r}, t) e^{-i\vec{k} \cdot \vec{r}} d\vec{r}. \quad (2.3)$$

As the spatio-temporal structure is studied in this thesis, a general form of the dynamic structure factor can be used to determine different spatio-temporal behavior: the two-dimensional Fourier transformation of the autocorrelation function. For a continuous system  $u(\vec{x}, t)$ , it reads

$$S(\vec{k}, \omega) = \int_{-\infty}^{\infty} \int_{-\infty}^{\infty} R_{uu}(\vec{r}, \tau) e^{-i\vec{k} \cdot \vec{r}} d\vec{r} e^{-i\omega \cdot \tau} d\tau, \quad (2.4)$$

where  $R_{uu}$  is the autocorrelation function with the form

$$R_{uu}(\vec{r}, \tau) = \lim_{a \rightarrow \infty} \lim_{b \rightarrow \infty} \int_{-a}^a dt \int_{-b}^b dx u(\vec{x}, t) u^*(\vec{x} - \vec{r}, t - \tau). \quad (2.5)$$

Note that there is a two-dimensional Fourier transformation in Eq.(2.4), whereas in Eq.(2.2) there is an inverse Fourier transformation. This difference can only influence the amplitude by a factor of  $\frac{1}{2\pi}$  and reverse the  $\omega$ -axis. It does not influence the determination of structures.

With the form in Eq.(2.4), the Wiener-Khinchin theorem can be applied to simplify the calculation: "The power spectral density of a wide-sense-stationary random process is the Fourier transformation of the corresponding autocorrelation function." [33, 34] The dynamic structure factor can be calculated as the power spectral density of the state function  $u(\vec{x}, t)$

$$S(\vec{k}, \omega) = \lim_{T \rightarrow \infty} \lim_{X \rightarrow \infty} \frac{1}{T} \frac{1}{X} \left| \int_{-T}^T \int_{-X}^X u(x, t) e^{-i\omega t} e^{-i\vec{k} \cdot \vec{x}} dt d\vec{x} \right|^2. \quad (2.6)$$

Different types of structures can present different dynamic spectrum factors. Some typical examples will be shown in Section 2.3

### 2.1.3 Window function

Since spectral analysis is used to determine the structure, numerical artifacts, such as the spectral leakage, will inevitably occur, interfering with my findings. Hence a window function is employed to alleviate this interference. Explained simply, a window function is a

mathematical function that is zero-valued outside some chosen interval. The Fourier transform is in general an integral in the interval from negative infinity to positive infinity. But in the actual spectrum analysis, it is only possible to choose a finite interval for the sample. Such a choice can be considered as the simplest example of the window function, the rectangular window, which is constant inside the chosen interval. For a periodic sample, only if the chosen interval is exactly an integral multiple of the period can the spectrum analysis with the rectangular window be exact. An example is shown in Fig.2.2. The signal considered is a cosine-shaped function with a frequency of 15. In the spectrum analysis, a signal peak is expected only at the frequency 15. One can see that with a window length of 2 (Fig.2.2(b)), the result coincides with the expected value. But for an arbitrary window length, there is leakage near the expected peaks (Fig.2.2(c)).

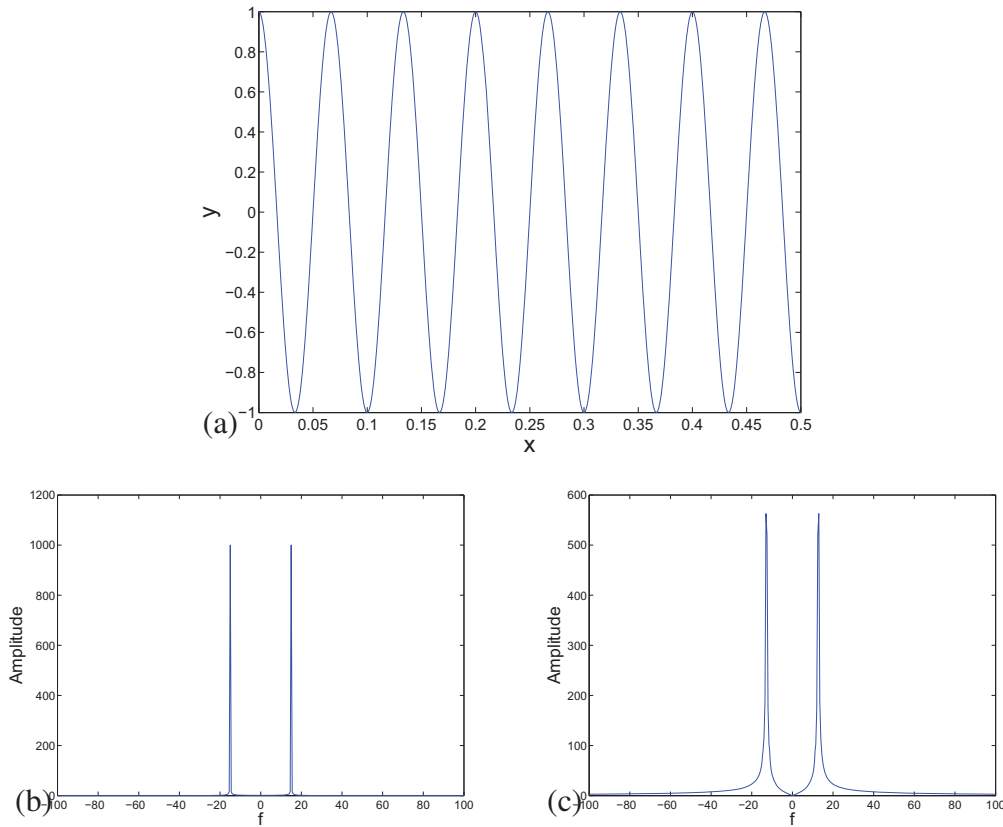


Figure 2.2: (a) The signal used,  $y(x) = \cos(30\pi x)$ , (b) the spectrum obtained by using a rectangular window within the interval  $[0, 2]$ , (c) the spectrum obtained by using a rectangular window within the interval  $[0, 1.7]$

In technical applications, most signals are complex, and it is not possible to ascertain the period. Under such conditions, the leakage can interfere with the measurements, leading to numerical artifacts. Hence different window functions have been proposed to reduce such interference. Two common examples are the Hamming window and Hann window. Both windows are in the family known as "raised cosine" or "generalized Hamming" windows. They are named respectively after Julius von Hann and Richard Hamming [35]. The Hamming window has the form

$$w(n) = 0.54 - 0.46 \cos\left(\frac{2\pi n}{N-1}\right). \quad (2.7)$$

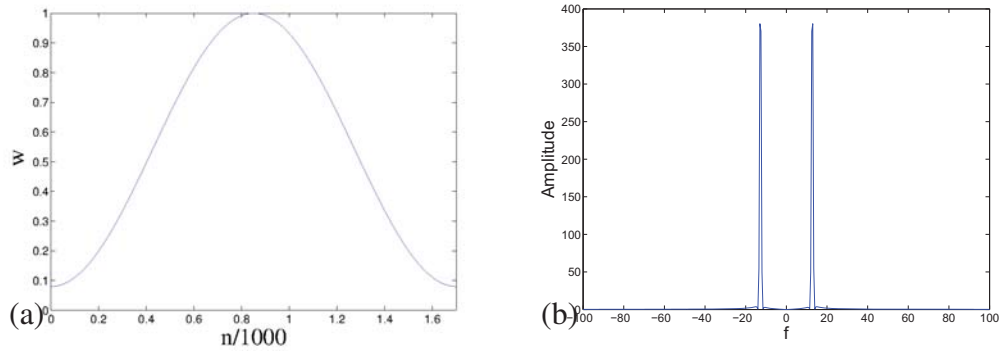


Figure 2.3: (a) Hamming window with  $N = 1700$ . (b) Spectrum analysis for  $y(x) = \cos(2\pi x)$  with the Hamming window in the interval  $[0, 1.7]$ .

And the Hann window has the form

$$w(n) = 0.5 \left( 1 - \cos\left(\frac{2\pi n}{N-1}\right) \right). \quad (2.8)$$

The two windows and their resulting spectra are shown, in Fig.2.3 and Fig.2.4 respectively. In comparison with Fig.2.2(c), one can see that with these window functions, the leakage can be effectively reduced in the spectrum analysis. In this work, these two window functions are used in most spectrum analyses.

### 2.1.4 Master stability function

The master stability function is a mathematical and physical tool for studying the problem of synchronous stability for any linear coupling of oscillators. It was first introduced by L.

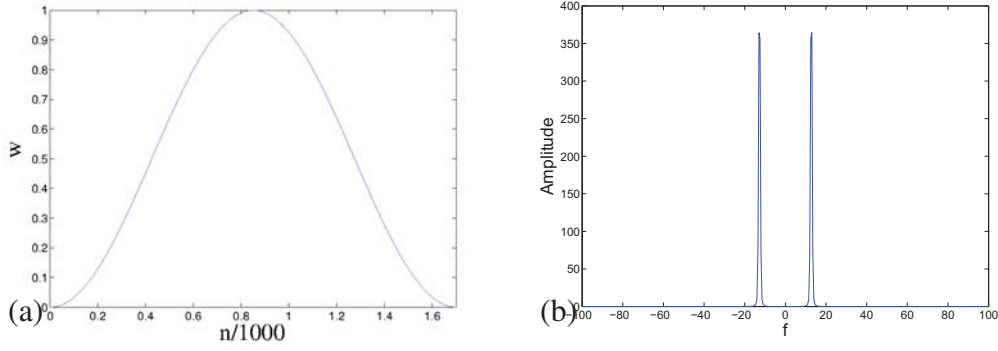


Figure 2.4: (a) Hann window with  $N = 1700$ . (b) Spectrum analysis for  $y(x) = \cos(2\pi x)$  with the Hann window in the interval  $[0, 1.7]$ .

M. Pecora and T. L. Carroll [36]. Since the coupled map lattice model used in this work can also be considered as a simple network system, the master stability function will be used to investigate the stability of some states with respect to the coupling.

In general, one considers a coupled  $N$ -node (oscillator) system with the form

$$\dot{x}^i = F(x^i) + \sigma \sum_j G_{ij} H(x^j). \quad (2.9)$$

Here  $x^i$  is the component of the  $m$ -dimensional vector of the dynamical variables corresponding to the  $i$ -th node.  $F(x^i)$  represents the dynamics of the uncoupled nodes and should be identical for each node.  $H : R^m \rightarrow R^m$  is an arbitrary function of node variables.  $G_{ij}$  are coupling coefficients that should satisfy  $\sum_j G_{ij} = 0$  so that the synchronization manifold is an invariant manifold. And  $\sigma$  is a coupling strength. The whole system can be rewritten as the vector form

$$\dot{x} = F(x) + \sigma G \otimes H(x). \quad (2.10)$$

Here the symbol  $\otimes$  denotes the direct product; the vectors are defined as

$$F(x) = [F(x^1), F(x^2), \dots, F(x^N)],$$

and

$$H(x) = [H(x^1), H(x^2), \dots, H(x^N)],$$

with

$$x = (x^1, x^2, \dots, x^N);$$

and  $G$  is the matrix of coupling coefficients  $\{G_{ij}\}$ . For the stability analysis, the linearized equation with a small perturbation  $\xi$  is considered,

$$\dot{\xi} = [I_N \otimes DF + \sigma G \otimes DH]\xi. \quad (2.11)$$

This equation can be used to calculate Lyapunov exponents. The first term in Eq.(2.11) is a block diagonal with  $m \times m$  blocks, and the second term can be transformed by diagonalizing  $G$ . Since the transformation only acts on the matrix  $I_N$ , it does not affect the first term. In this way, the Eq.(2.11) can be simplified and rewritten as a block-diagonalized differential equation, with each block having the form:

$$\dot{\xi}_k = [DF + \sigma \gamma_k DH]\xi_k, \quad (2.12)$$

where  $\gamma_k$  is an eigenvalue of  $G$ , with  $k = 0, 1, 2, \dots, N-1$ . With regard to the synchronized state, the Jacobian functions  $DF$  and  $DH$  should be the same for each block. Thus for the stability analysis, one can use Eq.(2.12) to calculate the so-called transverse Lyapunov exponents. And Eq.(2.12) is called the master stability function.

## 2.2 Dynamic properties of the basic systems

Before starting to investigate the spatially extended systems with fluctuating time delay, it is important to know the dynamic properties of the basic dynamical system, such as the delayed logistic map and the Hutchinson's equation.

### 2.2.1 Hutchinson's equation

In 1838, the Belgian mathematician Pierre François Verhulst introduced the famous equation [37]

$$\frac{dN}{dt} = rN\left(1 - \frac{N}{K}\right) \quad (2.13)$$

## 2.2. DYNAMIC PROPERTIES OF THE BASIC SYSTEMS

---

to study the population growth problem, an equation which he later called the logistic equation [38]. Afterwards, the logistic function has been applied in a range of fields, including biology, biomathematics, demography, economics, chemistry, mathematical psychology, probability, sociology, political science, statistics, and so on. In 1948, Hutchinson [23] appeared to be the first ecologist to investigate the role of explicit delays in ecological models and introduced the time delay into the logistic equation to form a more realistic logistic model, as shown in Eq.(1.3).

The Hutchinson's equation can have two different states depending on the values of the parameter  $a$  and the delay  $\tau$ . When  $a\tau \leq \frac{\pi}{2}$ , the system converges to the fixed point 1, otherwise one gets a periodic orbit. The threshold  $\frac{\pi}{2}$  can be determined by stability analysis of the fixed points [39]. For the equation

$$0 = au^*(1 - u^*), \quad (2.14)$$

one obtains two fixed points, 0 and 1, for the Hutchinson's equation. Linearizing the Hutchinson's equation allows the governing equation for the perturbation

$$\delta \dot{u}(t) = a(1 - u(t - \tau))\delta u(t) - au(t)\delta u(t - \tau) \quad (2.15)$$

to be determined.

Suppose that  $\delta u(t) = \delta u_0 e^{st}$ , where  $s$  is the stability exponent, which is generally complex. The real part of  $s$  is the Lyapunov exponent  $\lambda$ . By plugging it into Eq.2.15, one obtains

$$s = a(1 - u(t - \tau)) - au(t)e^{-s\tau}. \quad (2.16)$$

For the fixed point 0,  $s = a > 0$ , which means that this fixed point is always unstable. For the fixed point 1, the situation is more complicated, and the characteristic equation is now

$$s = -ae^{-s\tau}, \quad (2.17)$$

where  $s$  is a complex number which can be written as  $\lambda + i\omega$ . The stability of this fixed point can only be changed through the non-hyperbolic fixed point, which means the real part of  $s$  is equal to 0. When substituting  $s = i\omega$  in Eq.(2.17), one gets

$$i\omega = -ae^{-i\omega\tau}. \quad (2.18)$$



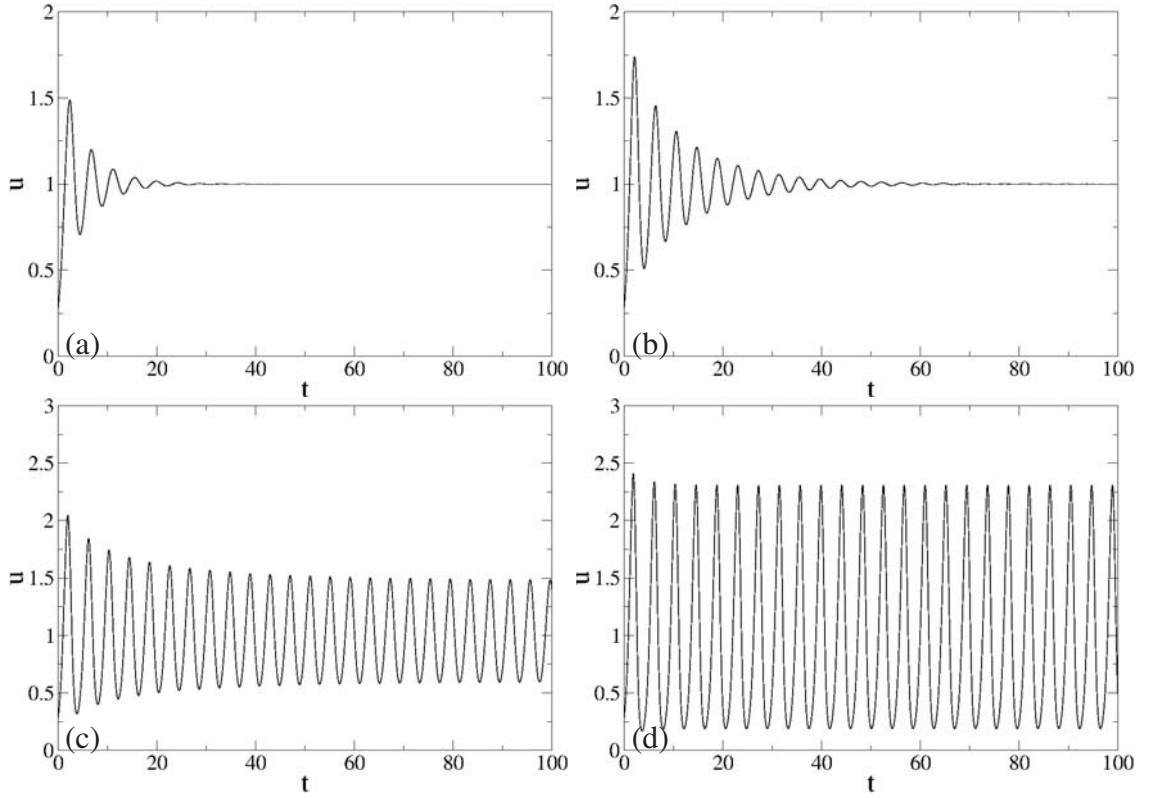


Figure 2.5: Temporal evolution of state for the Hutchinson's equation under different parameter values of  $a$ , with a time delay of  $\tau = 1$ , (a)  $a = 1.2$ , (b)  $a = 1.4$ , (c)  $a = 1.6$ , (d)  $a = 1.8$ .

This equation can be rewritten as

$$0 = a \cos(\omega \tau), \quad \text{and} \quad (2.19)$$

$$\omega = a \sin(\omega \tau). \quad (2.20)$$

The solution of this pair of equations is simply  $\omega = a$ , and  $\omega \tau = 2k\pi + \frac{\pi}{2}$ . This indicates the threshold of this Hutchinson's equation at  $a\tau = \frac{\pi}{2}$ .

In Fig.2.5, one can see the time evolution of the state for the Hutchinson's equation. Panels (a) and (b) correspond to the stationary state. The system converges to the fixed point 1 after sufficient time. Panels (c) and (d) correspond to the periodic state. Here the periodic oscillation in the temporal evolution can be seen. The amplitude of the oscillation is in accordance with the control parameter  $a \cdot \tau$ . In addition, starting from the same initial conditions, the larger  $a \cdot \tau$  is, the more time is necessary for the system to achieve the fixed point.

### 2.2.2 Delayed logistic map

Since the logistic map was introduced by the biologist Robert May in 1976 [40], it has been used as "an archetypal example of how complex, chaotic behavior can arise from very simple nonlinear dynamical equations" [41]. In 1968, Maynard Smith introduced a discrete analogy of Hutchinson's equation [42], obtaining a difference equation

$$u_{n+1} = au_n(1 - u_{n-1}), \quad (2.21)$$

which is the delayed logistic map Eq.(1.7) with a time delay of  $T = 1$ . Like the logistic map, the dynamic of the delayed logistic map is also complex. Fig.2.6 shows the bifurcation diagram and the Maximal Lyapunov exponent  $\lambda$  for Eq.(2.21) as functions of the control parameter  $a$ .

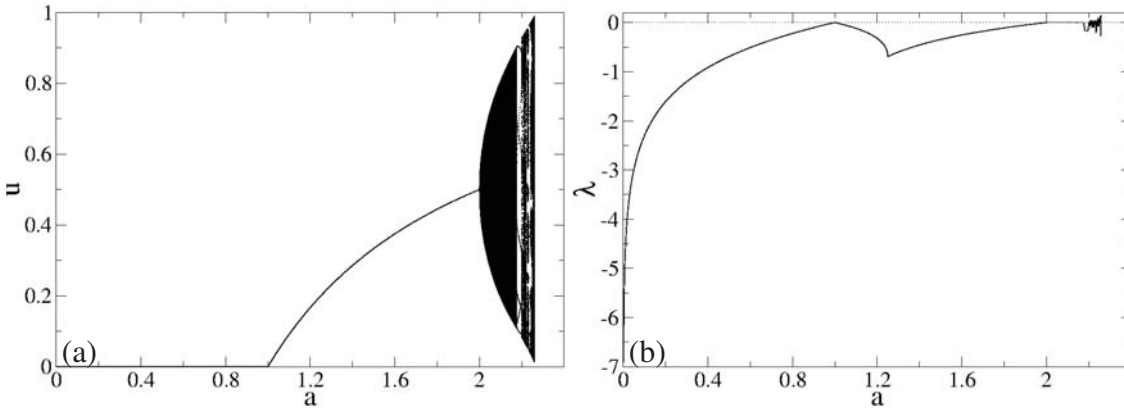


Figure 2.6: Bifurcation diagram and Maximal Lyapunov exponent for Eq.(2.21) as functions of  $a$

The delayed logistic map has two fixed points. One is  $u_1^* = 0$ . It is asymptotically stable for  $0 < a < 1$  and unstable for  $a > 1$ . The other is  $u_2^* = 1 - \frac{1}{a}$ . When  $a > 1$ , the second fixed point is positive and thus significant. This fixed point is asymptotically stable for  $1 < a < 2$ . But there are two different kinds of relaxation dynamics towards the second fixed point in the map's stable region. For  $1 < a < 1.25$ , the solutions starting near this fixed point approach it monotonically, while for  $1.25 < a < 2$ , the solutions starting near this fixed point exhibit damped oscillations as approaching the fixed point. In Fig.2.7, the evolution of states is shown, clearly demonstrating the difference between two kinds of transient dynamics.

The evolution of the stability and the dynamics of the fixed points can also be inferred from the Maximal Lyapunov exponent  $\lambda$ . In Fig.2.6(b),  $\lambda$  is negative and monotonically increases

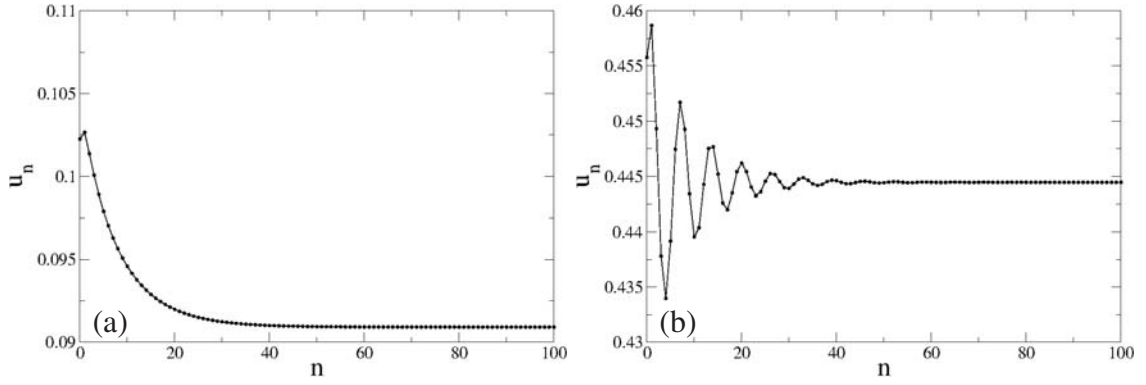


Figure 2.7: (a)  $a = 1.1$ , monotone approach to a fixed point, (b)  $a = 1.8$ , damped oscillations.

for  $0 < a < 1$  and reaches 0 at  $a = 1$ , which means that the system dynamics change here and  $a = 1$  correspond to the stability threshold for changing the fixed points. Beyond this point,  $\lambda$  turns negative again and monotonically decreases until  $a = 1.25$ . This value  $a = 1.25$  is the threshold where the imaginary part of the stability exponent is no longer 0. This result can be confirmed by analytical calculation. The linear equation of Eq.(2.21) for the perturbation reads as

$$\delta u_{n+1} = a(1 - u_{n-1})\delta u_n - au_n\delta u_{n-1}, \quad (2.22)$$

assuming a perturbation  $\delta u_n = \delta u_0 e^{sn}$ , where  $s$  is the stability exponent. In the interval  $a \in [1.25; 2]$ , the stability of the equilibrium point  $u^* = 1 - \frac{1}{a}$  is studied. Thus, one can obtain

$$e^s = 1 - (a - 1)e^{-s}. \quad (2.23)$$

As  $e^s \neq 0$ , the Eq.2.23 can be rewritten as

$$(e^s)^2 - e^s + (a - 1) = 0 \quad (2.24)$$

with the solution  $e^s = \frac{1 \pm \sqrt{1 - 4(a - 1)}}{2}$ .  $e^s$  is real only when  $1 - 4(a - 1) \geq 0$ . And this denotes the threshold  $a = 1.25$ . When  $a \leq 1.25$ ,  $e^s$  is real. Otherwise  $e^s$  is a complex number.

For  $a > 2$ , the system dynamics are complex. Fig.2.8 shows an enlargement of Fig.2.6 in this region. After the Poincare-Andoronov-Hopf bifurcation at  $a = 2$ , one can first observe periodic or quasiperiodic sustained oscillations, which are also called a limit cycle and have a Maximal Lyapunov exponent  $\lambda = 0$ . Then as the parameter  $a$  increases beyond 2, the topology of the invariant curve and the dynamics on it undergo a sudden change and a periodic attractor appears which is stable and has a negative Maximal Lyapunov exponent. As the parameter  $a$  is increased further, the invariant closed curve loses its smoothness and

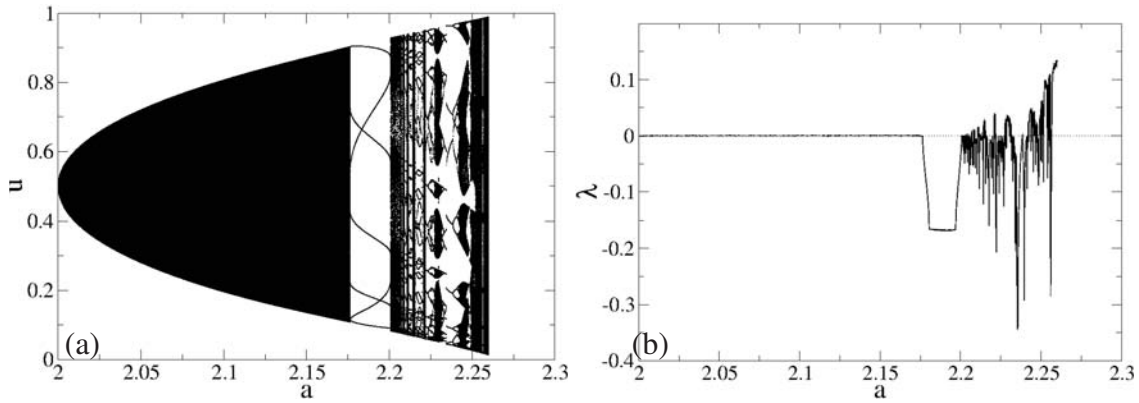


Figure 2.8: Enlarged bifurcation diagram of the one in Fig.2.6(a) and the related Maximal Lyapunov exponent for Eq.(2.21) as a function of  $a$ .

breaks down, giving rise to a strange attractor, for which the Maximal Lyapunov exponent is positive. As Aronson et al. stated in their paper [43]: "In one parameter families the transition from simple to complicated behavior is itself quite complicated." The dynamics of the delayed logistic map are remarkably complicated when the parameter  $a$  is further away from the bifurcation. One can observe different dynamics in a small parameter region (see Fig.2.9).

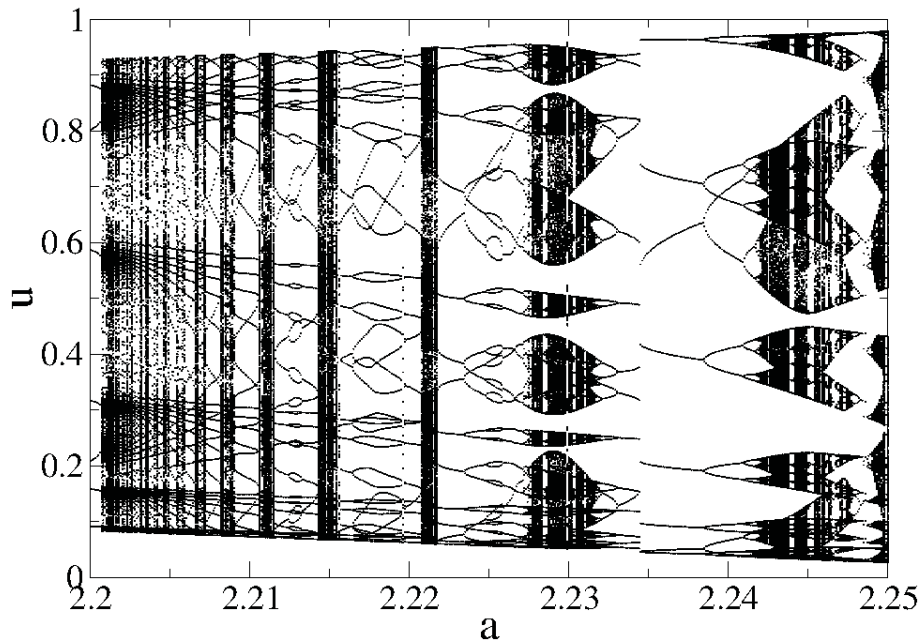


Figure 2.9: Enlarged bifurcation diagram from Fig.2.8(a) for large  $a$

Furthermore, in Fig.2.10, the bifurcation diagram and the related Lyapunov exponents of the delayed logistic map Eq.(1.7) with larger delay are shown. The delay  $T$  is chosen to be 2 or 3. One can see that when delay  $T$  increases, the second fixed point  $u_2^* = 1 - \frac{1}{a}$  loses its stability and the bifurcation point is shifted to a smaller value of the nonlinear parameter  $a$ . And the parameter value where the trajectories describing the system dynamics becomes divergent also becomes smaller. Thus the range of allowed nonlinear parameter  $a$  values is compressed. Complex dynamic behaviors can also be seen beyond the bifurcation.

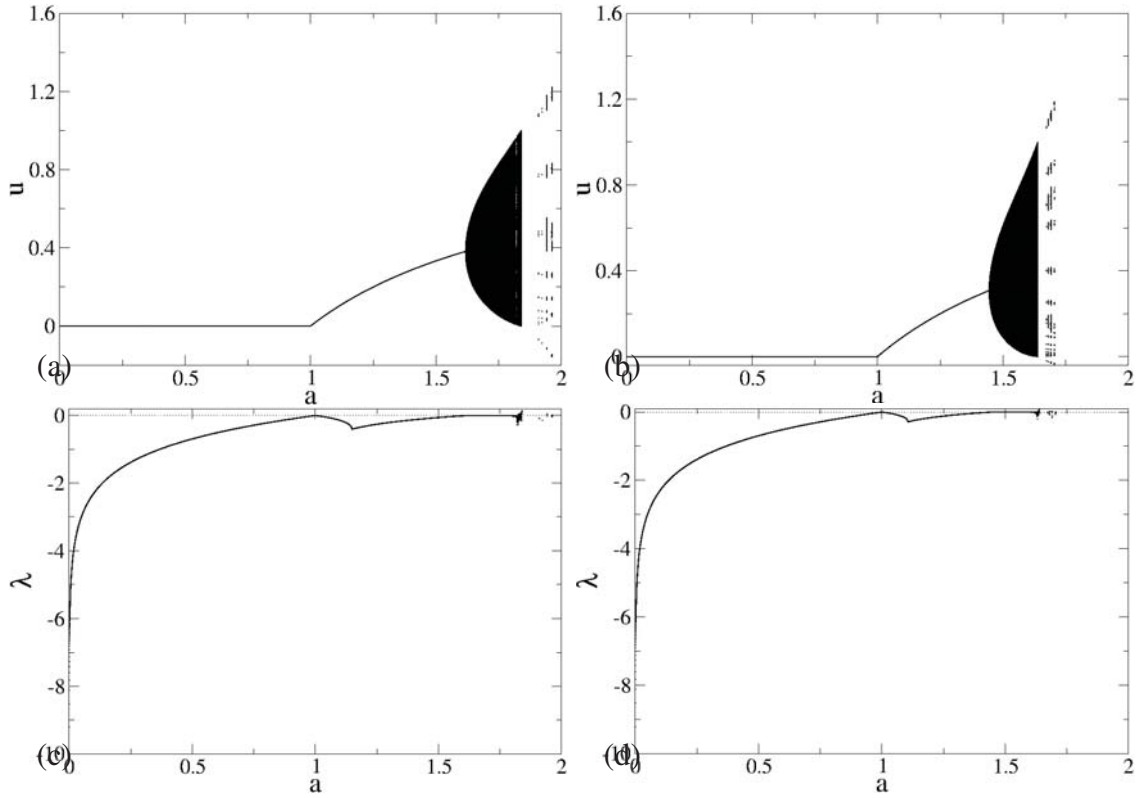


Figure 2.10: Bifurcation diagram for Eq.(1.7) with (a)  $T = 2$ , (b)  $T = 3$  and the related Lyapunov exponents as functions of  $a$  (c)  $T = 2$  (d)  $T = 3$

## 2.3 Dynamics of spatially extended systems

After the spatial extension is introduced in the model, some interesting phenomena appear. The study of spatial structures (also called patterns) which are generated by such systems is one focus of current research. Special structures, such as Turing patterns and traveling waves, are of great interest.

### 2.3.1 Turing instability

Turing instability, which is also known as diffusion-driven instability, was first studied by Alan Turing [44]. In general, the diffusion process should smooth the concentration inequality and lead the system to a uniform stable state. For instance, a drop of ink dissolves in water. But Turing instability shows another possible effect of diffusion. In his paper, A. Turing came up with the idea of a so-called *morphogen* and tried to explain how the pattern on an animal, for instance, stripes on a zebra, is generated through a reaction-diffusion process. But at that time, his paper did not draw attention. There were three causes: First, *morphogen* was not yet a term found in biology. Second, there were some negative concentration values in Turing's model, which cannot be accepted by chemists. And last, at that time, the Turing pattern was just considered to be an isolated phenomenon with no relation to patterns in other systems. After Ilya Prigogine suggested the dissipative structure theory [45], scientists realized that the pattern formation in different systems shared much in common and found Turing's speculations to be realistic. But this was already long after the death of Turing. Today the study of Turing patterns is a research front in the study of pattern formation in dissipative systems. In short, Turing instability shows that the interplay of reaction and diffusion can cause the stable equilibrium of the isolated local system to become unstable for the spatially extended system, leading to the spontaneous formation of spatially periodic stationary structures.

In order to understand Turing instability, one can consider a two-component reaction-diffusion system:

$$\begin{aligned}\frac{\partial U}{\partial t} &= f(U, V) + D_U \nabla^2 U \\ \frac{\partial V}{\partial t} &= g(U, V) + D_V \nabla^2 V,\end{aligned}\tag{2.25}$$

where  $U$ , and  $V$  are the state variables, and  $D_U$ , and  $D_V$  are the diffusion coefficients. This system consists of an *activator*  $U$ , which can facilitate its own reproduction, and an *inhibitor*  $V$ , which slows down the production of the activator. The mechanism of Turing instability can be explained mathematically by a linear stability analysis. For simplicity, we consider here only the one-dimensional case. Suppose that the system has stationary solutions  $(U_0, V_0)$ , which satisfies

$$\begin{aligned}f(U_0, V_0) &= 0, \quad \text{and} \\ g(U_0, V_0) &= 0.\end{aligned}$$

The pair of linearized equations governing the perturbations to the stationary point of Eq.(2.25) are

$$\begin{aligned}\frac{\partial u}{\partial t} &= a_{11}u + a_{12}v + D_u \nabla^2 u, \quad \text{and} \\ \frac{\partial v}{\partial t} &= a_{21}u + a_{22}v + D_v \nabla^2 v,\end{aligned}\tag{2.26}$$

where  $u$ , and  $v$  are the perturbations and

$$\begin{aligned}a_{11} &= \frac{\partial f}{\partial U}|_{U_0, V_0}, \quad a_{12} = \frac{\partial f}{\partial V}|_{U_0, V_0}, \\ a_{21} &= \frac{\partial g}{\partial U}|_{U_0, V_0}, \quad a_{22} = \frac{\partial g}{\partial V}|_{U_0, V_0}.\end{aligned}$$

For the spatially extended system considered, the perturbation can be accounted for by the form

$$\begin{pmatrix} u \\ v \end{pmatrix} = \sum_k \begin{pmatrix} c_k^1 \\ c_k^2 \end{pmatrix} e^{s_k t + i k x},\tag{2.27}$$

where  $s_k$  is the stability exponent, and  $k$  is the wavenumber. This form of the perturbation can be substituted into the linearized equation (2.26), resulting in the characteristic equation

$$s_k \begin{pmatrix} c_k^1 \\ c_k^2 \end{pmatrix} = \begin{pmatrix} a_{11} - k^2 D_U & a_{12} \\ a_{21} & a_{22} - k^2 D_V \end{pmatrix} \begin{pmatrix} c_k^1 \\ c_k^2 \end{pmatrix}.\tag{2.28}$$

By solving the characteristic polynomial, one obtains

$$s_k^2 - Tr_k s_k + \Delta_k = 0\tag{2.29}$$

with

$$Tr_k = a_{11} + a_{22} - k^2(D_U + D_V) = Tr_0 - k^2(D_U + D_V),\tag{2.30}$$

and

$$\begin{aligned}\Delta_k &= a_{11}a_{22} - a_{21}a_{12} - k^2(a_{11}D_V + a_{22}D_U) + k^4 D_U D_V \\ &= \Delta_0 - k^2(a_{11}D_V + a_{22}D_U) + k^4 D_U D_V.\end{aligned}\tag{2.31}$$

Finally, one can derive the solution

$$s_k = \frac{Tr_k \pm \sqrt{Tr_k^2 - 4\Delta_k}}{2}.\tag{2.32}$$

In contrast to the stability analysis solutions of ordinary differential equations, the solutions of a partial differential equation can be stable only if the real parts of all eigenvalues  $s_k$

### 2.3. DYNAMICS OF SPATIALLY EXTENDED SYSTEMS

are negative. Otherwise, perturbations with certain wavenumbers would be induced and the system would become unstable. The dependence of the real part of  $s$  on the wavenumber  $k$  can be roughly classified into two types (see Fig.2.11). For the first type, the maximum of  $Re(s_k)$  is located at  $k = 0$  (Fig.2.11(a)), while for the other type, the maximum is found for a nonzero wavenumber  $k > 0$  (Fig.2.11(b)). Assuming  $\mu$  is the set of control parameters, there is a critical value  $\mu_c$ , under which  $\max(s_k) = 0$ .

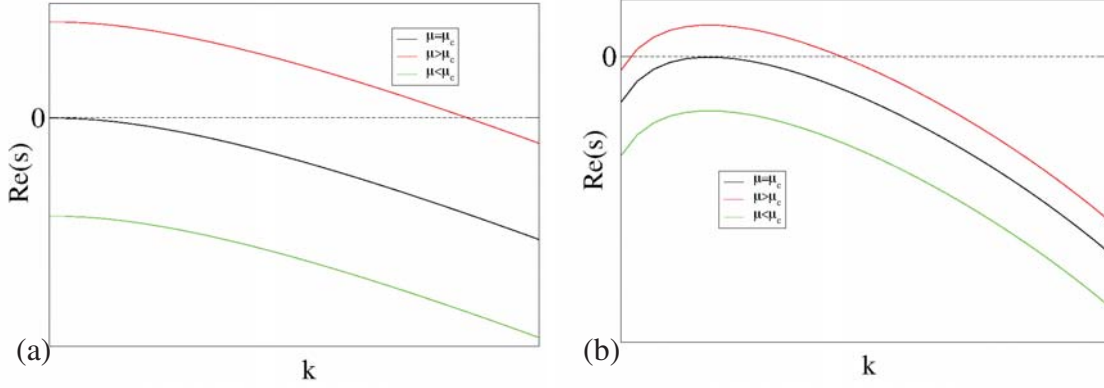


Figure 2.11: Schematic diagram of the two different types of relationship between  $Re(s)$  and  $k$ .

From the definition of Turing instability, one knows that the stationary state should be stable for isolated local dynamics, which means  $s_0 < 0$  for  $k = 0$ , therefore

$$Tr_0 = a_{11} + a_{22} < 0, \quad (2.33)$$

and

$$\Delta_0 = a_{11}a_{22} - a_{21}a_{12} > 0. \quad (2.34)$$

Because the diffusion coefficients  $D_U$  and  $D_V$  are positive in Eq.(2.30),  $Tr_k < Tr_0 < 0$ . Hence, with respect to Eq.(2.32) one eigenvalue is always negative. But the system is known to be unstable for some value of  $k$ . Therefore,  $\Delta_k = s_{k1} \cdot s_{k2}$  should be negative for certain  $k$  values, namely,

$$\Delta_0 - k^2(a_{11}D_V + a_{22}D_U) + k^4D_UD_V < 0. \quad (2.35)$$

To satisfy this inequality, the coefficient at  $k^2$  must be positive

$$a_{11}D_V + a_{22}D_U > 0. \quad (2.36)$$



By solving Eq.(2.31) for the local extreme of  $k^2$  (setting the first derivative of the equation for  $k^2$  equal to 0), the critical value  $k_c$  can be obtained:

$$k_c^2 = \frac{a_{11}D_V + a_{22}D_U}{2D_UD_V}. \quad (2.37)$$

Plugging the critical value  $k_c$  into Eq.(2.31) yields a new condition for Turing instability:

$$\Delta_{kc} = \Delta_0 - \frac{(a_{11}D_V + a_{22}D_U)^2}{4D_UD_V} < 0, \quad (2.38)$$

which can be rearranged as

$$\frac{D_V}{D_U}a_{11} + a_{22} > 2\sqrt{\Delta_0 \frac{D_V}{D_U}}. \quad (2.39)$$

So the sufficient conditions for Turing instability in a two-component reaction-diffusion system are defined by Eqs.(2.33), (2.34), (2.36), and (2.39). With simple calculations, one finds that the conditions can only be satisfied when  $D_V > D_U$ , which means that the diffusion coefficient of the inhibitor should be larger than the diffusion coefficient of activator. In other words, the propagation velocity of the inhibitor is faster than that of the activator. Hence, the Turing instability is also called diffusion-induced instability.

When a system satisfies all four conditions, the spatially homogeneous state corresponding to the state  $(U_0, V_0)$  becomes unstable to perturbations with wavenumber  $k$  within a finite range

$$k_1 < k < k_2.$$

The boundary wavenumbers  $k_{1,2}$  can be calculated from the equation  $s_k = 0$ ,

$$k_{1,2}^2 = \frac{a_{11}D_V + a_{22}D_U}{2D_UD_V} \pm \frac{\sqrt{(a_{11}D_V + a_{22}D_U)^2 - 4D_UD_V\Delta_0}}{2D_UD_V} \quad (2.40)$$

When studying a spatially extended system, one usually assumes the whole system to be over a finite domain with no-flux boundary conditions. In this case, the spectrum of allowed wavelengths becomes discrete:

$$k_n = n\pi/L, \quad n = 1, 2, \dots$$

$$\omega_n = 2\pi/k_n = 2L/n,$$

where  $L$  is the discrete domain size. In the positive region several  $k_n$  exist, and the structure will be determined by the wavenumber with the largest real part of the stability exponent  $s$ .

### 2.3.2 Traveling wave solutions

For a spatially extended system, in addition to the spatially periodic stationary solution already discussed, more complex spatio-temporal dynamics can be observed. One such important spatio-temporal state is the traveling wave solution with the general form

$$U(x, t) = \phi(kx - \omega t), \quad (2.41)$$

where  $\phi$  is a function,  $k$  is the wavenumber, and  $\omega$  is the frequency. The evolution of the system state depends on the whole term  $kx - \omega t$ , which represents a wave propagation with the velocity

$$v_p = \frac{\omega}{k}. \quad (2.42)$$

As already discussed, the dynamic structure factor is used to characterize the structures. An example is shown in Fig.2.12. Two simple states are considered. One is the traveling wave solution

$$U(x, t) = \sin(k_0 x - \omega_0 t), \quad (2.43)$$

and the other is a spatially and temporally decoupled wave state

$$V(x, t) = \cos(k_0 x) \sin(\omega_0 t), \quad (2.44)$$

which can also be understood as standing wave.

In Fig.2.12, the parameters are chosen to be  $k_0 = 2$  and  $\omega_0 = 3$ . The space domain has a size of  $4\pi$  with periodic boundary conditions.

According to the definition of dynamic structure factors, the related autocorrelation functions should be calculated first. Generally, the autocorrelation function for a process  $f(x, t)$  is defined as

$$R_{ff} = \lim_{a \rightarrow \infty} \lim_{b \rightarrow \infty} \int_{-a}^a dt \int_{-b}^b dx f(x, t) f^*(x - s, t - \tau). \quad (2.45)$$

For the above, there are two functions:

$$R_{UU}(s, \tau) = \lim_{a \rightarrow \infty} [2ab \cos(k_0 s - \omega_0 \tau) - \frac{\sin(2bk_0) \sin(2a\omega_0)}{2k_0\omega_0} \cos(k_0 s - \omega_0 \tau)], \quad (2.46)$$

and

$$R_{VV}(s, \tau) = \lim_{a \rightarrow \infty} (a - \frac{1}{2\omega_0} \sin(2\omega_0 a)) (\frac{1}{2k_0} \sin(2k_0 b) - b) \cos(k_0 s) \cos(\omega_0 \tau). \quad (2.47)$$

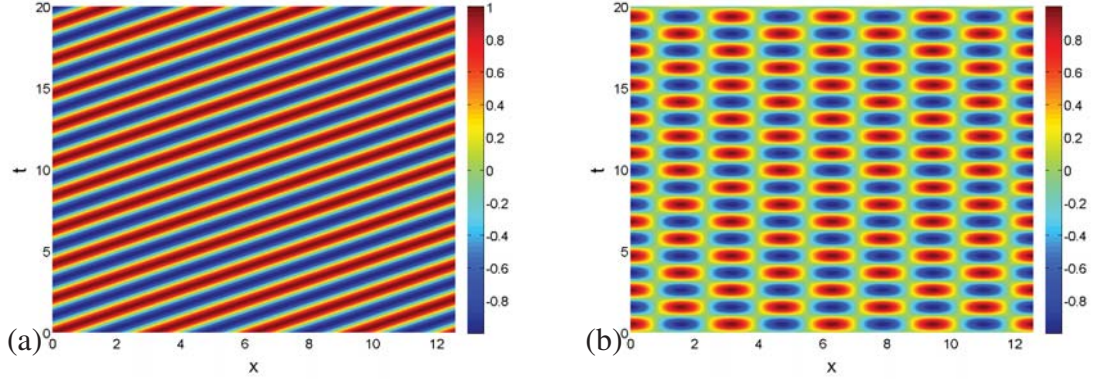


Figure 2.12: Examples of (a) a traveling wave state and (b) a spatially and temporally decoupled wave state.  $k_0 = 2$  and  $\omega_0 = 3$ . The space domain has a size of  $4\pi$  with periodic boundary conditions.

For  $s = 0$  and  $\tau = 0$ , they read

$$R_{UU}(0,0) = \lim_{a \rightarrow \infty} [2ab - \frac{\sin(2bk_0) \sin(2a\omega_0)}{2k_0\omega_0}] \quad (2.48)$$

and

$$R_{VV}(0,0) = \lim_{a \rightarrow \infty} (a - \frac{1}{2\omega_0} \sin(2\omega_0 a)) (\frac{1}{2k_0} \sin(2k_0 b) - b). \quad (2.49)$$

The normalization of  $R$  reads

$$r_{UU}(s, \tau) = \frac{R_{UU}(s, \tau)}{R_{UU}(0,0)} \approx \cos(k_0 s - \omega_0 \tau) \quad (2.50)$$

and

$$r_{VV}(s, \tau) = \frac{R_{VV}(s, \tau)}{R_{VV}(0,0)} \approx \cos(k_0 s) \cos(\omega_0 \tau). \quad (2.51)$$

Thus, for the traveling wave state, a 2D Fourier transformation yields

$$\tilde{r}_{UU} = \pi \delta(k + k_0) \delta(\omega - \omega_0) + \pi \delta(k - k_0) \delta(\omega + \omega_0) \quad (2.52)$$

and for the spatially and temporally separated state

$$\begin{aligned} \tilde{r}_{VV} = & \frac{1}{2} \pi \delta(k - k_0) \delta(\omega - \omega_0) + \frac{1}{2} \pi \delta(k + k_0) \delta(\omega - \omega_0) \\ & + \frac{1}{2} \pi \delta(k - k_0) \delta(\omega + \omega_0) + \frac{1}{2} \pi \delta(k + k_0) \delta(\omega + \omega_0). \end{aligned} \quad (2.53)$$

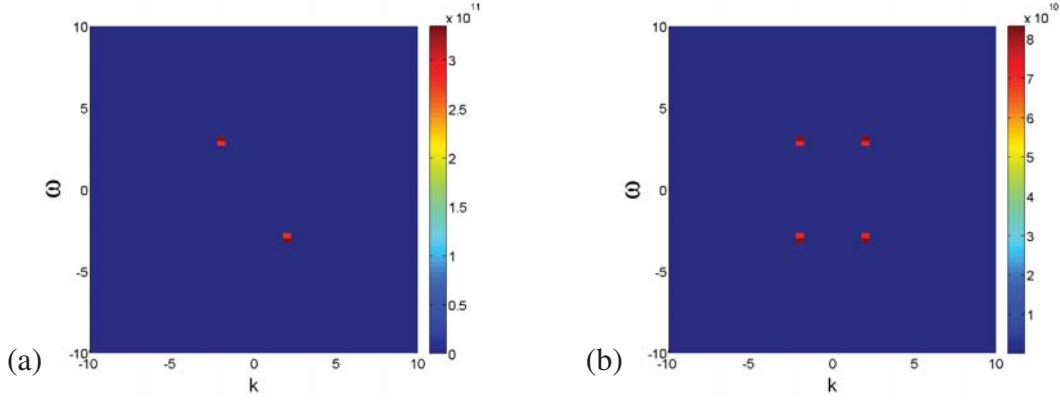


Figure 2.13: Dynamic structure factors for the two examples in Fig2.12, (a) a traveling wave state, and (b) a spatially and temporally decoupled wave state.

Now one can find the difference between two states. While the spatially and temporally separated state has four symmetric peaks in Fourier space, for the traveling wave, there are only two peaks, which are symmetrical with respect to the central origin. The velocity can be obtained as the negative slope of the line between these two peaks in  $k$ - $\omega$  space. In Fig.2.13, one can see the dynamic structure factor for the two examples. The signal size used is  $4\pi$  in space and 20 in time. Since the spatial periodic boundary condition is used, the Hamming window is used in the temporal spectrum analysis to reduce the spectral leakage. One can see that the peaks are located at  $k = \pm 3$  and  $\omega = \pm 2$ .

To test the applicability of the Wiener-Khinchin theorem in this case, one can also directly calculate the 2D Fourier transformation of Eqs.(2.43) and (2.44), which gives

$$\tilde{U} = -i\pi\delta(k+k_0)\delta(\omega-\omega_0) + i\pi\delta(k-k_0)\delta(\omega+\omega_0), \quad (2.54)$$

and

$$\begin{aligned} \tilde{V} = & \frac{1}{2}i\pi\delta(k-k_0)\delta(\omega-\omega_0) + \frac{1}{2}i\pi\delta(k+k_0)\delta(\omega-\omega_0) \\ & - \frac{1}{2}i\pi\delta(k-k_0)\delta(\omega+\omega_0) - \frac{1}{2}i\pi\delta(k+k_0)\delta(\omega+\omega_0). \end{aligned} \quad (2.55)$$

It is clear that the peaks are at the same position as in Eqs.(2.52) and (2.53).

## 3 Coupled Map Lattices

This chapter studies discrete spatially extended systems with delays, in particular, diffusively coupled map lattices. The study of the spatially extended system with delay can be approached from two directions: one is from the isolated delay system to investigate the influence of spatial coupling, and the other is from the spatially extended system to study the influence of delay. The following results will be presented along these two directions.

### 3.1 Coupled map lattices without delay and with constant delay

First the coupled map lattices without a delay as well as those with a constant delay are studied. They are one starting point of the considered discrete model.

#### 3.1.1 Coupled map lattice without delay

As a starting point, consider a lattice diffusively coupled logistic map

$$\begin{aligned} u_{n+1}^i &= (1 - \varepsilon)F(u_n^i) + \frac{1}{2}\varepsilon[F(u_n^{i-1}) + F(u_n^{i+1})] \\ F(u_n^i) &= 1 - a(u_n^i)^2, \end{aligned} \tag{3.1}$$

which has been investigated in depth by K. Kaneko [26]. Here the map  $F(u_n)$  is a variation of the famous logistic maps. Details of this map can be found in Refs. [46, 47]. With this model, different pattern classes were observed. Here it is used as a reference for understanding the phenomena of our model with time delay.

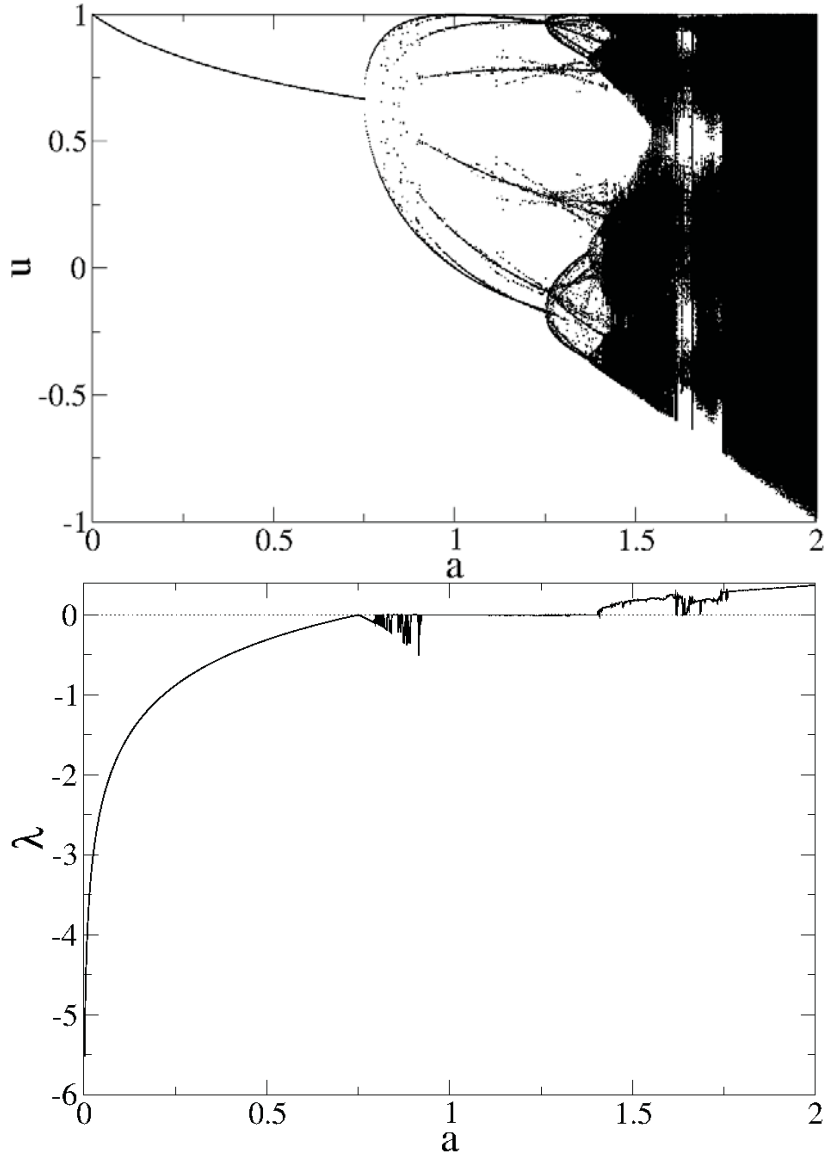


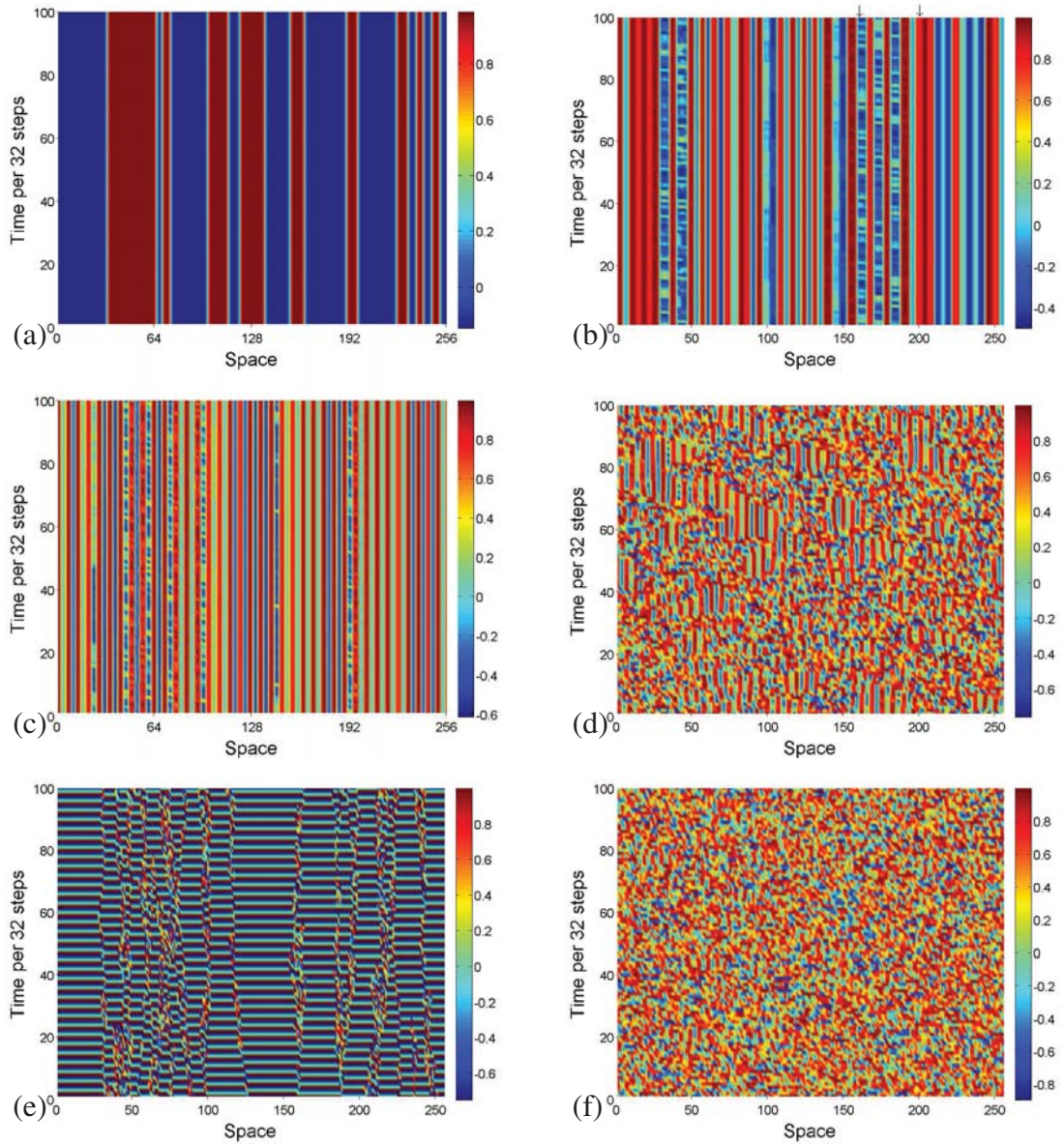
Figure 3.1: Bifurcation diagram and maximal Lyapunov exponent as functions of the nonlinear parameter  $a$  for Eq.(3.1) with  $\varepsilon = 0.4$ . The system size is chosen to be 256. Periodic boundary conditions and random initial conditions are used.

In Fig.3.1, the bifurcation diagram and maximal Lyapunov exponent of Eq.(3.1) as functions of the nonlinear parameter  $a$  are shown. The states and the corresponding maximal Lyapunov exponents can be compared. Fig.3.2 shows examples of various patterns which are generated by this model. The classification of the different states refers mostly to Kaneko's work [26].



### 3.1. COUPLED MAP LATTICES WITHOUT DELAY AND WITH CONSTANT DELAY

The generated patterns depend on the parameters  $a$  and  $\varepsilon$ . For small  $a$ , the system has a spatially homogeneous state. Beyond the bifurcation point  $a = 0.75$ , it exhibits the periodic-doubling of kinks, and patterns with kinks (Fig.3.2(a)) can be observed. As the nonlinear parameter  $a$  is further increased, after a periodic-doubling cascade, the system exhibits chaotic behavior correspondingly, with the domain structure sensitively dependent on initial conditions. Frozen random patterns consisting of both chaotic and regular regions (Fig.3.2(b)) can be observed. In the regular region, the dynamic behavior is not exactly regular, but slightly fluctuates. As examples, two temporal trajectories at different sites for the frozen random pattern (denoted by arrows in Fig.3.2(b)) are shown in Fig.3.3. In Fig.3.3(a) one can see



### 3.1. COUPLED MAP LATTICES WITHOUT DELAY AND WITH CONSTANT DELAY

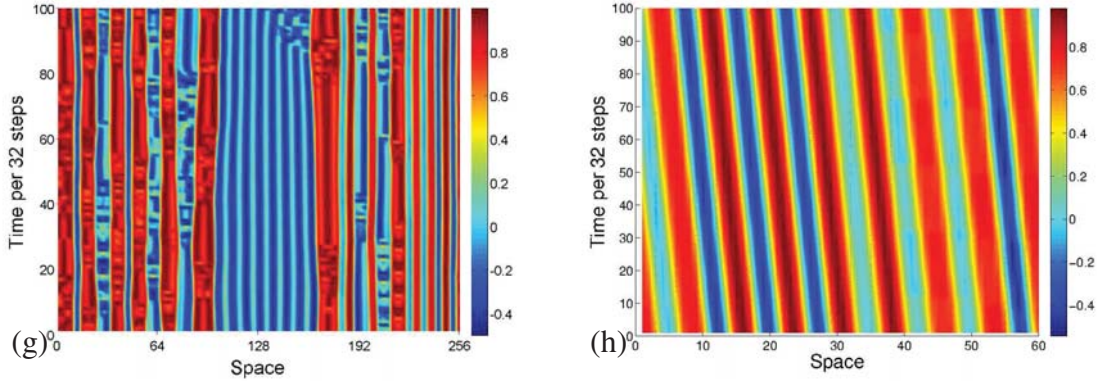


Figure 3.2: Different pattern classes of Eq.(3.1). The patterns are generated from random initial conditions and are depicted after  $2 \cdot 10^5$  iterations. Periodic boundary conditions are considered. Unless mentioned otherwise, the system size is chosen to be 256. (a) Pattern with kinks:  $a = 1.2$ ,  $\varepsilon = 0.4$ , plotted per 32 time steps. (b) Frozen random pattern:  $a = 1.5$ ,  $\varepsilon = 0.4$ , plotted per 32 time steps. (c) Pattern selection:  $a = 1.73$ ,  $\varepsilon = 0.4$ , plotted per 32 time steps. (d) Spatiotemporal intermittency:  $a = 1.77$ ,  $\varepsilon = 0.4$ , plotted per 32 time steps. (e) Spatiotemporal intermittency:  $a = 1.752$ ,  $\varepsilon = 0.001$ , plotted per 32 time steps. (f) Fully developed spatiotemporal chaos:  $a = 1.9$ ,  $\varepsilon = 0.4$ , plotted per 32 time steps. (g) Traveling wave:  $a = 1.5$ ,  $\varepsilon = 0.5$ , plotted per 32 time steps. (h) Traveling wave:  $a = 1.8$ ,  $\varepsilon = 0.5$ , plotted per 32 time steps. The system size is 60.

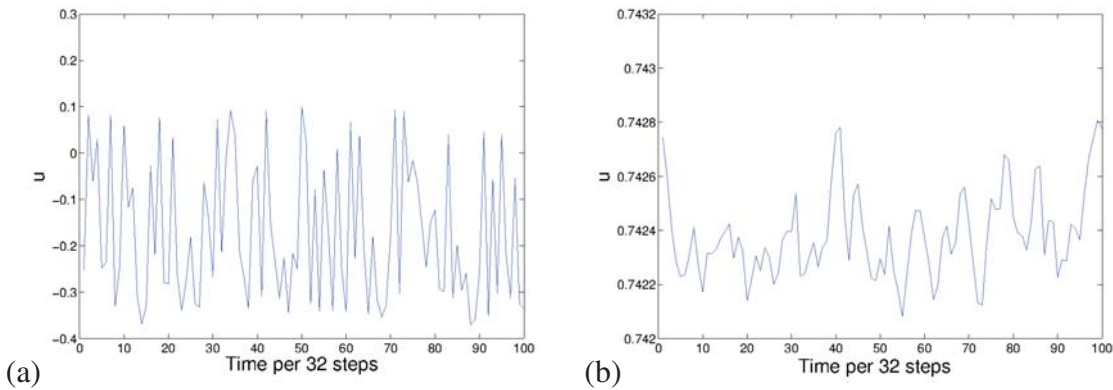


Figure 3.3: Temporal trajectories for the structure in Fig.3.2(b) at sites (a) 160 and (b) 200.

the temporal evolution at the site 160, where chaotic dynamics can be observed in Fig.3.2(b). In Fig.3.3(b) the temporal evolution at the site 200 is shown, which looks regular in Fig.3.2(b). Here one can observe a slight fluctuation around a large mean value. In contrast



### 3.1. COUPLED MAP LATTICES WITHOUT DELAY AND WITH CONSTANT DELAY

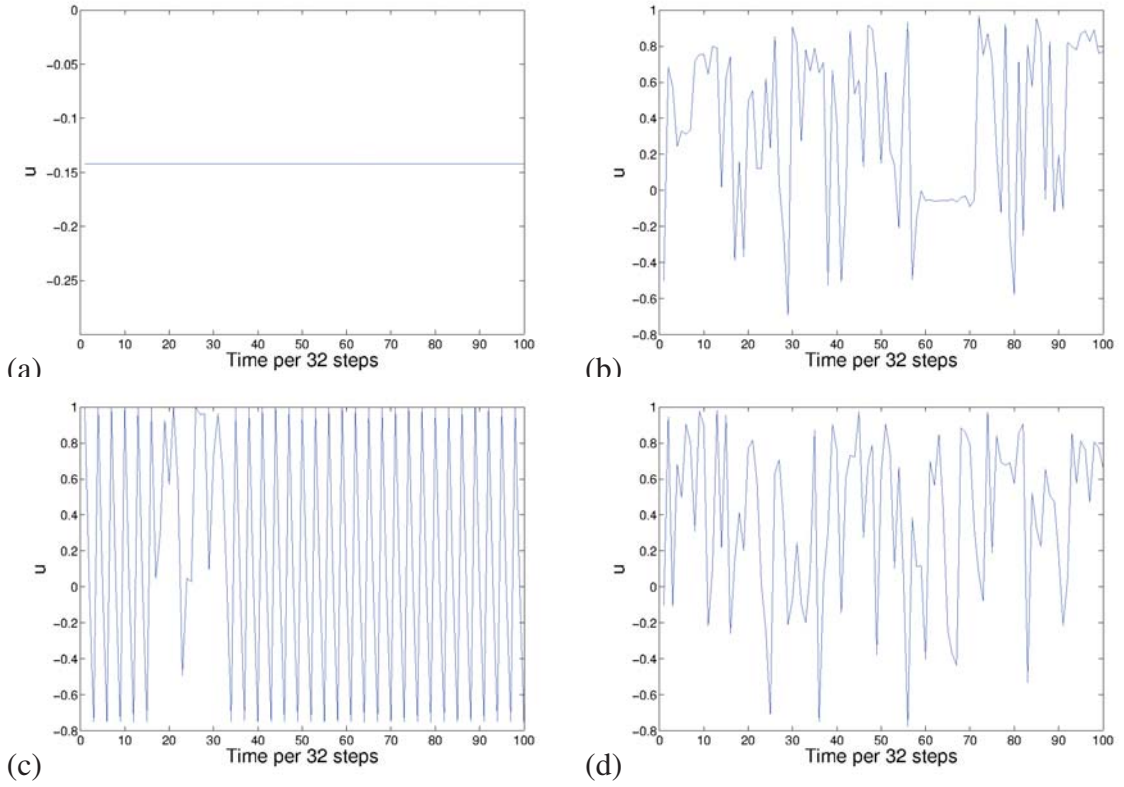


Figure 3.4: Temporal trajectories for the structure in (a) Fig.3.2(a) at site 20, (b) Fig.3.2(d) at site 82, (c) Fig.3.2(e) at site 120, and (d) Fig.3.2(f) at site 100.

to the temporal evolution of the pattern with kinks, the temporal evolution in the regular region is stationary (see Fig.3.4(a)).

When  $a$  is further increased to values beyond the so-called  $2 \rightarrow 1$  band merging point [48], large spatial domains start to become unstable and split into smaller domains. The band structure is no longer determined by the initial conditions. Smaller-sized domains are normally selected. This is called pattern selection (Fig.3.2(c)).

As  $a$  is further increased, before the system enters fully chaotic states (Fig.3.2(f)), spatio-temporal intermittency can be observed. For the model Eq.(3.1) two types of spatiotemporal intermittencies can be observed. In the first type, there is no spontaneous creation of bursts (Fig.3.2(e)). If a site and its neighbors are laminar, this site remains laminar in the next step. The temporal evolution at site 120 is shown in Fig.3.4(c). Some irregularity can be observed for times between 10 and 40. At other times, it behaves regularly. In the second type, bursts can be observed. For instance, in Fig.3.2(d), some bursts can be seen at the site even if all

### 3.1. COUPLED MAP LATTICES WITHOUT DELAY AND WITH CONSTANT DELAY

---

the states of the site and its neighbors are laminar. The temporal evolution at site 82 of this structure is shown in Fig.3.4(b). The dynamics in this figure are irregular, but for the times between 60 and 70, there is only a slight fluctuation around a large mean value.

Regarding the dependence on the parameter  $\varepsilon$ , when  $\varepsilon$  is small, the domain structures are fixed in space. As the coupling  $\varepsilon$  is increased and becomes larger than 0.45, the domain can move with a certain velocity and a traveling wave can be observed. At the parameter value of  $a$  corresponding to the frozen random pattern, the motion of domain boundaries is irregular (Fig.3.2(g)), while a regular traveling wave (Fig.3.2(h)) can be observed in the pattern-selection region.

A slightly different version of the CML reads:

$$u_{n+1}^i = au_n^i(1 - u_n^i) + D(u_n^{i+1} + u_n^{i-1} - 2u_n^i). \quad (3.2)$$

Due to the change in the diffusive coupling term, the dynamic behavior of the model Eq.(3.2) is different than that of the commonly used model Eq.(3.1). One phenomenon is that the bifurcation point location, which depends on the nonlinear parameter  $a$ , is no longer fixed when the coupling strength  $D$  is varied. Notice that for the model in Fig.3.1, even when  $\varepsilon = 2 \cdot D = 0.4$  the bifurcation point is still located at  $a = 0.75$ . In Fig.3.5 and Fig.3.6, the bifurcation diagram and the maximal Lyapunov exponent as functions of the nonlinear parameter  $a$  for the system described by Eq.(3.2) are shown for different  $D$  values. One can see that the  $P1 \rightarrow P2$  bifurcation point shifts itself to the left with increasing coupling strength  $D$ . Moreover, the allowed range of  $a$  also decreases with increasing  $D$ . Due to the coupling, the value of the state variable of the coupled map lattice can be out of the interval  $[0, 1]$ , which may cause divergence to infinity after some iterations.

To show the sensitiveness on the coupling strength, one can depict another bifurcation in which the diffusion coupling  $D$  varies. Fig.3.7 is an example of this bifurcation diagram. As can be seen, for a fixed parameter  $a = 1.6$ , the system does not converge to the fixed point when the coupling strength  $D$  is sufficiently large.

The different classes of patterns, including patterns with kinks, frozen random patterns, pattern selection, spatiotemporal intermittency, and traveling waves, which are observed in the CML described by Eq.(3.1), can also be obtained in the model from Eq.(3.2). Due to the change in coupling, the transitions of the various pattern classes are different and complex in this model. Here we show some examples for the various patterns in Fig.3.9. Fig.3.8

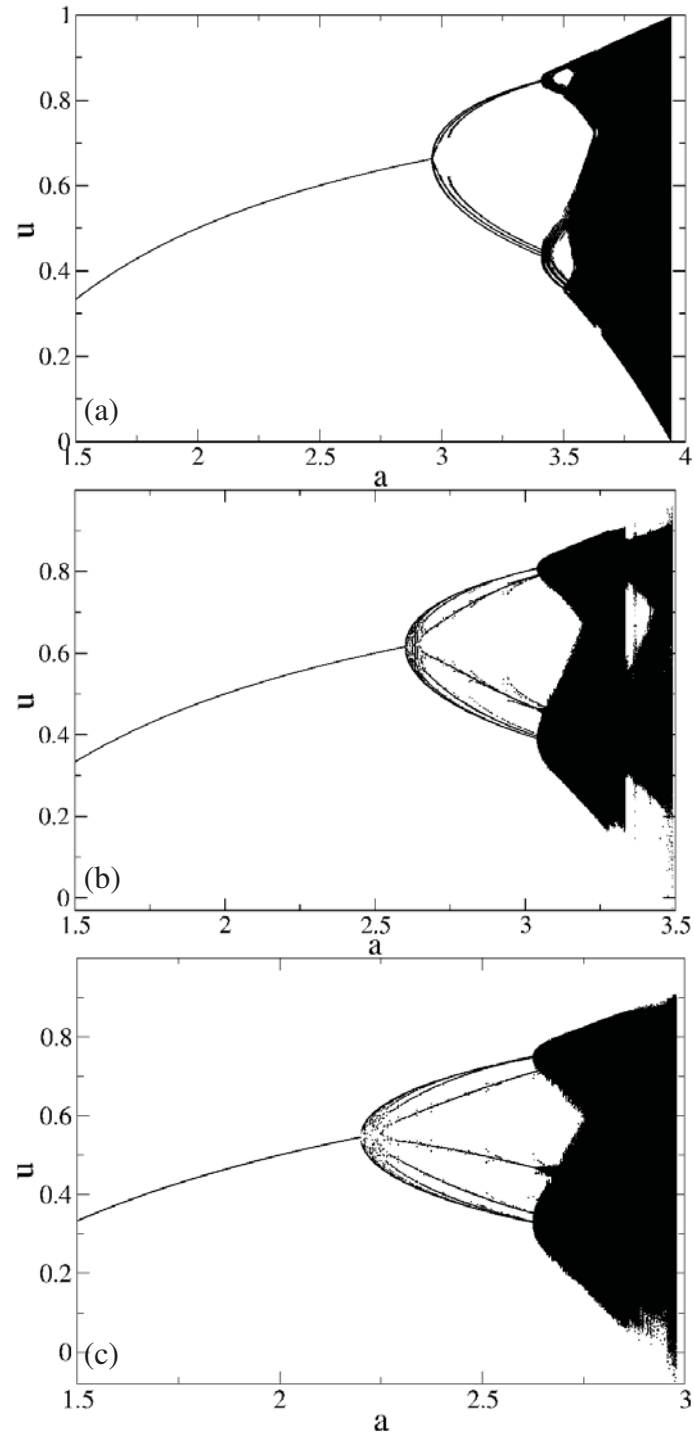


Figure 3.5: Bifurcation diagrams of Eq.(3.2) with different coupling strength  $D$ . The system size is chosen to be 256. Periodic boundary conditions and random initial conditions are used. (a)  $D = 0.01$ , (b)  $D = 0.1$ , and (c)  $D = 0.2$ .

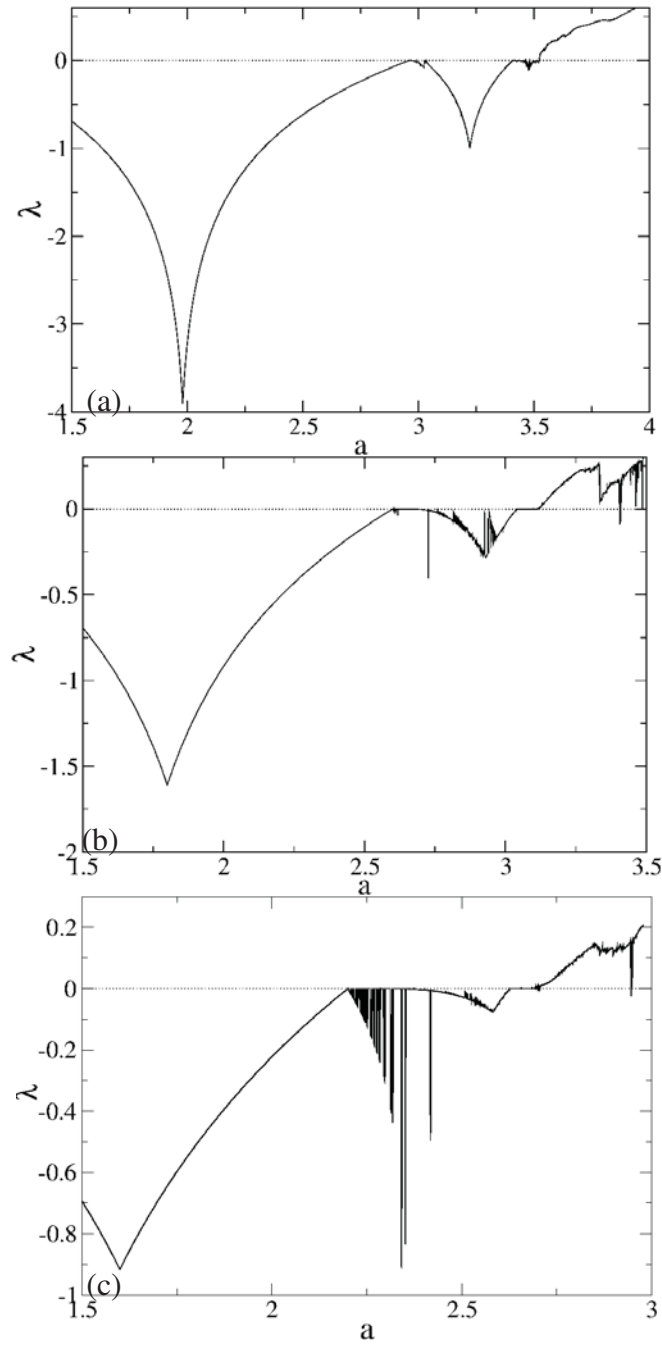


Figure 3.6: Maximal Lyapunov exponent as a function of  $a$  of Eq.(3.2) with different coupling strength  $D$ . The system size is chosen to be 256. Periodic boundary conditions and random initial conditions are used. (a)  $D = 0.01$ , (b)  $D = 0.1$ , and (c)  $D = 0.2$ .

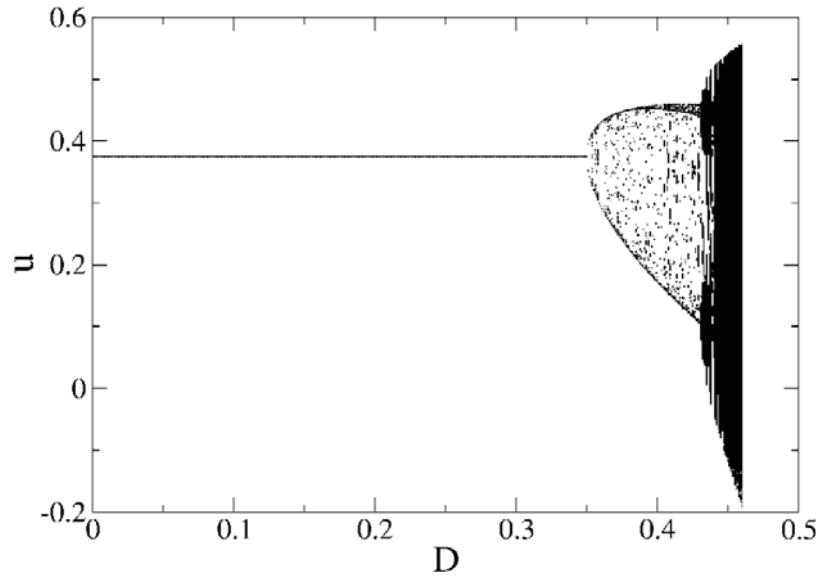


Figure 3.7: Bifurcation diagram with the coupling strength  $D$  of Eq.(3.2) as the independent variable, with  $a = 1.6$ .

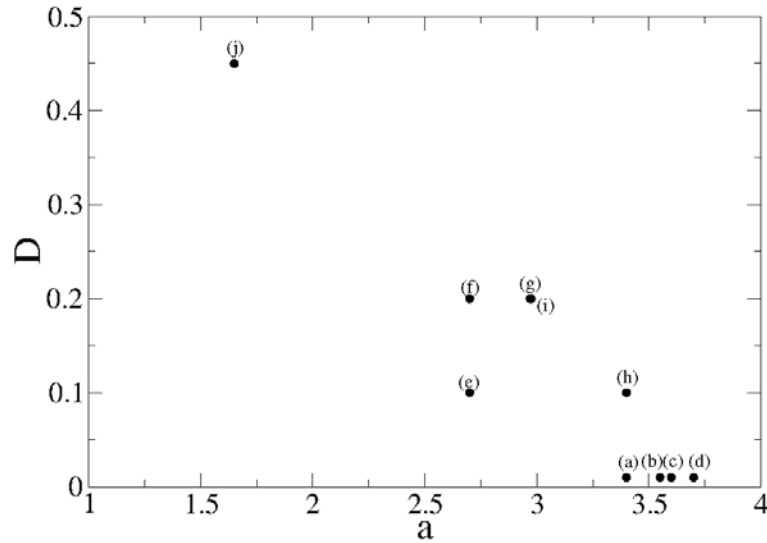


Figure 3.8: Location of the parameters of the examples in Fig.3.9 in  $a$ - $D$ -space.

shows the parameter locations for examples in  $a$ - $D$ -space.

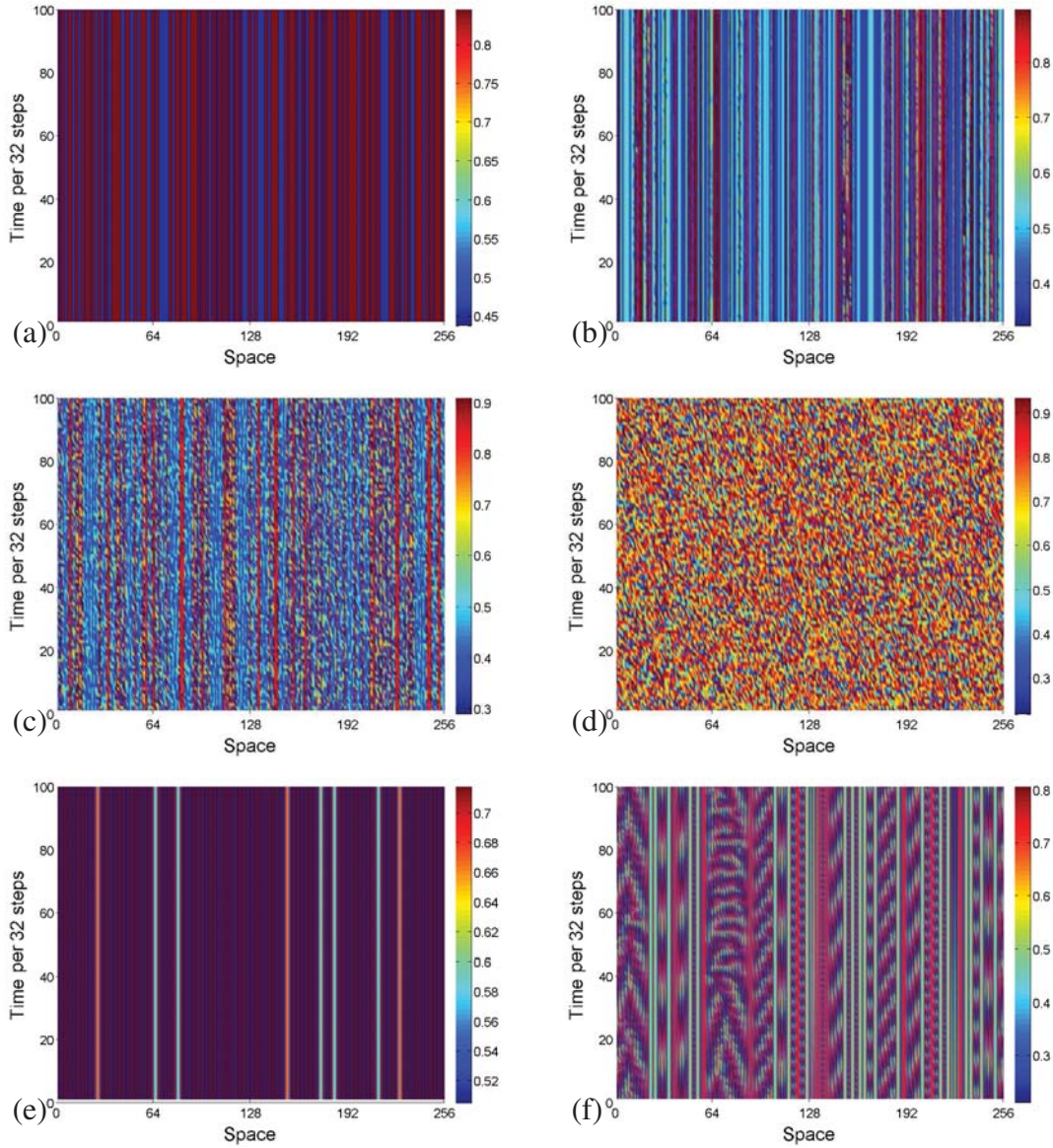
At very small  $a$  values, spatially homogeneous attractors are observed. After the  $P1 \rightarrow P2$  bifurcation point, which depends on the coupling strength  $D$ , patterns with kinks can be obtained (Fig.3.9(a)). But for large  $D$ , the large spatial domain between kinks splits into small regions and the resulting pattern looks like pattern selection (Fig.3.9(e)). As the

### 3.1. COUPLED MAP LATTICES WITHOUT DELAY AND WITH CONSTANT DELAY

nonlinear parameter  $a$  is increased, random frozen pattern and pattern selection states are obtained.

For a small  $D$ , the pattern selection states are directly obtained after the  $P1 \rightarrow P2$  transition (Fig.3.9(b)), while the random frozen patterns can be obtained for large  $D$  (Fig.3.9(f)). When  $a$  is further increased, before fully developed spatiotemporal chaotic states are generated (Fig.3.9(d)), one can obtain the spatiotemporal intermittency (Fig.3.9(c)(g)). In this model, both types of spatiotemporal intermittency can be obtained.

Because of the shrink in the value range, in this model for some large  $D$  values, the pattern





### 3.1. COUPLED MAP LATTICES WITHOUT DELAY AND WITH CONSTANT DELAY

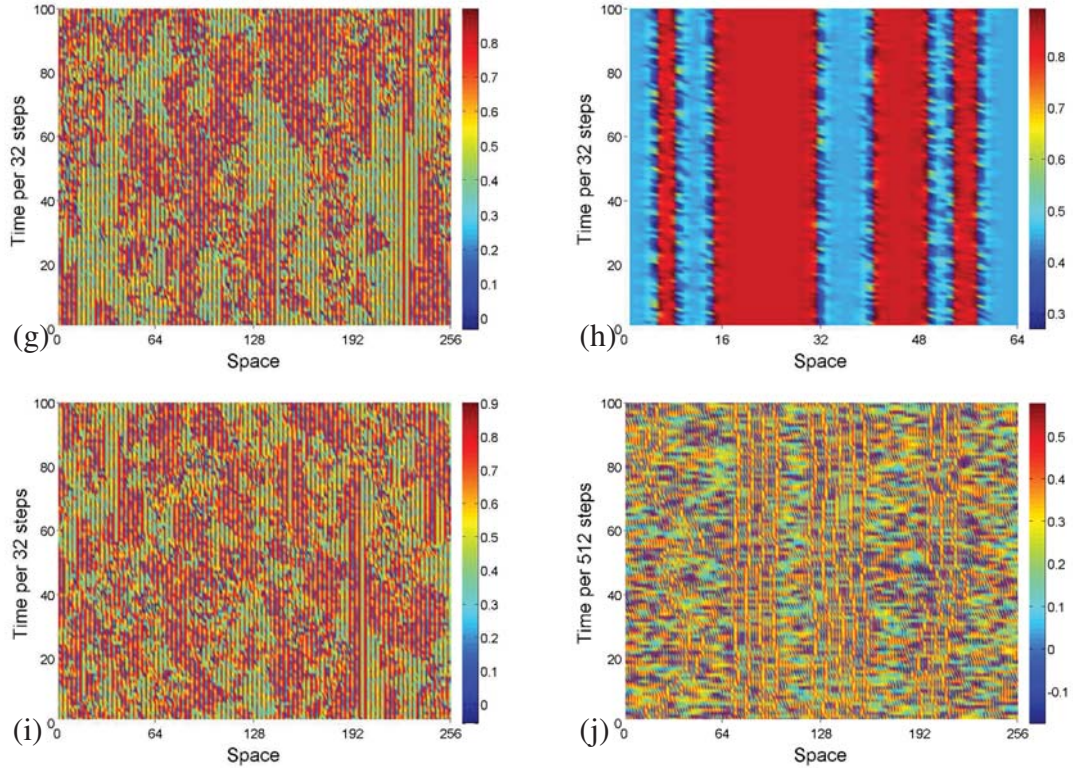


Figure 3.9: Space-time plot of Eq.(3.2). The patterns are generated from random initial conditions and are shown after  $2 \cdot 10^5$  iterations. Periodic boundary conditions are considered. Unless mentioned otherwise, the system size is chosen to be 256. (a)  $a = 3.4$ ,  $D = 0.01$ , plotted per 32 time steps. (b)  $a = 3.55$ ,  $D = 0.01$ , plotted per 32 time steps. (c)  $a = 3.6$ ,  $D = 0.01$ , plotted per 32 time steps. (d)  $a = 3.7$ ,  $D = 0.01$ , plotted per 32 steps. (e)  $a = 2.7$ ,  $D = 0.1$ , plotted per 32 time steps. (f)  $a = 2.7$ ,  $D = 0.2$ , plotted per 32 time steps. (g)  $a = 2.97$ ,  $D = 0.2$ , plotted per 32 time steps. (h)  $a = 3.4$ ,  $D = 0.1$ , plotted per 32 time steps. The system size is chosen to be 64. (i)  $a = 2.975$ ,  $D = 0.2$ , plotted per 32 steps. (j)  $a = 1.65$ ,  $D = 0.45$ , plotted per 512 time steps.

cannot evolve to a fully developed spatiotemporal chaotic pattern with increasing nonlinear parameter  $a$ . For instance, for the case  $D = 0.2$ , one finds that the maximum possible  $a$  value is just under 3 (Fig.3.5(c) and Fig.3.6(c)). But even for  $a = 2.975$ , some sites in the pattern are still laminar (Fig.3.9(i)) and the pattern belongs to a spatiotemporal intermittency class. A schematic diagram of this phenomenon is represented in Fig.3.10. The allowed range of the parameters  $a$  and  $D$  is below the black line. Between the blue and red lines is the regime of spatiotemporal intermittency, and to the right of red line is the regime of fully chaotic

### 3.1. COUPLED MAP LATTICES WITHOUT DELAY AND WITH CONSTANT DELAY

states. For some  $D$  values there is no allowed value of  $a$  with which the system can present fully chaotic states.

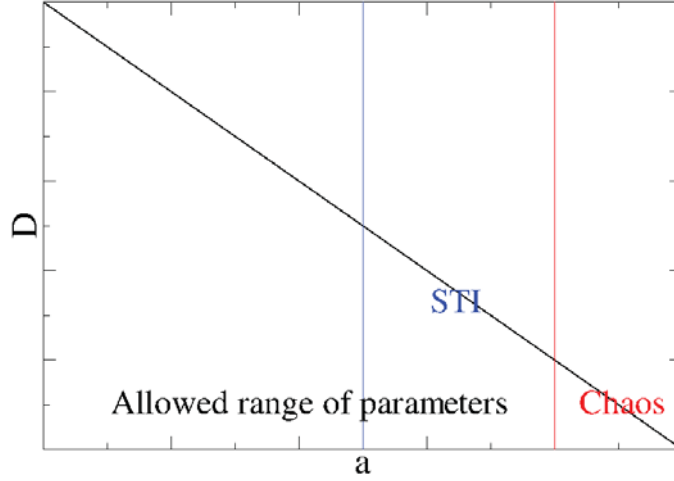


Figure 3.10: Schematic diagram of the allowed parameter range, spatiotemporal intermittency (STI), and fully chaotic states.

For large coupling strength  $D$ , the domain structure may not be fixed in time and traveling wave can be obtained (Fig.3.9(j)).

Additionally, in this model, one can see a new pattern. An example is shown in Fig.3.9(h). This pattern seems to be an exact inverse of the frozen random pattern. In this pattern, the large spatial domains contain periodic states and chaotic behavior can be seen in small domains. In contrast, in the frozen random patterns, it is the small domains that contain periodic states and chaotic behavior is present in the large domains. The difference between these two patterns is apparent in Fig.3.11.

In reference to the logistic map, with the nonlinear parameter  $a = 3.4$ , a periodic orbit with a period of 2 is obtained. Correspondingly, with this  $a$  value for a small coupling strength  $D$ , patterns with kinks is obtained (Fig. 3.9(a)). The state variable values 0.842 and 0.452 of the period orbit in an isolated logistic map are exactly the values of the state variables in the stable regions in this new pattern. And the chaotic regions between the stable regimes can be viewed as transitions between stable regimes. Without coupling, the state of each site is determined by its initial conditions. Starting from random initial conditions, a random configuration of the domain structure with many small domains will appear in the beginning. Due to the large coupling strength, small domains are eliminated, leading to the presence of only large domains. The transition between different domains is rough and chaotic.



### 3.1. COUPLED MAP LATTICES WITHOUT DELAY AND WITH CONSTANT DELAY

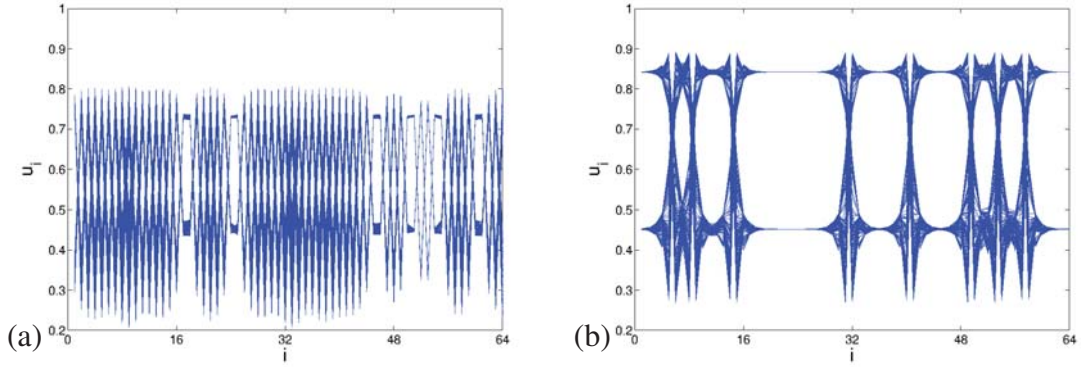


Figure 3.11: Space-plot referring to (a) Fig.3.9(f) and (b) Fig.3.9(h). The first 64 sites are plotted. The figure is generated by overlapping over 256 time steps.

#### 3.1.2 Coupled map lattice with constant delay

Now consider the coupled map lattice with constant delay. The model reads

$$u_{n+1}^i = au_n^i(1 - u_{n-T}^i) + D(u_n^{i+1} + u_n^{i-1} - 2u_n^i). \quad (3.3)$$

The bifurcation diagrams and the corresponding Lyapunov exponents are shown in Fig.3.12 and Fig.3.13. These figures suggest that for the case with constant delay, the  $P1 \rightarrow P2$  bifurcation point is no longer dependent on the coupling strength. For the case with a delay of  $T = 1$  the  $P1 \rightarrow P2$  bifurcation point is always at  $a = 2$ , which is also the bifurcation point of the delayed isolated logistic map with  $T = 1$ . In Fig.3.13(a)(b), the Lyapunov exponents for this case with different coupling strengths  $D$  are shown. One can see that the curves overlap perfectly in the neighborhood of  $a = 2$ . The range of allowed values of the nonlinear parameter  $a$  still depends on the coupling strength  $D$ . With increasing  $D$ , the allowed range of  $a$  will be compressed. Thus, for sufficiently large  $D$ , the maximum allowed value of  $a$  can be less than the  $P1 \rightarrow P2$  bifurcation point  $a$ , and one can only obtain the spatiotemporal homogeneous attractors.

As the delay is increased, the same behavior as for the delayed logistic map occurs. The  $P1 \rightarrow P2$  bifurcation point shifts to left. But just after the bifurcation point, there is a small chaotic region (see Fig.3.13(c)(d)) which does not exist in the case of  $T = 1$ . Examples of such chaotic states are shown in Fig.3.14. The delay is chosen to be  $T = 2$  and the coupling strength  $D = 0.01$ . For the nonlinear parameter  $a$ , two values are chosen. One is  $a = 1.63$ , which is in the chaotic region, with the maximal Lyapunov exponent  $\lambda = 0.002$ .

### 3.1. COUPLED MAP LATTICES WITHOUT DELAY AND WITH CONSTANT DELAY

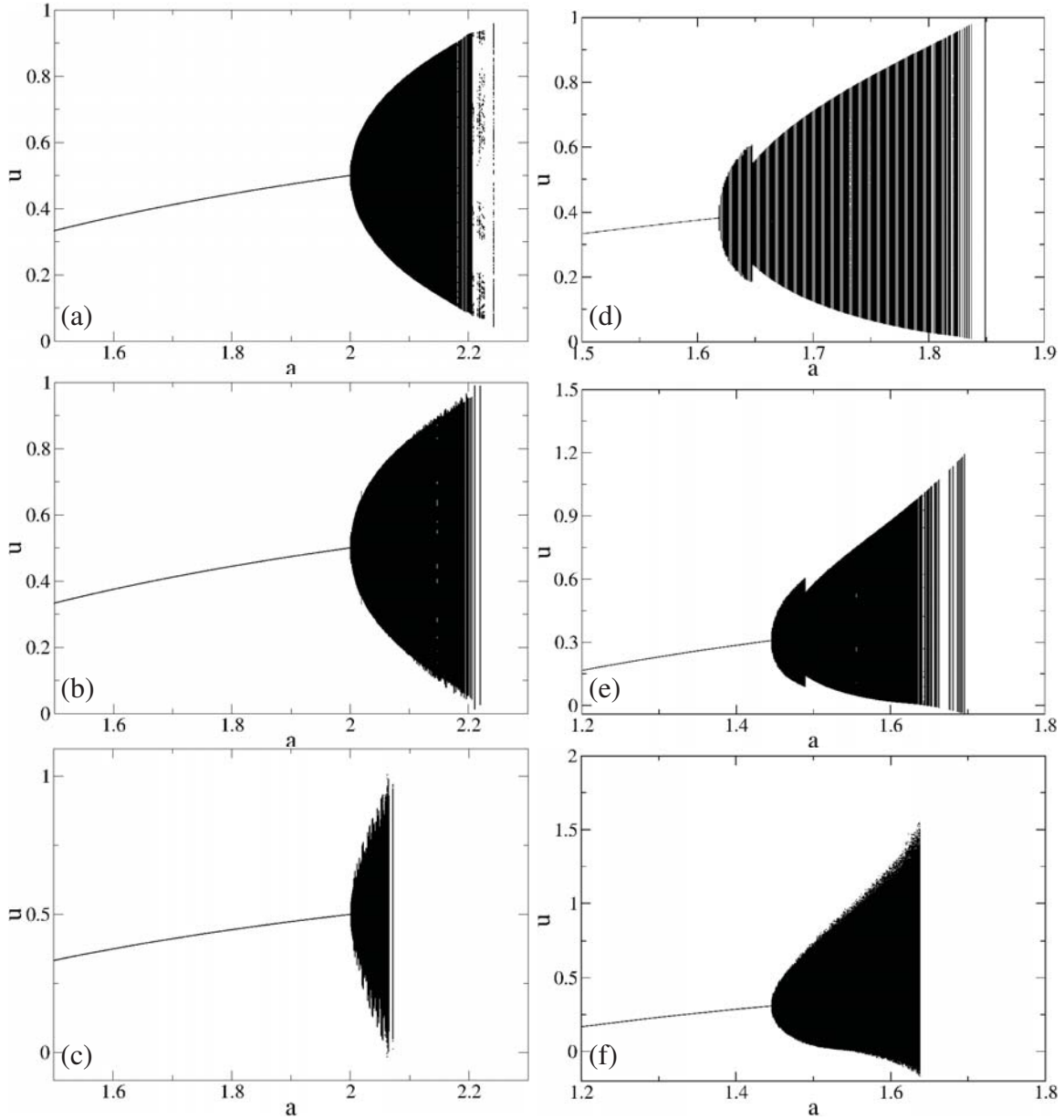


Figure 3.12: Bifurcation diagrams for Eq.(3.3). (a)  $T = 1, D = 0.01$ . (b)  $T = 1, D = 0.1$ . (c)  $T = 1, D = 0.2$ . (d)  $T = 2, D = 0.01$ . (e)  $T = 3, D = 0.01$ , (f)  $T = 3, D = 0.1$ .

The other is  $a = 1.66$ , with the maximal Lyapunov exponent  $\lambda = 0$ . The initial conditions are randomly selected near the unstable fixed point  $1 - \frac{1}{a}$  with a perturbation of 0.1. In the transitional chaotic region, the structure is weakly chaotic (Fig.3.14(a)). For the steady state, the structure is regular (Fig.3.14(b)).

### 3.1. COUPLED MAP LATTICES WITHOUT DELAY AND WITH CONSTANT DELAY

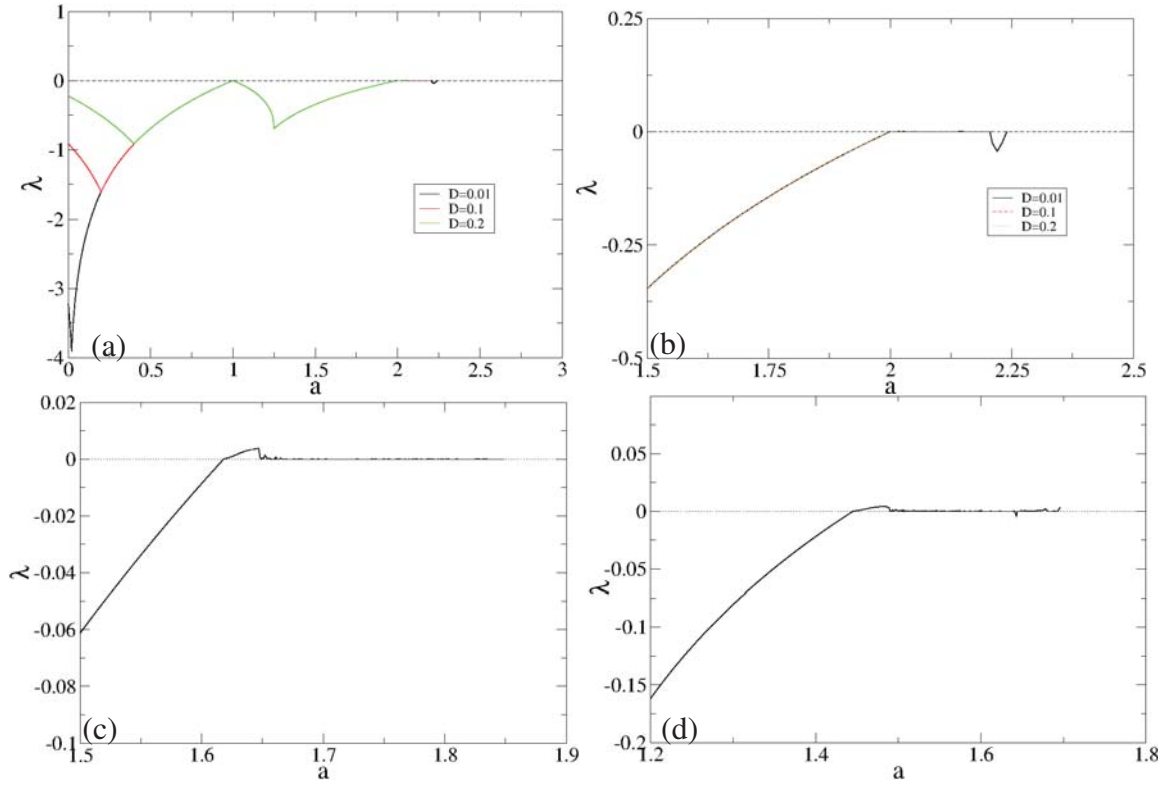


Figure 3.13: Maximal Lyapunov exponent as a function of  $a$  (a)  $T = 1$ , each different color refers to a different coupling strength. (b) Enlarged figure of (a). (c)  $T = 2$ ,  $D = 0.01$ . (d)  $T = 3$ ,  $D = 0.01$ .

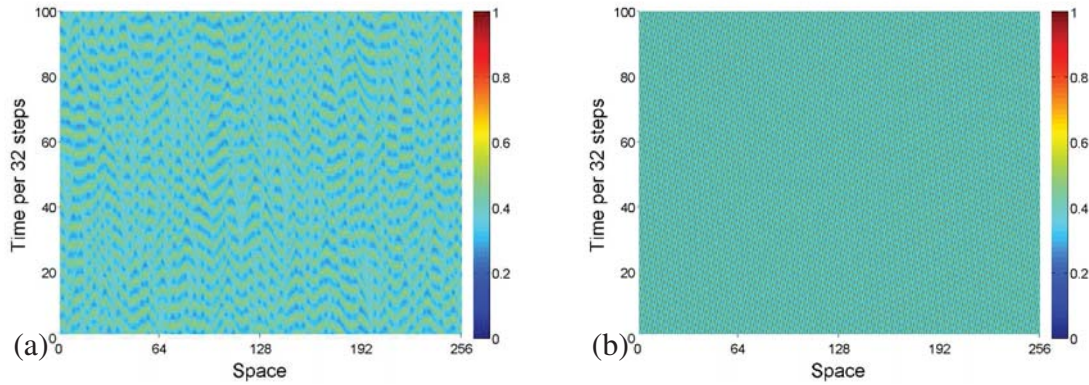


Figure 3.14: Space-time plot for Eq.(3.12) with  $T = 2$  and  $D = 0.01$ . The structure is generated from random initial conditions around an unstable fixed point  $1 - \frac{1}{a}$  and depicted after  $2 \cdot 10^5$  iterations. Periodic boundary conditions are considered. The system size is chosen to be 256. (a)  $a = 1.63$ , (b)  $a = 1.66$ .

### 3.1. COUPLED MAP LATTICES WITHOUT DELAY AND WITH CONSTANT DELAY

With delay present, only some patterns can be generated in this model. Here one can compare Fig.3.13 with Fig.3.6. While in the coupled map lattice without delay the dynamics are complex and abundant after the  $P1 \rightarrow P2$  bifurcation point, in the coupled map lattice with constant delay, the dynamics are relatively simple. For some constant delays, hardly any chaotic region can be observed after the bifurcation point. This means that chaotic patterns, such as fully developed spatiotemporal chaos, spatiotemporal intermittency, frozen random pattern, and pattern selection might not be found in a coupled map lattice with constant delays.

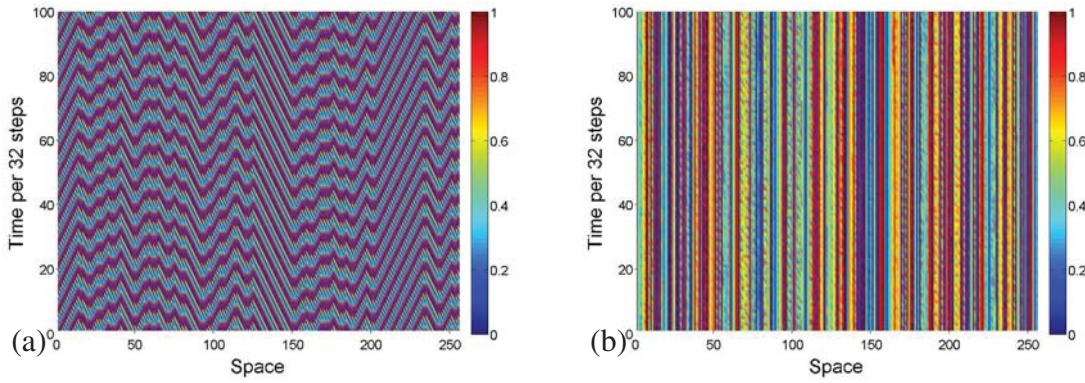


Figure 3.15: Space-time plot for Eq.(3.12) with  $T = 1$ . The structure is generated from random initial conditions around an unstable fixed point  $1 - \frac{1}{a}$  and depicted after  $2 \cdot 10^5$  iterations. Periodic boundary conditions are considered. The system size is chosen to be 256. (a)  $a = 2.235$ ,  $D = 0.01$ , and (b)  $a = 2.25$ ,  $D = 0.001$ .

For instance for the constant delay  $T = 1$ , one can observe a region with  $\lambda = 0$  after the bifurcation point. As the parameter  $a$  further increases, a stable region can be found for small coupling strengths, for instance  $D = 0.01$ . In this region there are some patterns with kinks. For example, with  $a = 2.235$  and  $D = 0.01$ , the pattern in Fig.3.15(a) can be generated. This pattern has a maximal Lyapunov exponent  $\lambda = -0.025$ . As the parameter  $a$  further increases, the system diverges to infinity for most coupling. Only for very weak coupling some chaotic structures can be found, for instance, with  $a = 2.25$  and  $D = 0.001$ . Here a pattern selection (see Fig.3.15(b)) with a maximal Lyapunov exponent  $\lambda = 0.066$  occurs.

The region with  $\lambda = 0$  after the  $P1 \rightarrow P2$  bifurcation point denotes another important effect resulting from the presence of delay. The traveling wave solution can be found even in the cases with weak coupling as well as in chaotic structure. Referring to Fig.3.14, one can

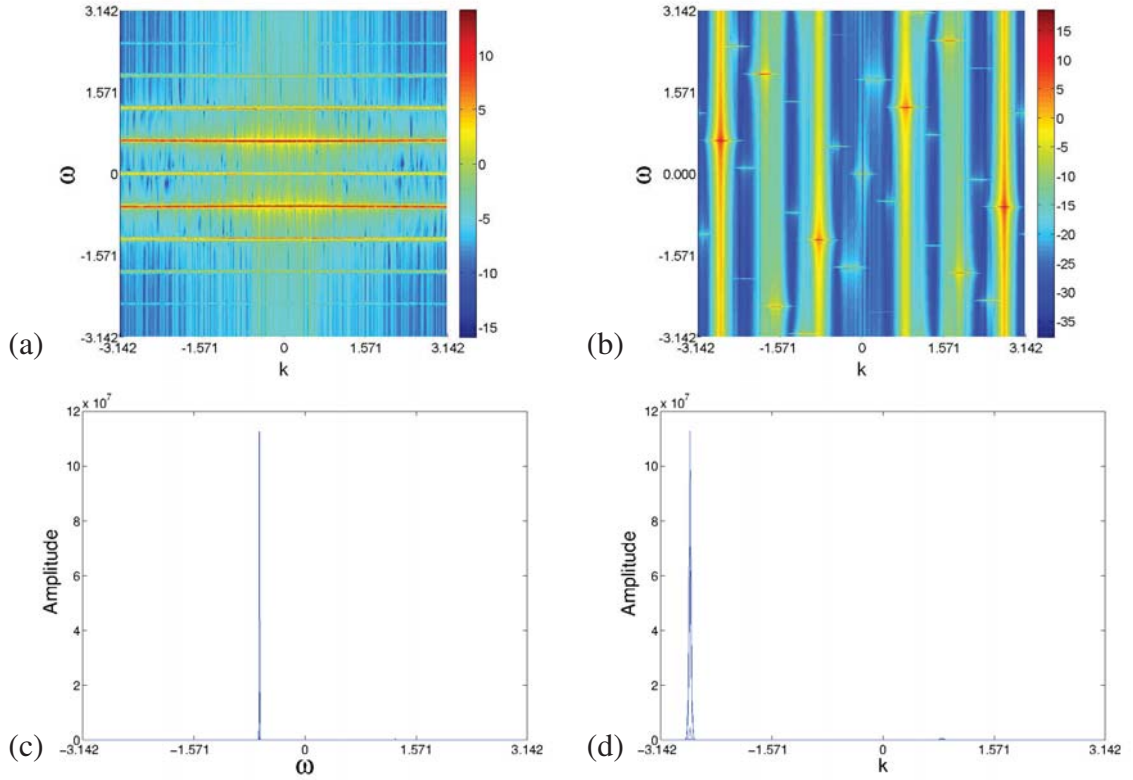


Figure 3.16: Dynamic structure factor (a) corresponding to the structure in Fig.3.14(a), (b) corresponding to the structure in Fig.3.14(b), (c) integration of the  $\omega$ -spectrum from (b) with  $k \leq 0$ , (d) integration of the  $k$ -spectrum from (b) with  $\omega \leq 0$

find some irregular structures in the chaotic state and a wave-shaped regular structure. This finding can be verified by using the dynamic structure factor. Fig.3.16(a)(b) show the dynamic structure factors corresponding to Fig.3.14(a)(b), respectively. The amplitude of the spectrum on a logarithmic scale is denoted with different colors. In the analysis, hamming window with size 999 is used. The dynamic structure factor is averaged over 100 samples. The dynamic structure factor for Fig.3.14(a) is rough, indicating chaotic behavior. In addition, this dynamic structure factor is not fully axially symmetric, which means that there are also spatial displacements in the structure. For the wave-shaped structure several pairwise occurring centrosymmetric peaks can be seen in the dynamic structure factor. For further analysis, the spectrum is integrated for  $k$  with  $\omega \geq 0$  and for  $\omega$  with  $k \geq 0$ , respectively (Fig.3.16(c)(d)). One can see that the spectrum is not symmetric and the highest peak is found at  $k \approx -2.70$  and  $\omega \approx -0.64$ . According to Fig.3.16(b), this pair of peaks is located at  $(-2.7, 0.64)$  and  $(2.7, -0.64)$ . As mentioned in Section 2.3.2, the velocity can be ob-



### 3.2. ANALYSIS OF THE BIFURCATION POINT SHIFT

tained as the negative slope of the line between two centrosymmetric peaks in  $k$ - $\omega$ -space. Determining the slope indicates that the velocity of wave has the value  $v = -\frac{\omega}{k} \approx 0.24$  site/iteration.

The wave solution is not artificial and the coupling strength  $D = 0.01$  is a weak coupling. One can find that with the presence of delay, even for weak coupling, the structures are no longer stationary in space. To verify that this phenomenon does not only occur for large delay, an example for the case of  $T = 1$  is shown in Fig.3.17. The nonlinear parameter is chosen to be  $a = 2.05$ . Random initial conditions and periodic boundary conditions are used. The system size is chosen to be 256. The structure is shown after  $2 \cdot 10^5$  transient iterations. In the temporal spectrum analysis, a hamming window with a size of 999 is applied. The dynamic structure factor is averaged over 100 samples. A spatially unfixed structure can be observed, and in the corresponding dynamic structure factor, some centrosymmetric peaks are present. These indicate the existence of the traveling wave solution.

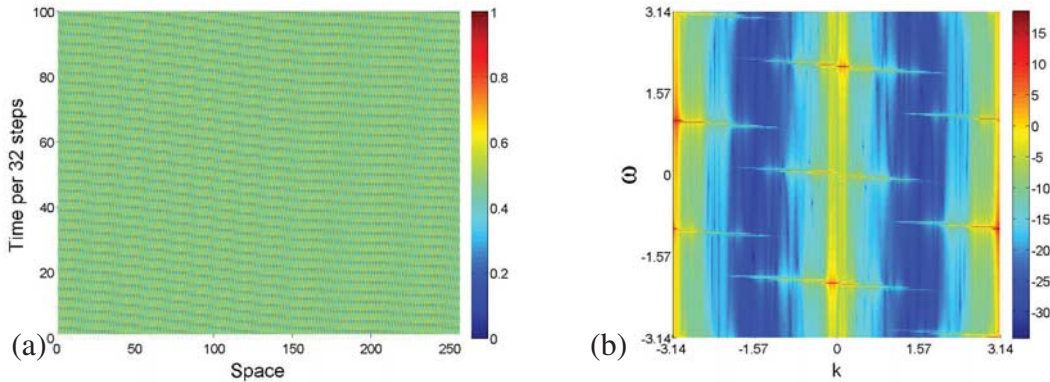


Figure 3.17: Space-time plot and the corresponding dynamic structure factor for Eq.(3.12) with  $T = 1$ ,  $a = 2.05$ , and  $D = 0.01$ . The amplitudes of the spectrum analysis are represented logarithmically with different colors.

### 3.2 Analysis of the bifurcation point shift

The previous results indicate that the bifurcation point becomes fixed in the presence of delay. To determine the reason for this phenomenon, the stability of the fixed point  $1 - \frac{1}{a}$  will be calculated. With spatial coupling, the Jacobian matrix  $J$  becomes the sum of the

extension matrix  $DF$  from the Jacobian matrix  $J_p$  for the isolated system and the coupling matrix  $C_D$ , where

$$DF = \begin{pmatrix} J_p & & & \\ & J_p & & \\ & & \ddots & \\ & & & J_p \end{pmatrix} \quad (3.4)$$

$$C_D = \begin{pmatrix} C_{DC} & C_{DN} & & & C_{DN} \\ C_{DN} & C_{DC} & C_{DN} & & \\ & \ddots & \ddots & \ddots & \\ & & \ddots & \ddots & \\ & & & C_{DN} & C_{DC} & C_{DN} \\ C_{DN} & & & & C_{DN} & C_{DC} \end{pmatrix} \quad (3.5)$$

$$C_{DC} = \begin{pmatrix} -2 \\ \end{pmatrix} \quad (3.6)$$

$$C_{DN} = \begin{pmatrix} 1 \\ \end{pmatrix}. \quad (3.7)$$

Here the matrices  $C_{DC}$  and  $C_{DN}$  have the same dimension as matrix  $J_p$ , which is determined by the isolated system. Only  $C_{DC}(1, 1) = -2$ ,  $C_{DN} = 1$ , and the rest are equal to 0.

The stability of the stationary state of the system is characterized by the eigenvalues of the Jacobian matrix  $J$ . If the absolute values of all eigenvalues are smaller than 1, the state is stable, otherwise it is unstable. Since the matrix  $DF$  characterizes the system dynamics corresponding to the local reaction term, the direct way to examine the influence of spatial coupling is to infer the eigenvalues of  $J$  from the eigenvalues of  $DF$  and  $C_D$ . But this idea

### 3.2. ANALYSIS OF THE BIFURCATION POINT SHIFT

---

leads to a mathematically unsolved problem: the relationship between the eigenvalues of the individual matrices and the eigenvalues of their sum. Even though many mathematicians have worked on this problem for about a hundred years, there are only some results for special matrices, for instance, the Hermitian matrices and normal matrices [49–51]. From another point of view, the coupled map lattice can be considered as a simple type of system with network coupling. The stability analysis for the network, which is based on the so-called master stability function, should also be applicable in this model.

Since the considered model is discrete, the corresponding master stability function should also be reformed for the discrete system. For the case without delay, the considered system can be written in the form

$$u_{n+1} = F(u_n) + D \cdot G \otimes H(u_n). \quad (3.8)$$

Notice here that  $D$  is  $\sigma$  in the definition of the master stability function in Eq.(2.9). And the linear equation for perturbation reads

$$\dot{\xi} = [I_N \otimes DF + D \cdot G \otimes DH] \xi. \quad (3.9)$$

For the case without delay, the state variable has only one component of each node, thus the matrix  $H(x) = 1$  and

$$G = \begin{pmatrix} -2 & 1 & & & -1 \\ 1 & -2 & -1 & & \\ & \ddots & \ddots & \ddots & \\ & & \ddots & \ddots & \ddots \\ & & & 1 & -2 & 1 \\ 1 & & & & 1 & -2 \end{pmatrix}. \quad (3.10)$$

The Jacobian function  $DF$  can be obtained from the linearized equation of the isolated iterate map

$$DF = a - 2au. \quad (3.11)$$

As discussed previously, this model has two fixed points  $u_1^* = 0$  and  $u_2^* = 1 - \frac{1}{a}$ . The loss of stability of the fixed point  $u_2^*$  is attributed to the considered bifurcation point. According to the master stability function method, the equation

$$|\xi_{(n+1)k}| = (a - 2au_2^* + D\gamma_k) |\xi_{nk}| \quad (3.12)$$



can be used here to calculate the stability of the fixed point  $u_2^*$ . Here  $\gamma_k$  is the  $k$ -th eigenvalue of the coupling matrix  $G$ . Since the perturbation is assumed to be  $|\xi_{nk}| = |\xi_{0k}|e^{\lambda_k n}$ , one obtains

$$e^{\lambda_k} = |2 - a + D\gamma_k|. \quad (3.13)$$

Thus, the the stability threshold of  $u_2^*$  is located at  $|2 - a + D\gamma_k| = 1$ .

- When  $|2 - a + D\gamma_k| > 1$ , the Lyapunov exponent is positive, the perturbation will grow up, and the state  $u_2^*$  is unstable.
- When  $|2 - a + D\gamma_k| < 1$ , the Lyapunov exponent is negative, the perturbation will shrink in size, and the state  $u_2^*$  is stable.

Recall that the diffusive coupling matrix  $G$  has eigenvalues  $\gamma_k \in [-4; 0]$  [36, 52, 53].

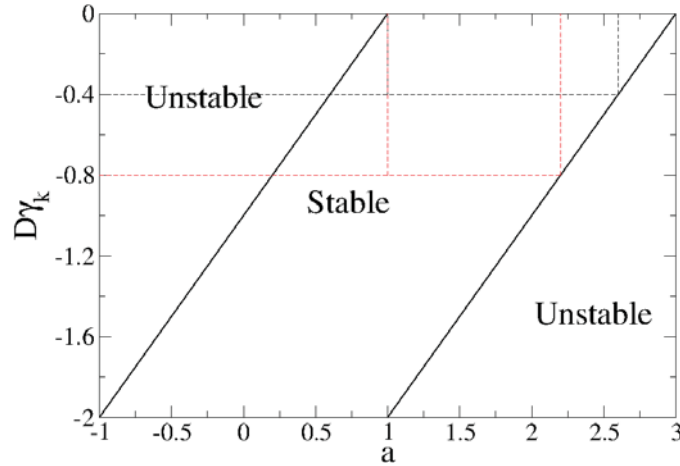


Figure 3.18: Stability distribution of Eq.(3.2) for the fixed point  $u_2^*$  in  $a$ - $D\gamma_k$ -space.

The boundaries of the stable region can be obtained from Eq.(3.13):

$$D\gamma_k = a - 1 \quad \text{and} \quad (3.14)$$

$$D\gamma_k = a - 3. \quad (3.15)$$

The stability of the fixed point  $u_2^*$  is determined by this system of equations. The fixed point is stable for a given parameter set  $a$  and  $D$  only when the fixed point is stable for all possible  $D\gamma_k$ . For the left boundary, corresponding to Eq.(3.14), there is a maximum  $a = 1$  for  $D\gamma_k = 0$ . This maximum exists for all  $D$ . Thus, the left boundary can be simplified as  $a = 1$ .

### 3.2. ANALYSIS OF THE BIFURCATION POINT SHIFT

The right boundary given by Eq.(3.15) describes the bifurcation point. The stability of  $u_2^*$  in terms of  $a$  and  $D\gamma_k$  is schematically represented in Fig.3.18. The results can be confirmed by comparing bifurcation diagrams. For instance, for a case with coupling strength  $D = 0.2$ , Eq.(3.15) gives a minimum  $a = 2.2$  for  $D\gamma_k \in [-0.8, 0]$  (see red dashed line in Fig.3.18). Thus, the bifurcation point for  $D = 0.2$  is located at  $a = 2.2$ , as can be seen in Fig.3.5(c). And for the case with coupling strength  $D = 0.1$ ,  $a = 2.6$  ( see black dashed line in Fig.3.18). This result can also be used for comparison with Fig.3.5(b).

Now consider the coupled map lattice with a constant delay. The presence of delay effectively adds other dimensions to phase space, thereby expanding it. Here the analysis for a case with delay  $T = 1$  is presented. For larger delay, the analysis can be performed in the same way.

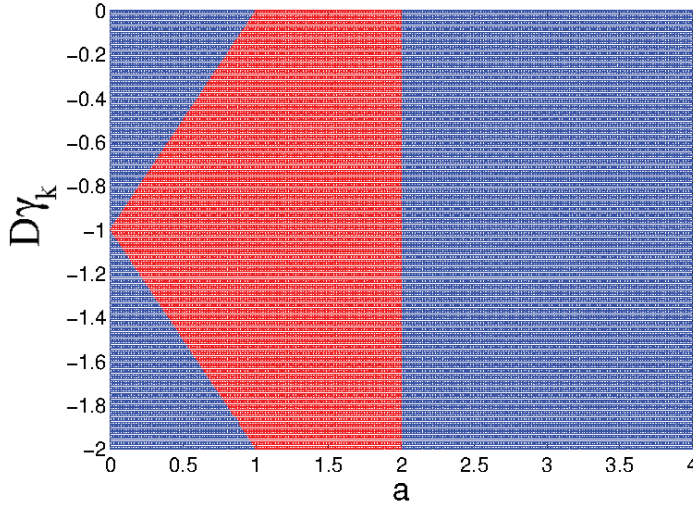


Figure 3.19: Stability distribution for Eq.(3.12) with a constant delay of  $T = 1$  in  $a$ - $D\gamma_k$ -space. Red: stable. Blue: unstable.

For the local reaction dynamics

$$u_{n+1} = au_n(1 - u_{n-1}), \quad (3.16)$$

the Jacobian matrix is

$$DF = J_p = \begin{pmatrix} a(1 - u_{n-1}) & -au_n \\ 1 & 0 \end{pmatrix}. \quad (3.17)$$

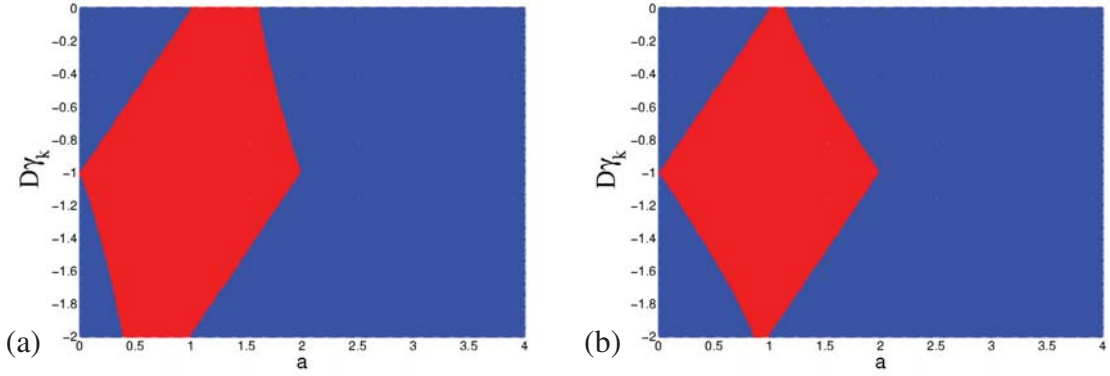


Figure 3.20: Stability distribution for Eq.(3.12) with constant delay (a)  $T = 2$ , (b)  $T = 10$  in  $a$ - $D\gamma_k$ -space. Red: stable. Blue: unstable.

Since the spatial coupling is only applied on the component  $u_n$ , the matrix

$$H = \begin{pmatrix} u_n & 0 \\ 0 & 0 \end{pmatrix}, \quad (3.18)$$

so that

$$DH = \begin{pmatrix} 1 & 0 \\ 0 & 0 \end{pmatrix}. \quad (3.19)$$

Considering of the stability of the fixed point  $u_2^* = 1 - \frac{1}{a}$ , the Jacobian matrix, which is obtained through the master stability equation, has the form

$$\begin{aligned} J &= DF(u_2^*) + D\gamma_k DH = \begin{pmatrix} a(1-u_2^*) & -au_2^* \\ 1 & 0 \end{pmatrix} + D\gamma_k \begin{pmatrix} 1 & 0 \\ 0 & 0 \end{pmatrix} \\ &= \begin{pmatrix} 1 + D\gamma_k & 1 - a \\ 1 & 0 \end{pmatrix}. \end{aligned} \quad (3.20)$$

Thus, one can calculate the Lyapunov exponents from this class of Jacobian matrices with different  $a$  and  $D\gamma_k$  values. Fig.3.19 shows the stability distribution in this case. The stable region is indicated by red, and the unstable region is indicated by blue. For a diffusive coupling, the coupling strength is generally not larger than 0.5, thus  $D\gamma_k \leq 2$ . The figure shows that for  $D = D \in [0, 0.5]$ , the fixed point  $u_2^* = 1 - \frac{1}{a}$  is always stable for  $a \in [1, 2]$ . Hence the bifurcation point is fixed.

For the case with larger delay, the Jacobian matrix of the local reaction has a larger dimension  $T + 1$ . The spatial coupling is always only applied on  $u_n$ , therefore the matrix  $DH$  is a

$(T + 1) \times (T + 1)$  matrix with  $DH(1, 1) = 1$  and the rest equal to 0. Hence, in this case, the stability for fixed point  $u^*$  can also be analytically calculated through the Jacobian matrices with a general form

$$\begin{aligned}
 J &= DF(u^*) + D\gamma_k DH \\
 &= \begin{pmatrix} a(1 - u^*) & & & -au^* \\ 1 & & & \\ & \ddots & & \\ & & \ddots & \\ & & & \ddots \end{pmatrix} + D\gamma_k \begin{pmatrix} 1 & & & \\ & & & \\ & & & \\ & & & \end{pmatrix} \\
 &= \begin{pmatrix} a(1 - u^*) + D\gamma_k & & & -au^* \\ 1 & & & \\ & \ddots & & \\ & & \ddots & \\ & & & \ddots \end{pmatrix}.
 \end{aligned} \tag{3.21}$$

Here  $J$  is a  $(T + 1) \times (T + 1)$  matrix with  $J(1, 1) = a(1 - u^*) + D\gamma_k$ ,  $J(1, T + 1) = -au^*$  and a secondary diagonal occupied by the value 1. The rest is equal to 0.

As examples, the stability exponent for the fixed point  $u_2^* = 1 - \frac{1}{a}$  for case with constant delay  $T = 2$  and  $T = 10$  are calculated and the resulting stability distributions are shown in Fig.3.20. The figure shows that for large delay, the right boundary of the stable region is no longer  $D\gamma_k$ -independent. With the help of the master stability function, a state is stable only when all stability exponents for the corresponding  $D\gamma_k$  values have negative real parts. So for the boundary in Fig.3.20, the minimum of  $a$  on the right boundary can be found by  $D\gamma_k = 0$  when  $D\gamma_k$  is less than a certain value. This means the bifurcation point is fixed before the coupling strength  $D$  reaches a certain value.

For instance, for the case with a constant delay  $T = 2$ , when the coupling strength is less than a certain value, such as  $D = 0.1, 0.2$ , and  $0.3$ , giving a corresponding range of  $D\gamma_k$   $[-0.4; 0]$ ,  $[-0.8; 0]$ , and  $[-1.2; 0]$ , respectively,  $a = 1.61$  at  $D\gamma_k = 0$  is the minimum of  $a$  on the right boundary. This means that the bifurcation point is located at  $a = 1.61$ . When the coupling strength increases beyond a certain value, for instance,  $D = 0.4$ , corresponding to a range of  $D\gamma_k$   $[-1.6; 0]$ , the minimum of  $a$  on the right boundary is  $a = 1.4$  at  $D\gamma_k = -1.6$  for this case. This means that the bifurcation point is located at  $a = 1.4$ . This result can be confirmed by the bifurcation diagram or Lyapunov exponent as a function of  $a$ . In Fig.3.21,

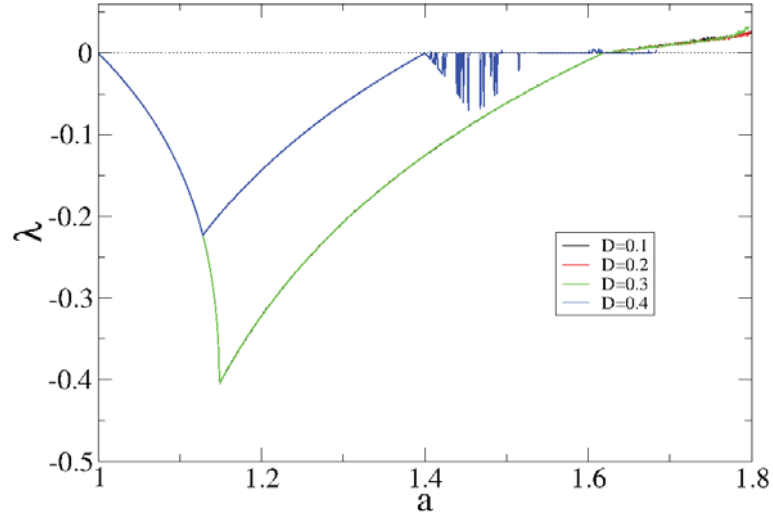


Figure 3.21: Lyapunov exponent as a function of  $a$  for Eq.(3.12)  $T = 2$ .

the Lyapunov exponents as functions of the nonlinear parameter  $a$  for Eq.(3.12) with  $T = 2$  for different coupling strengths are shown. One can see that the bifurcation point is fixed at  $a = 1.61$  for  $D = 0.1$  (black line),  $0.2$  (red line), and  $0.3$  (green line). It is shifted to left only when  $D$  is very large (see blue line,  $D = 0.4$ ).

The reason for this phenomenon is based on the Lyapunov exponents. For the delay  $T = 1$ , the eigenvalue can be calculated from the Jacobian matrix (3.21) and can be obtained from

$$L^2 - (1 + D\gamma_k)L + (a + 1) = 0, \quad (3.22)$$

where  $L$  is the eigenvalue. For this equation,  $\Delta = (1 + D\gamma_k)^2 - 4(a + 1)$ . For this study,  $D\gamma_k \in [0, 2]$  and  $a$  is in the neighborhood of 2. Thus  $\Delta$  is always negative, which means the eigenvalues are a pair of complex conjugate numbers with the same module. Hence, this pair of eigenvalues can be considered as one. The right boundary of the stable region therefore depends only on one eigenvalue. But for large  $T$ , one obtain  $T + 1$  Lyapunov exponents, which contains several pairs of complex conjugate numbers, real numbers, and pure imaginary numbers. The stability is determined by the largest one of them and may have a different behavior when  $D\gamma_k$  changes. So the zig of the right boundary of the stable region can be caused by the switch of positions in the Lyapunov sequence.module.

### 3.3 Coupled map lattices with fluctuating delay

Now coupled map lattices with spatially and temporally fluctuating delay are investigated. With regard to the time variation of the delay, this section concentrates on the periodic case. The spatial variation of the delay can also be classified as two different cases: the synchronized case and nonsynchronized case. For the synchronized case, the delay is only dependent on time, which means that at any time step  $n$ , all nodes have the identical delay. For nonsynchronized case the delay is dependent on both time and space. The initial delays on the different nodes are randomly selected and varies with the same periodic sequence, which means there is a random phase shift between the time evolution of the delays on different nodes.

For simplicity, in this study, the delay is only considered to fluctuate between two different values. More precisely, the time evolution of the delay is described by a step function:

$$T(n) = \begin{cases} T_1 & \text{if } n \bmod T_p < T_{p1} \\ T_2 & \text{otherwise} \end{cases}, \quad (3.23)$$

where  $T_1 < T_2$ , and  $T_p$  is the period of the delay and  $T_{p1}$  is the duration where the delay takes the value  $T_1$ .

#### 3.3.1 Synchronized periodic delay

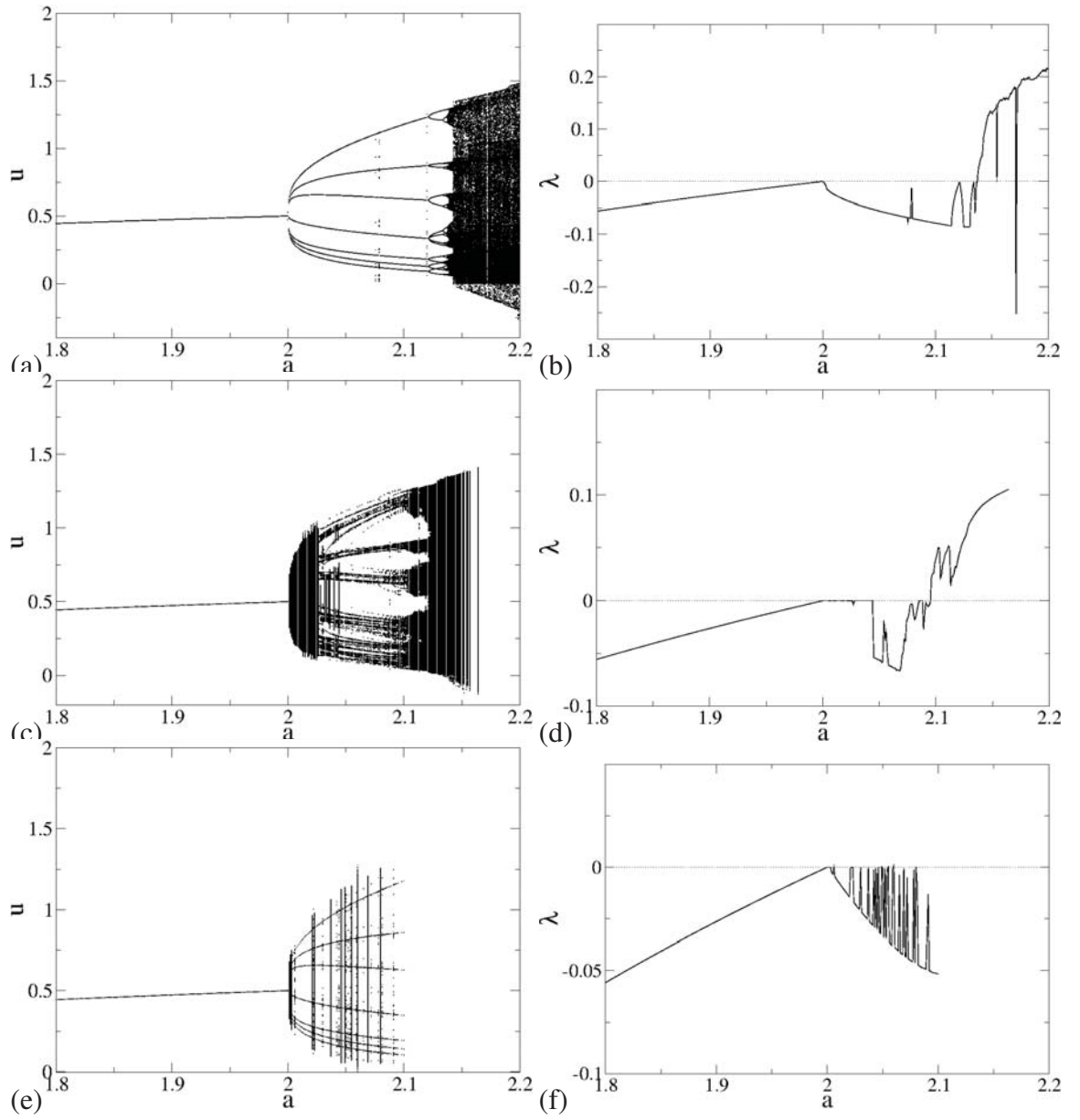
This section discusses the case with synchronized periodic delay. First, the delays  $T_1$  and  $T_2$  are chosen to be 1 and 2, respectively, and the durations  $T_p = 2$ , and  $T_{p1} = 1$ . The bifurcation diagram and the Lyapunov exponent as a function of the nonlinear parameter  $a$  for different coupling strengths are shown in Fig.3.22. Here two interesting phenomena can be observed. One is the bifurcation point, where the spatially homogeneous state loses its stability. It is fixed on  $a = 2$ , which is also the bifurcation point for the case with a constant delay of  $T = 1$ . The other is the dynamics after the bifurcation. In comparison with the case with constant delay, the dynamics in this case are much more complex and abundant. A typical phenomenon is the existence of stable states. In the case of fluctuating delay, one can observe a large periodic window.

For the stability analysis of the homogeneous state, the master stability function can be used. As calculated previously, in this case, the Jacobian matrices can be written as

$$J_1 = \begin{pmatrix} a(1 - u_2^*) + D\gamma_k & -au_2^* & 0 \\ 1 & 0 & 0 \\ 0 & 1 & 0 \end{pmatrix} \quad (3.24)$$

for a delay of  $T_1 = 1$  and

$$J_2 = \begin{pmatrix} a(1 - u_2^*) + D\gamma_k & 0 & -au_2^* \\ 1 & 0 & 0 \\ 0 & 1 & 0 \end{pmatrix} \quad (3.25)$$



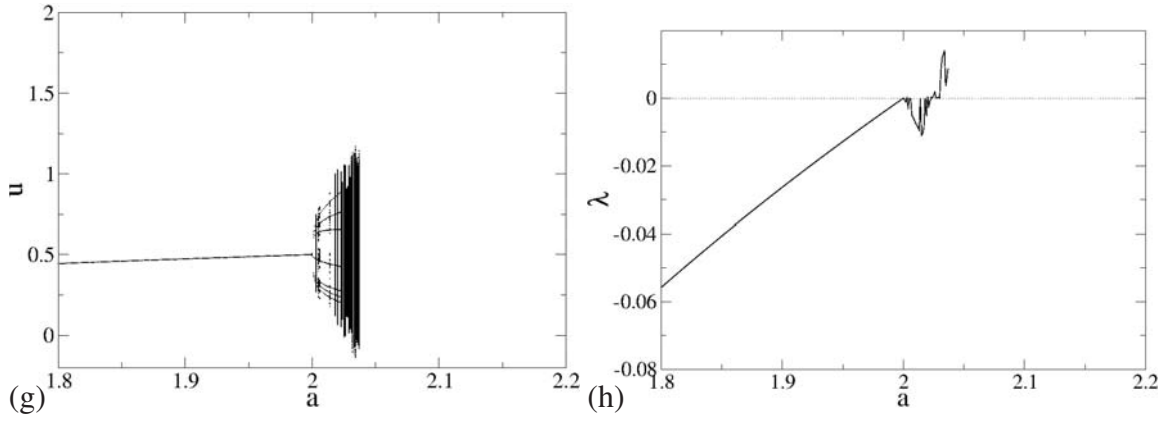


Figure 3.22: Bifurcation diagrams and Lyapunov exponents for coupled map lattices with synchronized periodic delay,  $T_1 = 1$ ,  $T_2 = 2$ ,  $T_p = 2$ , and  $T_{p1} = 1$ . The results are obtained from random initial conditions and depicted after  $5 \cdot 10^5$  iterations. Periodic boundary conditions are considered. The system size is chosen to be 100. (a),(b)  $D = 0$ , (c),(d)  $D = 0.01$ , (e),(f)  $D = 0.1$ , (g),(h)  $D = 0.2$ .

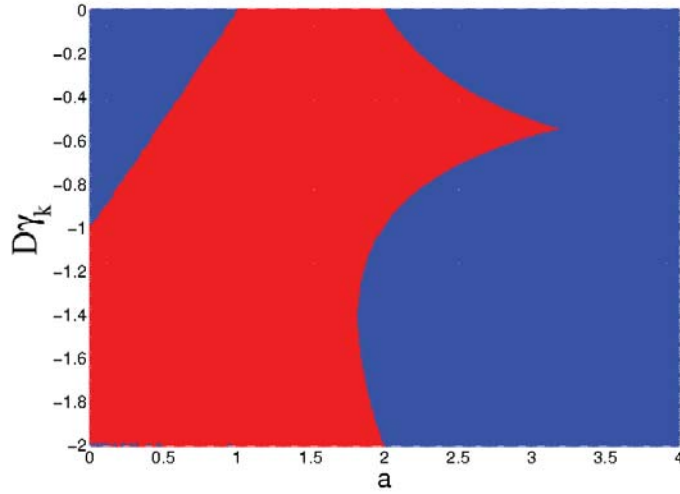


Figure 3.23: Stability distribution for Eq.(3.12) with synchronized periodic delay  $T_1 = 1$ ,  $T_2 = 2$ ,  $T_p = 2$  and  $T_{p1} = 1$  in  $a$ - $D\gamma_k$ -space. Red: stable. Blue: unstable.

for a delay of  $T_2 = 2$ . Thus the stability of the fixed point  $u_2^*$  can be determined by the eigenvalues of the matrix  $J_1 J_2$ . Fig.3.23 shows the stability distribution for this case. The stable region is indicated by red color and the unstable region by blue. The right boundary of the stable region is similar to the case with a large constant delay. The minimum of  $a$  is located at  $D\gamma_k = 0$  when  $D\gamma_k$  is less than 1. For the examples in Fig.3.22, the maximum



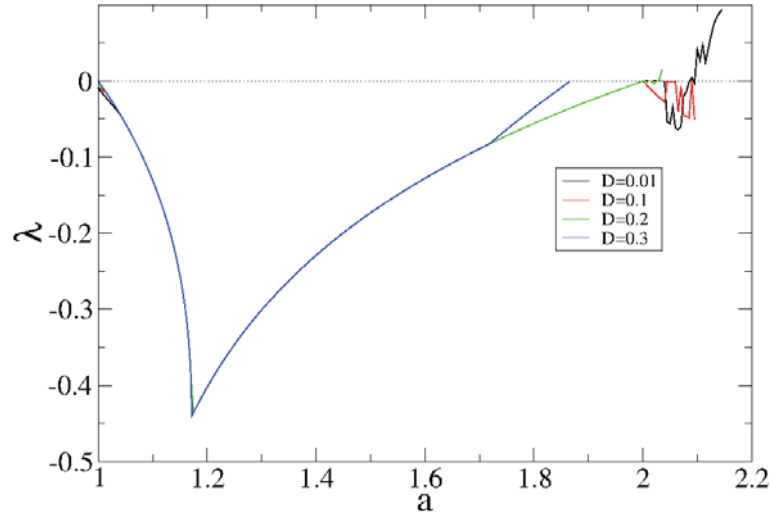


Figure 3.24: Maximal Lyapunov exponent as a function of  $a$  for Eq.(3.12) with synchronized periodic delays  $T_1 = 1$ ,  $T_2 = 2$ ,  $T_p = 2$ , and  $T_{p1} = 1$  under different coupling strength.

of the selected coupling strengths is 0.2, which corresponds to  $D\gamma_k \in [0, -0.8]$ . So that the bifurcation point appears to be fixed. Furthermore, the Lyapunov exponent as a function of  $a$  for different coupling strengths  $D$  is shown in Fig.3.24. Here one can see that the bifurcation point is fixed for small coupling strengths  $D = 0.01$  (black line),  $D = 0.1$  (red line), and  $D = 0.2$  (green line). For a large coupling strength  $D = 0.3$  (blue line), it is shifted to the left. Note that for case with a constant delay of  $T = 2$ , the domain of  $a$  is smaller than the case with a constant delay of  $T = 1$ . Even for small  $D$  values after  $a \approx 1.8$ , the system states diverge to infinity. Correspondingly, for the case with fluctuating delay with  $D = 0.3$ , the system states also diverge to infinity right after the fixed point loses its stability and there are no finite states after the bifurcation.

When  $T_2$  increases, the behavior of the bifurcation point changes. First, when the difference between the two delays is not very large, the bifurcation point is shifted to the left and fixed there; for instance, see the cases with a delay of  $T_2 = 3$  or  $T_2 = 7$  (see Fig.3.25(a)(b)). As  $T_2$  further increases, one obtains an asymptotic shape of the stability distribution (see Fig.3.25). When  $D\gamma_k = 0$ , the bifurcation point is located at  $a = 1.99$ , which is slightly to the left of the bifurcation point  $a = 2$  for the case with a constant delay of  $T = 1$ . This can be explained by the dynamic behavior of a delay system with large delays. For a constant delay system with delay  $\tau \rightarrow \infty$ , the Lyapunov spectrum for an unstable state can be asymptotically split into a point-like component which remains finite and an ordinary spectral component  $\lambda$  which

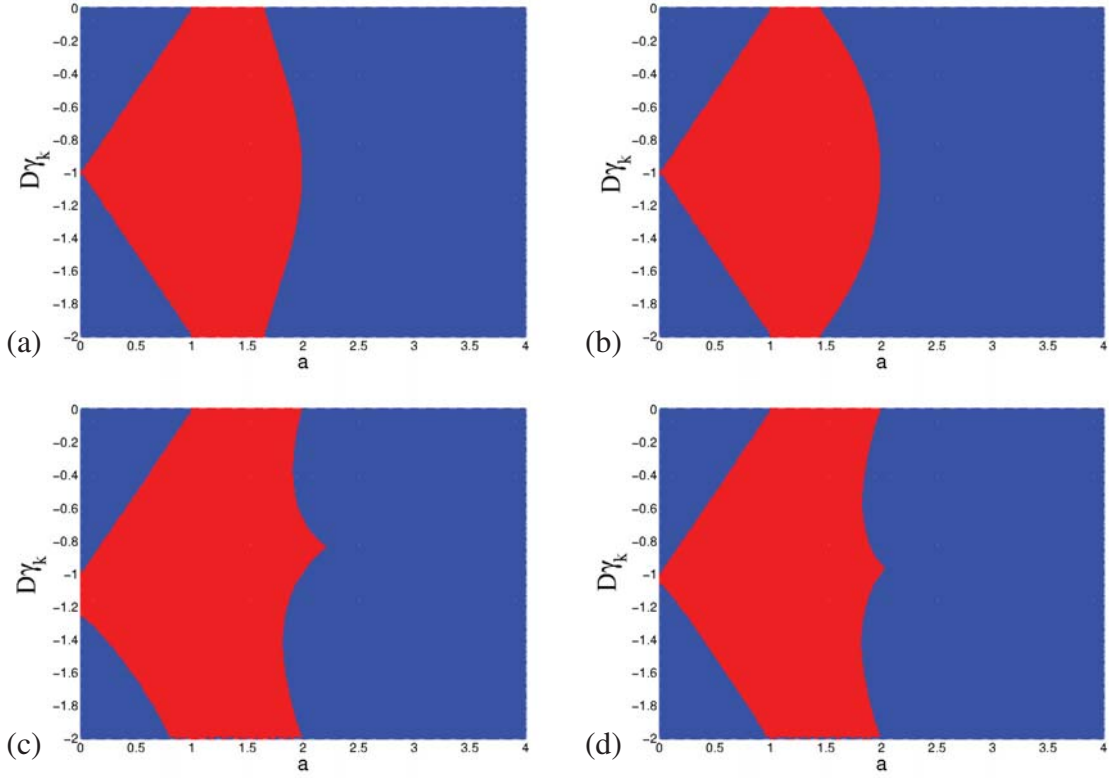


Figure 3.25: Stability distribution for Eq.(3.12) with synchronized periodic delay with fixed  $T_1 = 1$ ,  $T_p = 2$ , and  $T_{p1} = 1$  for different  $T_2$  values in  $a$ - $D\gamma_k$ -space. (a)  $T_2 = 3$ , (b)  $T_2 = 7$ , (c)  $T_2 = 10$ , and (d)  $T_2 = 50$ . Red: stable. Blue: unstable.

satisfies

$$\lambda_\tau \cdot \tau \approx \Lambda \quad \text{as } \tau \rightarrow \infty. \quad (3.26)$$

Here  $\Lambda$  is a constant spectrum which can be analytically calculated [54, 55]. For coupled map lattices with delay (Eq.(3.3)), the linearized equation can be written as

$$\delta \vec{u}_{n+1} = A \delta \vec{u}_n + B \delta \vec{u}_{n-T} + D \cdot G \otimes \delta \vec{u}_n, \quad (3.27)$$

where  $\delta \vec{u}_n = (\delta u_n^1, \delta u_n^2, \dots, \delta u_n^L)$ ,  $L$  is the spatial size.  $A$  and  $B$  are the matrices which are based on the partial differential of the local iteration after  $u_n^i$  and  $u_{n-T}^i$ , and  $G$  is the coupling matrix. The perturbation can be written as  $\delta \vec{u}_n = \delta \vec{u}_0 e^{sn}$ , where  $s$  is the stability exponent and the real part of  $s$  is the Lyapunov exponent  $\lambda$ . Thus, Eq.(3.27) can be written as

$$\delta \vec{u}_0 e^s = A \delta \vec{u}_0 + B \delta \vec{u}_0 e^{-sT} + D \cdot G \otimes \delta \vec{u}_0. \quad (3.28)$$

As the maximal Lyapunov exponent is positive for  $T \rightarrow \infty$ , the second part of Eq.(3.28) can be neglected. Thus, the maximal Lyapunov exponent converges to a certain value when the delay  $T \rightarrow \infty$ . For the case with fluctuating delay, the boundary between stable and unstable regions is determined by the interaction between the stability properties for the cases with constant delays.

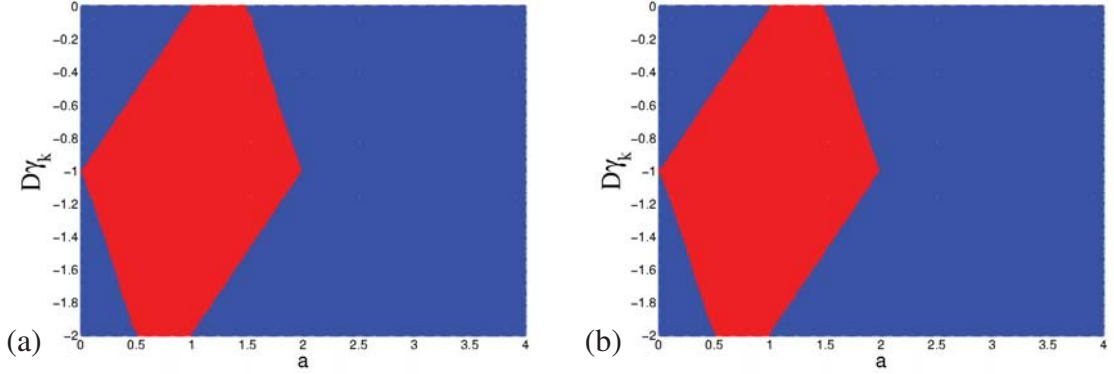


Figure 3.26: Stability distribution for Eq.(3.12) with synchronized periodic delay with fixed  $T_p = 2$ ,  $T_{p1} = 1$ , and  $T_1 = 2$  for different  $T_2$  values in  $a$ - $D\gamma_k$ -space. (a)  $T_2 = 50$ , (b)  $T_2 = 100$ . Red: stable. Blue: unstable.

For the cases with fluctuating delays, the stability property is influenced by the stability properties for cases with the corresponding constant delays. Since  $T_1$  is fixed and there is an asymptotic state for  $T_2 \rightarrow \infty$ , asymptotic states may be obtained when the difference between the considered delays  $\Delta T = (T_2 - T_1) \rightarrow \infty$ . In Fig.3.26, an example is shown. Here the delay  $T_1$  is fixed at 2, and  $T_2$  is chosen to be 50 in (a) and 100 in (b). One can see that both distribution diagrams appear identical. For  $D\gamma_k = 0$ , the right boundary between the stable and unstable regions is located at  $a \approx 1.48$ . Compare this with the stability distribution diagram for the case with a constant delay of  $T = 2$  (see Fig.3.20(a)). There the boundary is located at  $a \approx 1.61$  for  $D\gamma_k = 0$ .

Now the dynamic behaviors after the bifurcation are studied. As the dynamics after the bifurcation point are complex in this case, the same patterns which can be generated in the Kaneko model (3.1) and the model of coupled map lattices without delay (3.2) can also be generated in this case. Some examples are shown in Fig3.27. Compare with the patterns in Figs.3.2 and 3.9. The focus here is the study of new phenomena, which will be discussed in the following text.

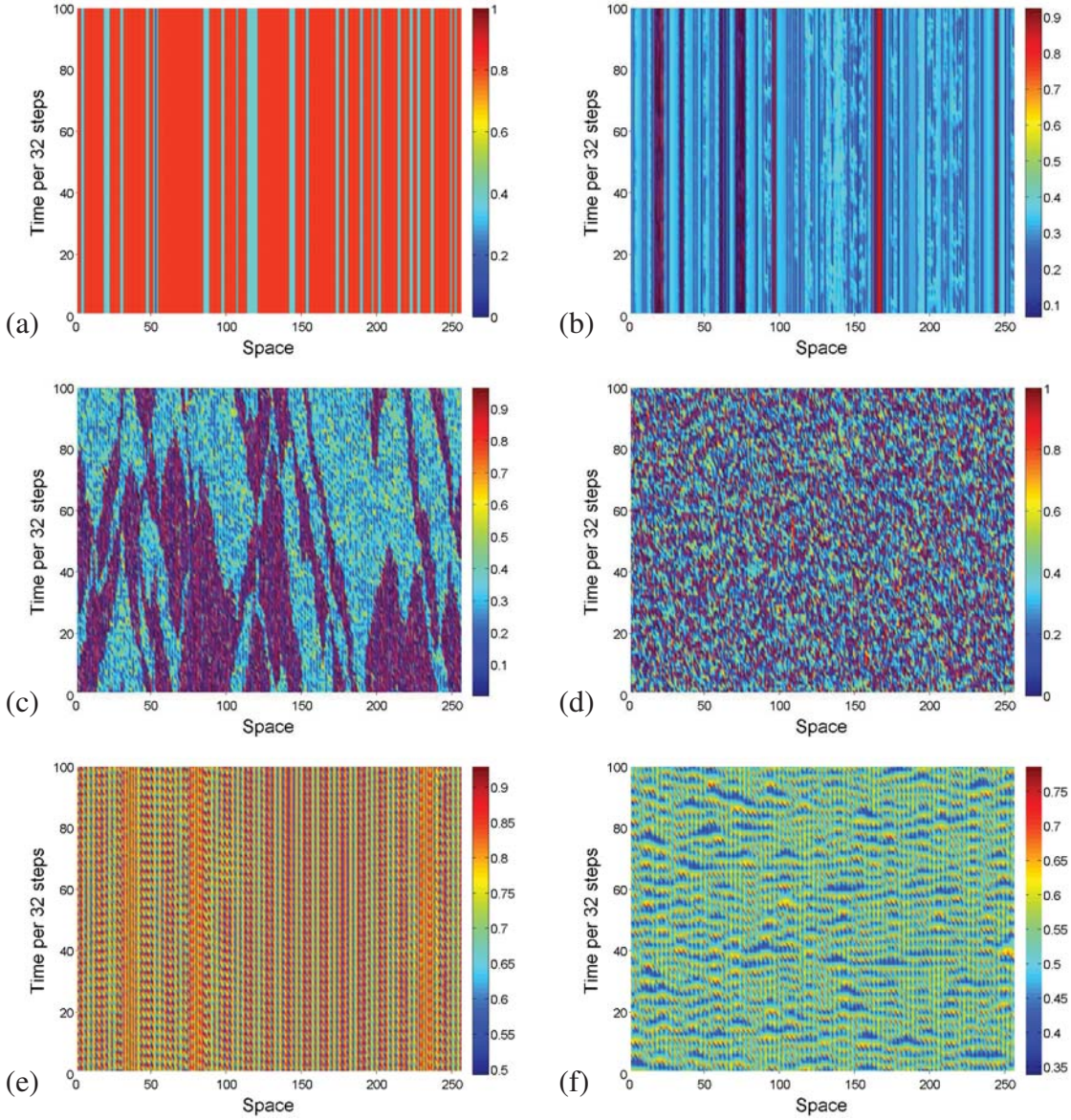


Figure 3.27: Examples of different patterns which can be generated by the coupled map lattice with fluctuating delay.  $T_1 = 1$ ,  $T_2 = 2$ ,  $T_p = 2$ , and  $T_{p1} = 1$ . The patterns are generated from random initial conditions and depicted after  $2 \cdot 10^5$  iterations. Periodic boundary conditions are considered. The system size is chosen to be 256. The structure is plotted per 32 time steps. (a)  $a = 2.05$ ,  $D = 0.01$ , (b)  $a = 2.12$ ,  $D = 0.01$ , (c)  $a = 2.13$ ,  $D = 0.01$ , (d)  $a = 2.15$ ,  $D = 0.01$ , (e)  $a = 2.03$ ,  $D = 0.2$ , (f)  $a = 2.035$ ,  $D = 0.2$ .



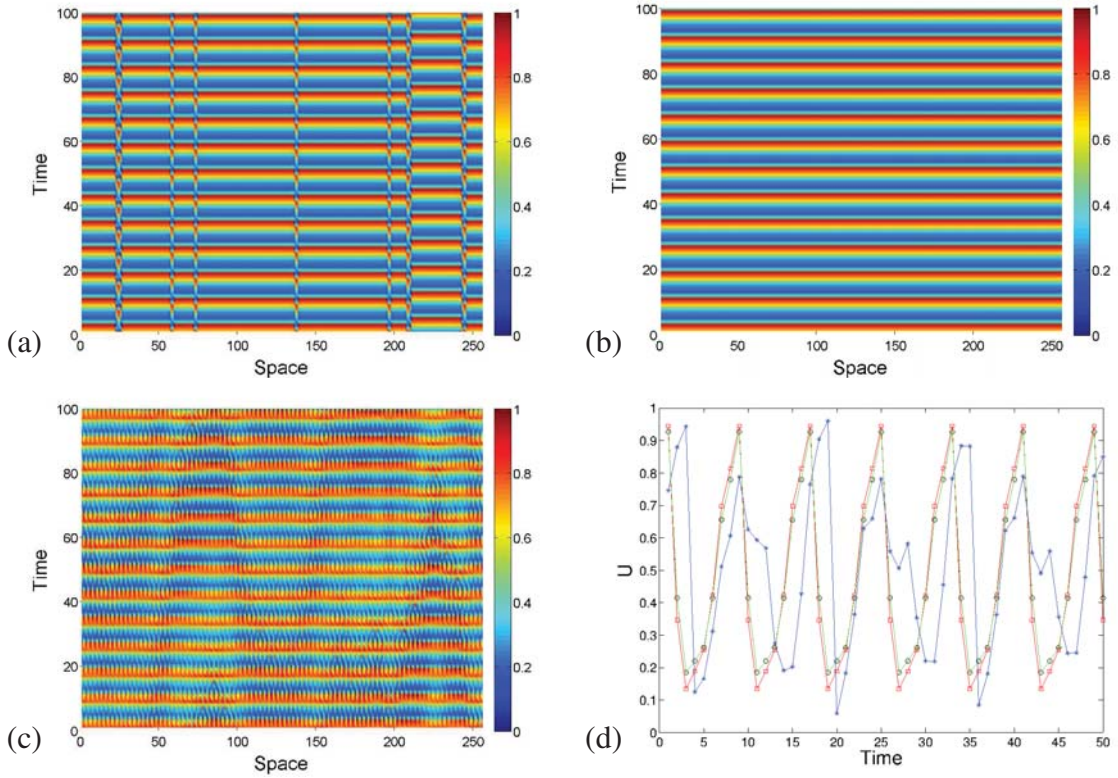


Figure 3.28: Space-time plots (a)(b)(c) and the related temporal trajectory at one site (d) of Eq.(3.12) with synchronized periodic delay,  $T_1 = 1$ ,  $T_2 = 2$ ,  $T_p = 2$ ,  $T_{p1} = 1$ , and  $a = 2.03$ . The patterns are generated from a random initial conditions and depicted after  $2 \cdot 10^5$  iterations. Periodic boundary conditions are considered. The space size is chosen to be 256. (a)  $D = 0.01$ , plotted per time step. (b)  $D = 0.1$ , plotted per time step. (c)  $D = 0.2$ , plotted per time step. (d) Black:  $D = 0$ , red:  $D = 0.01$  at site  $x = 23$ , green:  $D = 0.1$  at site  $x = 50$ , blue:  $D = 0.2$  at site  $x = 50$ .

One effect of the fluctuating delay and spatial coupling is the enhancement of a state's stability. In Fig.3.28, an example is shown. Here the delays are chosen to be  $T_1 = 1$ ,  $T_2 = 2$ , and the duration are chosen to be  $T_p = 2$  and  $T_{p1} = 1$ . The nonlinear parameter is  $a = 2.03$ . The space-time plot for different spatial couplings  $D$  are shown with initial conditions randomly perturbed from the unstable fixed point  $1 - \frac{1}{a}$  with an amplitude 0.1. When the spatial coupling is absent, a periodic orbit with a period of 8 is obtained. The temporal trajectory of a site is shown in Fig.3.28(d) with a black dashed line and black circles. In this figure, the green line with crosses, which is the temporal trajectory at one site for the case

of  $D = 0.1$ , exactly overlaps the black line with circles. The corresponding space-time plot shows it is a fully synchronized state (see Fig3.28(b)). The system has a maximal Lyapunov exponent  $\lambda = -0.02$ .

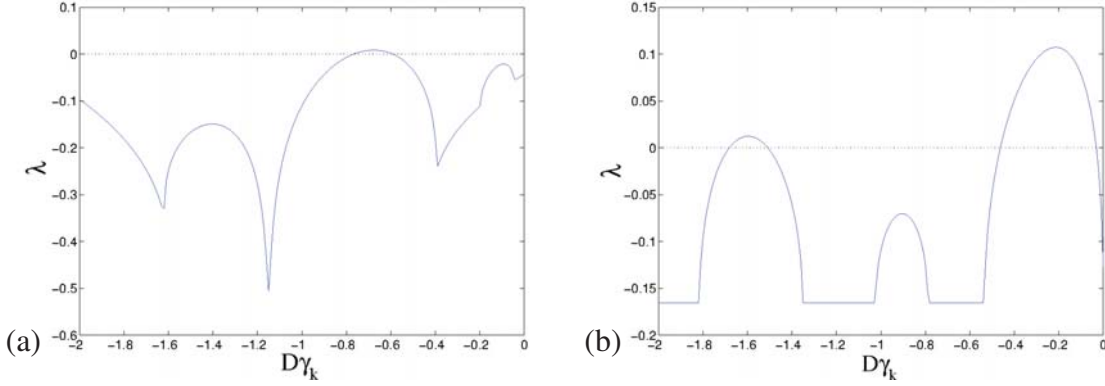


Figure 3.29: Master stability function for fully synchronized periodic states of a coupled map lattice with delay. (a) Synchronized periodic delay  $T_1 = 1$ ,  $T_2 = 2$ ,  $T_p = 2$ ,  $T_{p1} = 1$ , and  $a = 2.03$ . The periodic state has a period of 8. (b) Constant delay  $T = 1$ , and  $a = 2.18$ . The periodic state has a period of 7.

The possibility of such a fully synchronized state occurring can be determined by the master stability function. In Fig.3.29(a), the master stability function for the periodic state with  $a = 2.03$  is shown. One can see that the Lyapunov exponent is positive only in the domain  $D\gamma_k \in [-0.77, -0.6]$ . As  $\gamma_k \in [-4; 0]$ , it means that for  $D < 0.15$ , the fully synchronized periodic state can be achieved. For our example with  $D = 0.1$ , the allowed values of  $D\gamma_k$  are in  $[-0.4, 0]$ . In this region, the Lyapunov exponent has a maximum  $\lambda \approx -0.02$  at  $D\gamma_k \approx -0.1$ . This maximum is exactly the value which we have obtained directly from the structure. And with  $D\gamma_k = 0.1$  and the coupling strength  $D = 0.1$ , the critical value of  $\gamma_k$  is 1, which represents the wavenumber of the Lyapunov vector corresponding to the maximal Lyapunov exponent. In Fig.3.30, the Lyapunov vector and the related spectrum are shown. As expected, the vector has the wavenumber 1.

For comparison, consider the case with constant delays. For a delay of  $T = 1$ , a window for the periodic state with a period of 7 can be found in the bifurcation diagram for the local map (see Fig.2.8). In Fig.3.29(b), the master stability function for an example with  $a = 2.18$ . One can see that the Lyapunov exponent becomes positive for very small absolute values of  $D\gamma_k$ . This means that full synchronization can only be obtained for very weak coupling strengths for the case with a constant delay. In contrast, for the case with fluctuating delay,

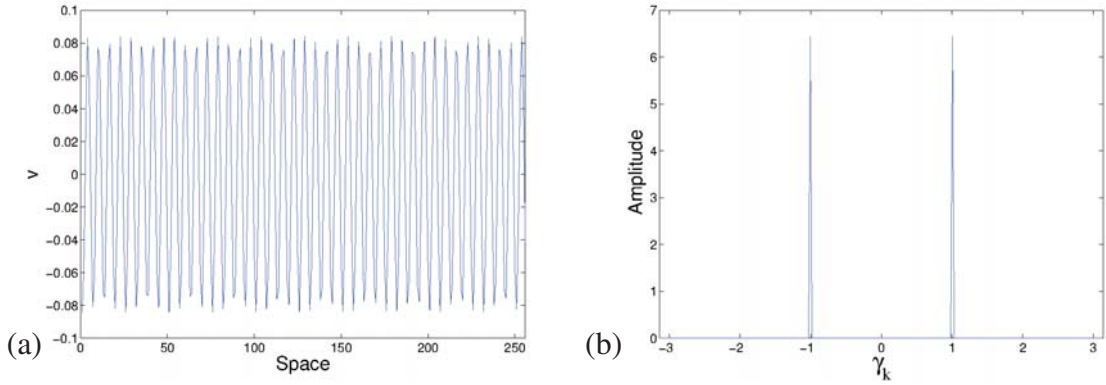


Figure 3.30: (a) Lyapunov vector corresponding to the first Lyapunov exponent for the fully synchronized periodic state in coupled map lattices with synchronized periodic delay  $T_1 = 1$ ,  $T_2 = 2$ ,  $T_p = 2$ , and  $T_{p1} = 1$ , with  $a = 2.03$ . (b) Power transformation of the vector.

the stability of the periodic orbits of the uncoupled units can be enhanced, and corresponding synchronized states appear in the coupled map lattices with coupling strengths up to a large value.

Besides the fully synchronized periodic stable state, other states can also be generated. For weaker couplings, for instance  $D = 0.01$ , a pattern with kinks can be obtained. With the coupling strength  $D = 0$ , random initial conditions lead to a structure with phase shifts. Although fully synchronized periodic states are possible for weak couplings, the basins of attraction for them are small. Thus, the phase shifts between the neighbor sites generally cannot be fully eliminated. Hence one normally obtains a structure with kinks (Fig.3.28(a)). The temporal trajectory at the boundary of domains in such a state is different from the trajectory of uncoupled units. An example is given in Fig.3.28(d) and is represented with a red line and stars. The temporal trajectory is shown for the site at  $x = 23$ , which is on the boundary of two domains. In Fig.3.32(a), a space time plot for every 32 time steps is shown. There are different domains in the structure, which is temporally periodic. For this example, the system has a maximal Lyapunov exponent  $\lambda = -0.01$ . The structure is sensitively dependent on initial conditions. This indicates the existence of a multiattractor. For  $a = 2.03$  and  $D = 0.01$ , the considered system has at least two attractors. One is the fully synchronized periodic state, the other is the kink state. For stronger couplings (for instance,  $D = 0.2$ ) the system cannot converge to stable periodic orbits, due to the strong influence from neighbors. Therefore, chaotic structures will appear (Fig.3.28(c)). An example of the

### 3.3. COUPLED MAP LATTICES WITH FLUCTUATING DELAY

temporal trajectory at one site is shown in Fig.3.28(d) with a blue line and stars. For this example, the system has a maximal Lyapunov exponent  $\lambda = 0.01$ .

When the nonlinear parameter  $a$  is increased, another pattern can be observed. For instance,

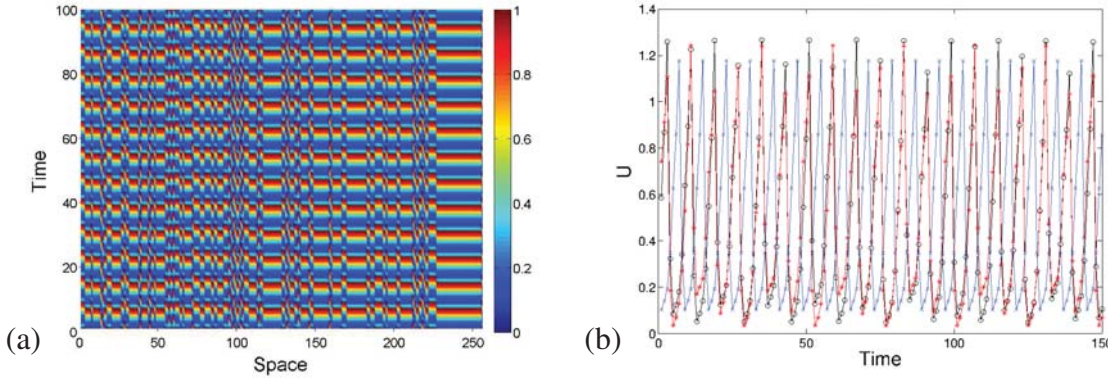


Figure 3.31: (a) Space-time plot and (b) the corresponding temporal trajectories at different sites for Eq.(3.12) with synchronized periodic delay,  $T_1 = 1$ ,  $T_2 = 2$ ,  $T_p = 2$ ,  $T_{p1} = 1$ ,  $a = 2.1$ , and  $D = 0.01$ . The patterns are generated from a random initial conditions and depicted after  $2 \cdot 10^5$  iterations. They are plotted for every time step. Periodic boundary conditions are considered. The system size is 256. The selected sites are  $x = 218$  (black),  $x = 98$  (red), and  $x = 245$  (blue).

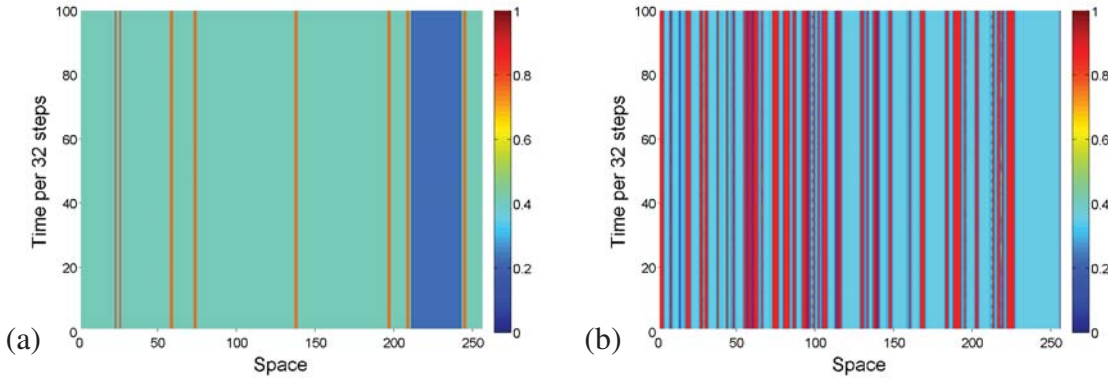


Figure 3.32: Space-time plot for Eq.(3.12) with synchronized periodic delay,  $T_1 = 1$ ,  $T_2 = 2$ ,  $T_p = 2$ ,  $T_{p1} = 1$ , and  $D = 0.01$ . The patterns are generated from random initial conditions and depicted after  $2 \cdot 10^5$  iterations. Periodic boundary condition are considered. The system size is 256. (a)  $a = 2.03$ , plotted per 32 steps. (b)  $a = 2.1$ , plotted per 32 steps.



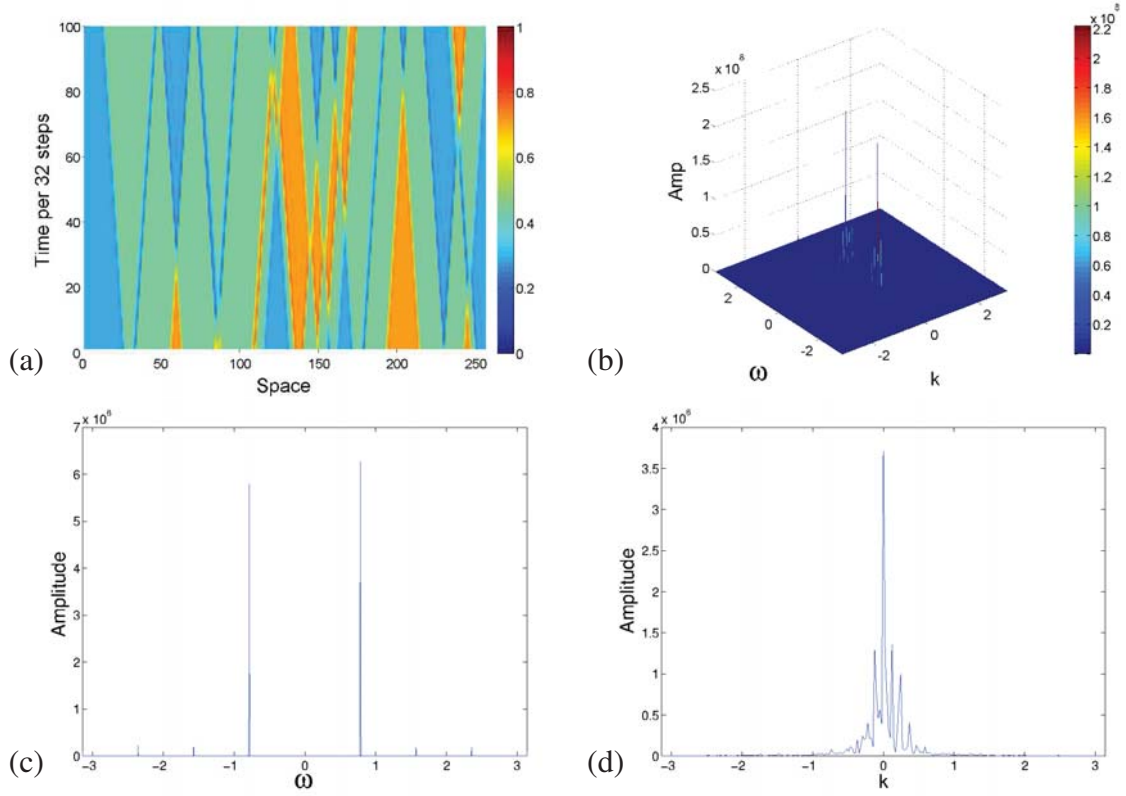


Figure 3.33: Space-time plot and the corresponding dynamic structure factor for Eq.(3.12) with synchronized periodic delay,  $T_1 = 1$ ,  $T_2 = 2$ ,  $T_p = 2$ ,  $T_{p1} = 1$ ,  $a = 2.01$ , and  $D = 0.01$ . The patterns are generated from random initial conditions and depicted after  $2 \cdot 10^5$  iterations. The patterns are plotted per 32 time step. Periodic boundary conditions are considered. The space size is chosen to be 256.

for the case with  $a = 2.1$  and  $D = 0.01$ , the structure in Fig.3.31(a) is plotted for every time step. The structure looks similar to the pattern with kinks for the case with  $a = 2.03$  and  $D = 0.01$ . But here the system has a maximal Lyapunov exponent  $\lambda = 0.04$ , which means that the system is chaotic. Note that in the study of Kaneko, as the nonlinear parameter increases, the patterns with kinks transform to frozen random patterns, which are chaotic. But unlike the normal frozen random patterns, the large domains here do not correspond to large temporal periodicity. When one looks at the structure in Fig.3.32(b), which is plotted for every 32 time steps, one finds that some temporally nonstationary structures exist in small bands, such as at sites  $x = 98$  and  $x = 218$ . The temporal trajectories are shown in Fig.3.31(b). One finds periodic behavior with a period of 8 in larger bands (blue line, selected at site  $x = 245$ ). In contrast, periodic orbits with larger periods, for example

at site  $x = 98$  with a period of 24 (red line), or irregular orbits, for example at site 218 (black line), can be found in small bands. As mentioned previously, for the considered system, patterns with kinks and rough transitions can be found for the case without any delay. The continuation of these dynamics may be the reason that such patterns for cases with fluctuating delays are found.

Additionally, the existence of traveling waves can be confirmed in this case. Traveling waves can also be obtained for weak coupling. For instance, for  $a = 2.01$  and  $D = 0.01$  it is possible to obtain a structure as the one shown in Fig.3.33(a). The pattern is plotted per 32 time steps. Unlike the traveling wave in the case with a constant delay, the structure for the case with synchronized periodic delay is complex. But the structure does not appear to be fixed spatially. The dynamic structure factor for this state is calculated and shown in Fig.3.33(b). The spectrum is not fully axially symmetric. To make the situation more obvious, the spectrum for  $k$  with  $\omega > 0$  and for  $\omega$  with  $k > 0$  are overlapped respectively and shown in Fig.3.33(c)(d). The spectra are yet not symmetric, which means the waves in the structure are not standing.

As some fascinating phenomena can be found in the above examples, it would be interesting to know if they can be obtained under other delays. Here two other cases are also investigated. In one case, the delay fluctuates slowly, which means  $T_p$  and  $T_{p1}$  are very large. In the other case, the delays themselves are large. As mentioned above, the coupled map lattices have stable states, no matter whether the states are synchronized or not, based on the stable state in the local process. Thus, the existence of stable periodic states in the uncoupled units is the precondition.

The bifurcation diagrams for some examples are shown in Fig.3.34. Because the delay increases, stable periodic states cannot be obtained directly after the  $P1 \rightarrow P2$  bifurcation. Windows for stable states, however, can be obtained afterwards. For instance, for the case with  $T_1 = 1$ ,  $T_2 = 3$ ,  $T_p = 2$ , and  $T_{p1} = 1$ , there is a window for period 12 between  $a = 1.76$  and  $1.79$ . For cases with slowly fluctuating delay, the dynamic behavior for the corresponding case with constant delays plays a more important role. The bifurcation diagram becomes more complex, but it is still possible to obtain periodic states. As periodic states can be obtained in the uncoupled units with other delays, by using the master stability function, the possibility of having a fully synchronized periodic state in the coupled map lattices can be determined. Some examples are shown in Fig.3.35. One can see that periodic states in periodic windows lose their stabilities very fast in the presence of spatial coupling. The

Lyapunov exponent can be positive even for a very small  $|D\gamma_k|$  (see Fig.3.35(a)(b)). Thus, the fully synchronized periodic state can only be found for very weak coupling.

For the periodic state, which is found directly after the bifurcation, the fully synchronized

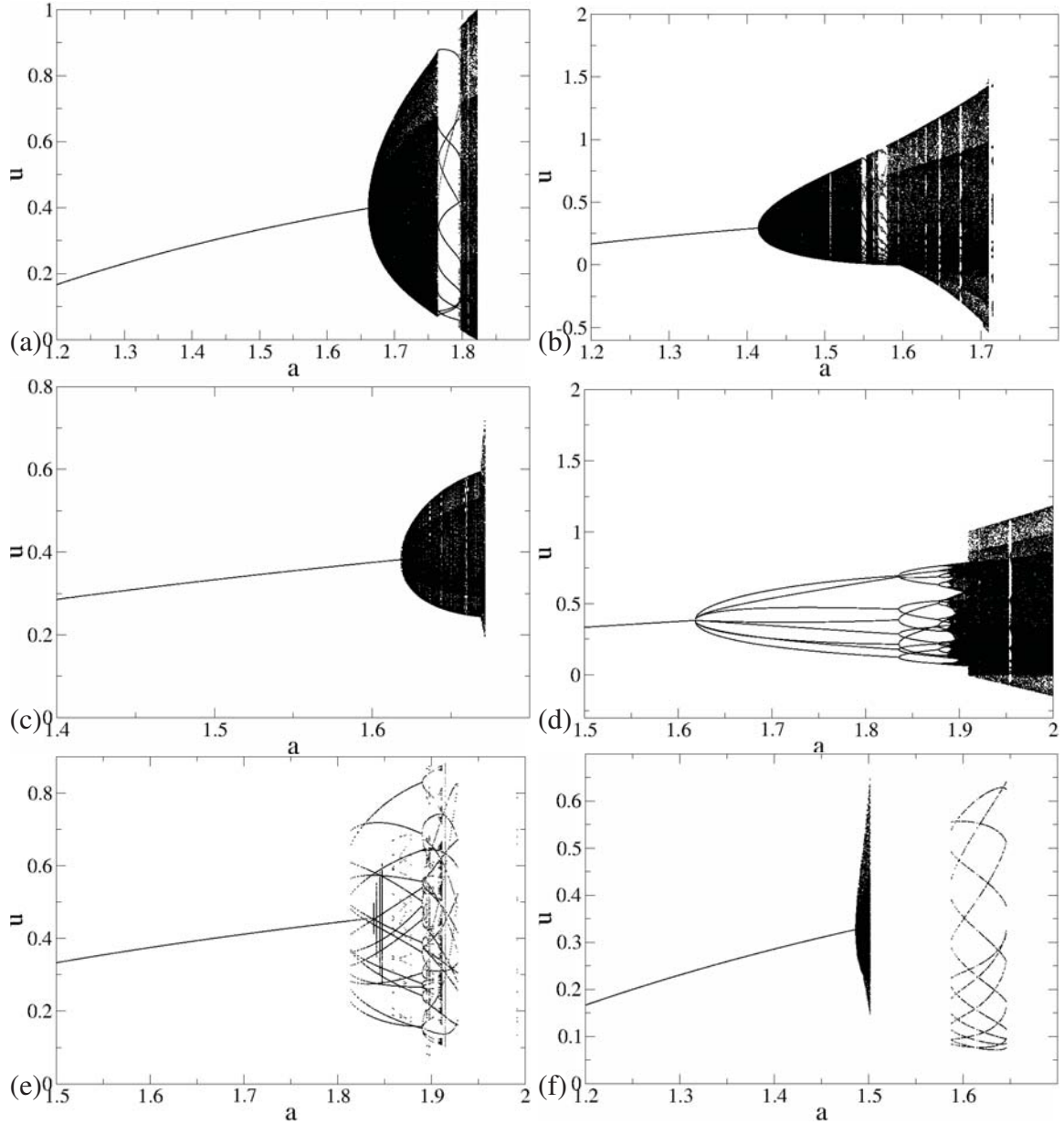


Figure 3.34: Bifurcation diagrams for a logistic map with periodic fluctuating delay. (a)  $T_1 = 1$ ,  $T_2 = 3$ ,  $T_p = 2$ , and  $T_{p1} = 1$ . (b)  $T_1 = 2$ ,  $T_2 = 5$ ,  $T_p = 2$ , and  $T_{p1} = 1$ . (c)  $T_1 = 2$ ,  $T_2 = 10$ ,  $T_p = 2$ , and  $T_{p1} = 1$ . (d)  $T_1 = 1$ ,  $T_2 = 2$ ,  $T_p = 4$ , and  $T_{p1} = 2$ . (e)  $T_1 = 1$ ,  $T_2 = 2$ ,  $T_p = 16$ , and  $T_{p1} = 8$ . (f)  $T_1 = 2$ ,  $T_2 = 5$ ,  $T_p = 16$ , and  $T_{p1} = 8$ .

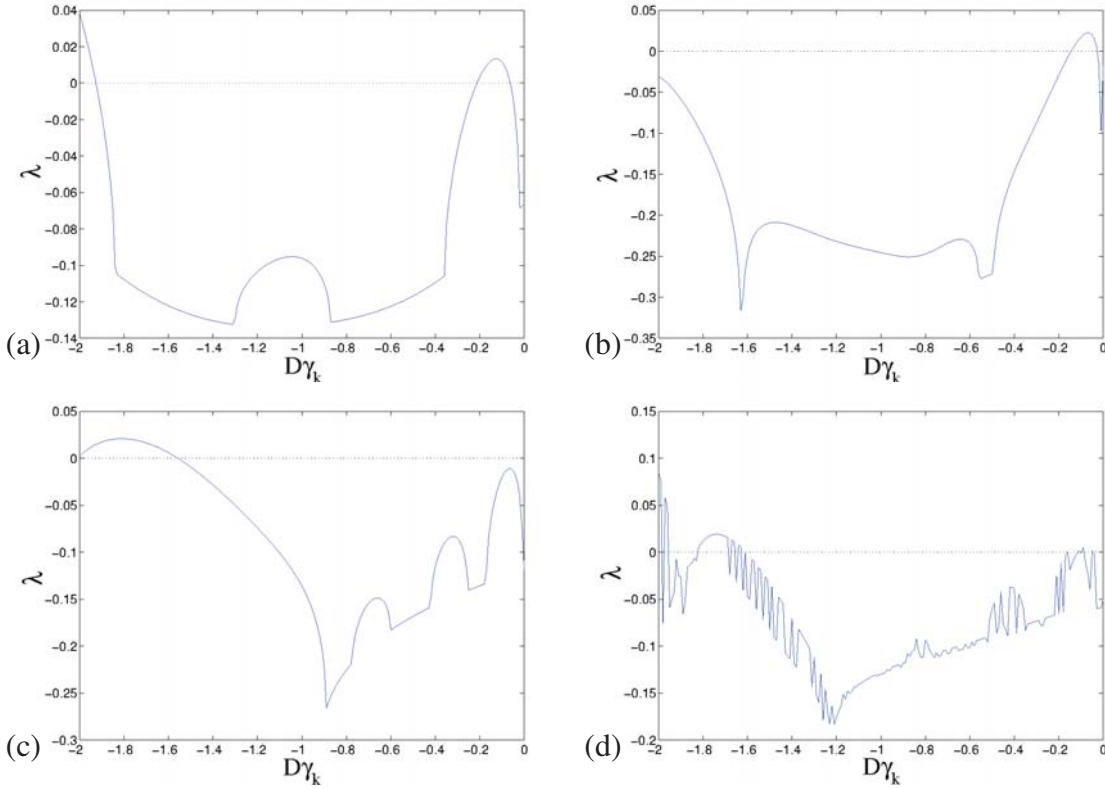


Figure 3.35: Master stability functions corresponding to the fully synchronized periodic state of the coupled map lattice with synchronized periodic delay (a)  $T_1 = 1$ ,  $T_2 = 3$ ,  $T_p = 2$ ,  $T_{p1} = 1$ , and  $a = 1.77$ , with a period of 12. (b)  $T_1 = 2$ ,  $T_2 = 5$ ,  $T_p = 2$ ,  $T_{p1} = 1$ , and  $a = 1.57$ , with a period of 22. (c)  $T_1 = 1$ ,  $T_2 = 2$ ,  $T_p = 4$ ,  $T_{p1} = 2$ , and  $a = 1.86$ , with a period of 16. (f)  $T_1 = 1$ ,  $T_2 = 2$ ,  $T_p = 16$ ,  $T_{p1} = 8$ , and  $a = 1.86$ , with a period of 16.

periodic state can be found in a large range of spatial coupling. As an example, Fig.3.35(c) shows the result of the master stability function for  $T_1 = 1$ ,  $T_2 = 2$ ,  $T_p = 4$ ,  $T_{p1} = 2$ , and  $a = 1.86$ . There is a periodic orbit with a period of 16. One can see that the Lyapunov exponent is negative for  $D\gamma_k \in [-1.56, 0]$ , which means that the fully synchronized periodic states can be observed for any spatial coupling  $D \in [0, 0.39]$ .

For cases with very slowly fluctuating delays, due to the retention of states for the corresponding cases with constant delays, cases in which there are only periodic states in periodic windows, the fully synchronized periodic state can only be found for very weak coupling. For instance, for  $T_1 = 1$ ,  $T_2 = 2$ ,  $T_p = 16$ ,  $T_{p1} = 8$ , and  $a = 1.86$ , a periodic orbit with a period of 16 can be found. As a result of the master stability function, some positive peaks

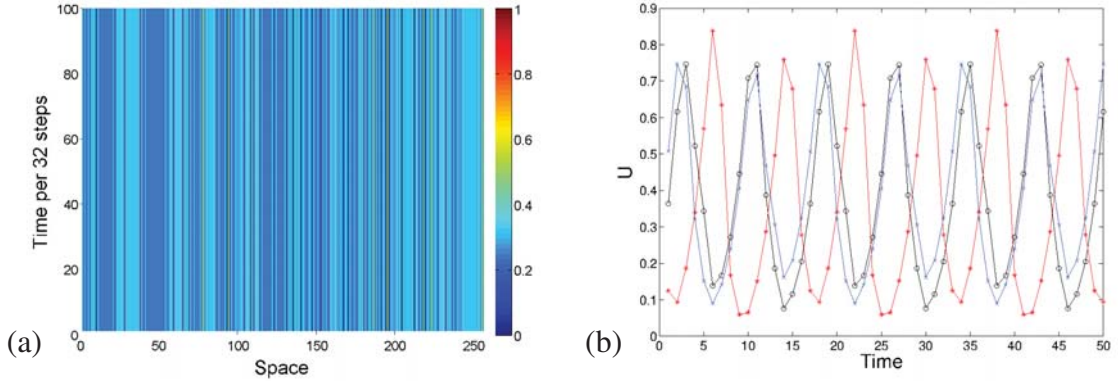


Figure 3.36: (a) Space-time plot and (b) the related temporal trajectories at different sites for Eq.(3.12) with synchronized periodic delay,  $T_1 = 1$ ,  $T_2 = 2$ ,  $T_p = 4$ ,  $T_{p1} = 2$ ,  $a = 1.86$ , and  $D = 0.05$ . The pattern is generated from random initial conditions and depicted after  $2 \cdot 10^5$  iterations. The time is plotted in 32-step intervals. Periodic boundary conditions are considered. The system size is 256.

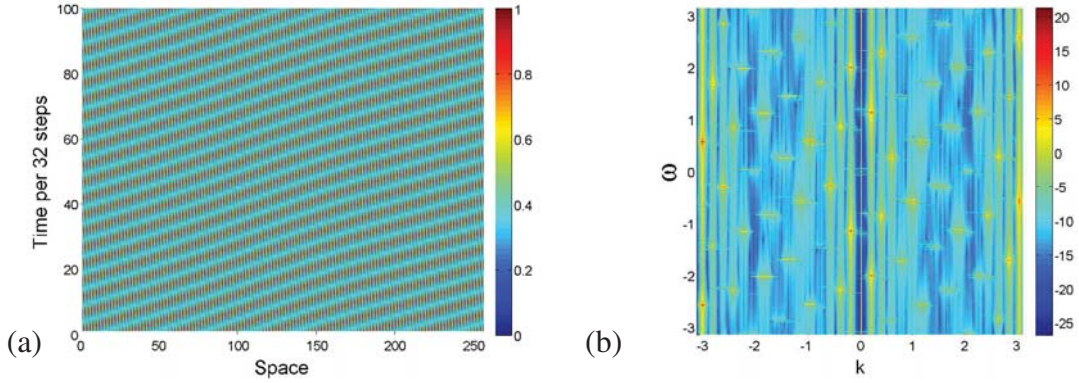


Figure 3.37: (a) Space-time plot and (b) the related dynamic structure factor for Eq.(3.12) with synchronized periodic delay,  $T_1 = 1$ ,  $T_2 = 3$ ,  $T_p = 2$ ,  $T_{p1} = 1$ ,  $a = 1.77$ , and  $D = 0.01$ . The pattern is generated from random initial conditions and depicted after  $2 \cdot 10^5$  iterations. The time is plotted in 32-step intervals. Periodic boundary conditions are considered. The system size is 256. The amplitudes of the spectrum analysis is logarithmic and is represented with different colors.

can be found for very small  $|D\gamma_k|$  (see Fig.3.35(d)).

In addition, patterns with kinks and traveling waves can also be obtained under weak coupling. For example, for the case with  $T_1 = 1$ ,  $T_2 = 2$ ,  $T_p = 4$ ,  $T_{p1} = 2$ ,  $a = 1.86$ , and  $D = 0.05$ ,

it is possible to obtain a pattern with kinks. Fig.3.36(a) shows one such structure. The system has a maximal Lyapunov exponent  $\lambda = -0.003$ . Though there are many bands with different sizes in the structure, the size of the bands is not related to the temporal period in the band. Thus, this structure is not a frozen random pattern. In Fig.3.36(b), one can see temporal trajectories at sites 2 (black), 100 (red), and 250 (blue), which are located in bands with different sizes. The trajectories are observed to have the same period of 16. For case with  $T_1 = 1$ ,  $T_2 = 3$ ,  $T_p = 2$ ,  $T_{p1} = 1$ ,  $a = 1.77$ , and  $D = 0.01$ , it is possible to obtain traveling waves. An example is shown in Fig.3.37. Some spatial transitioning is apparent in the space-time plot (Fig.3.37(a)). The corresponding dynamic structure factor (Fig.3.37(b)) confirms the result. Centrosymmetric peaks can be observed in the dynamic structure factor.

#### 3.3.2 Nonsynchronized periodic delay

Here the case with nonsynchronized periodic delay is investigated. First, the case with delay  $T_1 = 1$ ,  $T_2 = 2$ ,  $T_p = 2$ , and  $T_{p1} = 1$  is considered. In Fig.3.38, the bifurcation diagram and the corresponding Lyapunov exponent as a function of nonlinear parameter  $a$  for different coupling strengths  $D$  are shown. The space size is chosen to be 100. Periodic boundary conditions are considered. The results are obtained from random initial conditions and depicted after  $5 \cdot 10^5$  iterations. The initial delays at different sites at  $t = 0$  are also chosen randomly, with an equal probability of either 1 or 2 being chosen. The difference between the case with synchronized periodic delay and the case with nonsynchronized periodic delay can be clearly observed. The bifurcation point is no longer fixed for different coupling strengths. Fig.3.38(d) shows that for different coupling strengths  $D$ , the zero positions for Lyapunov exponent are located at different values of the nonlinear parameter  $a$ . Due to different delays at different sites, a fully synchronized stable periodic state is no longer possible. And the master stability function cannot be applied in this case. For weak couplings, patterns with kinks can still be obtained, such as for the case with  $a = 2.06$  and  $D = 0.01$ . An example space-time plot is shown in Fig.3.39. The pattern is generated from random initial conditions and depicted after  $2 \cdot 10^5$  iterations. The pattern is plotted per 32 time steps. Periodic boundary conditions are considered. The space size is chosen to be 256. For this state, the system has a Lyapunov exponent  $\lambda = -0.06$ . The temporal trajectories at sites 50 (black), 180 (red), and 240 (blue) are shown in Fig.3.39(b). One can see that all of these trajectories have a period of 8, even if they are in bands with different sizes.



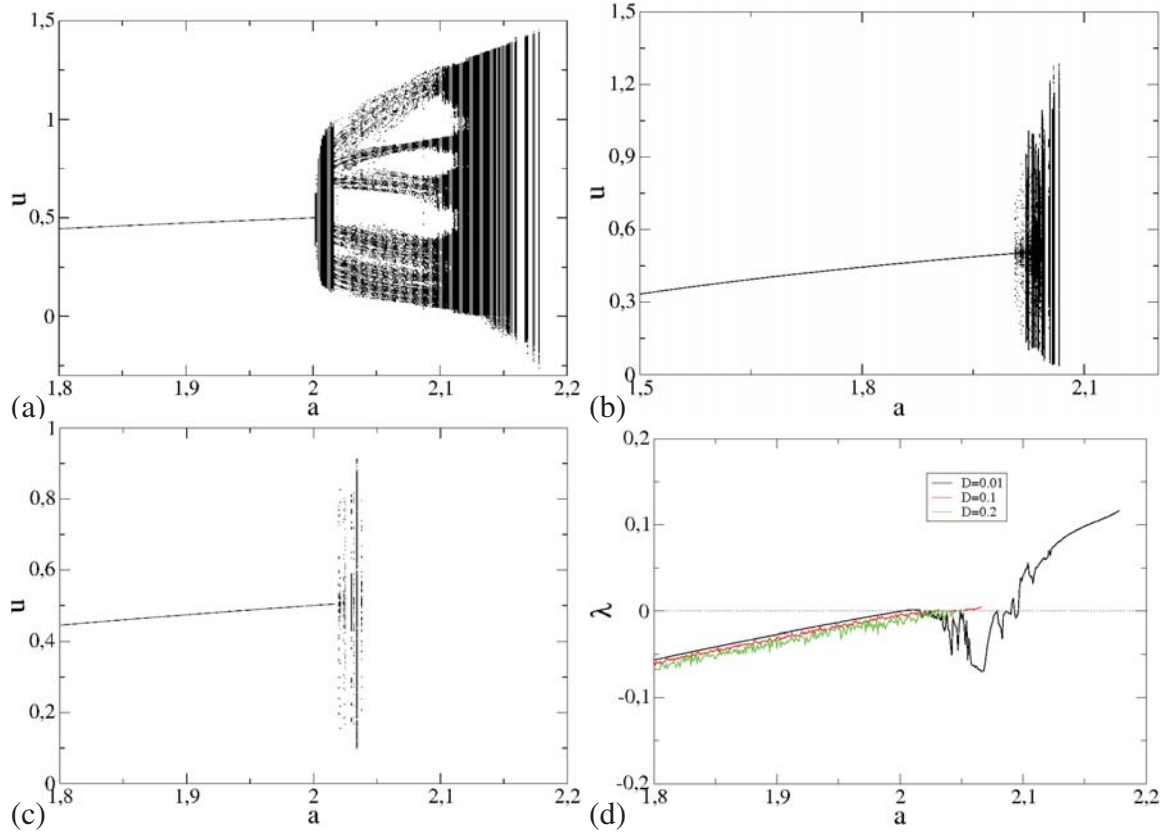


Figure 3.38: Bifurcation diagrams and the maximal Lyapunov exponents for coupled map lattices with non-synchronized periodic delays  $T_1 = 1$ ,  $T_2 = 2$ ,  $T_p = 2$ , and  $T_{p1} = 1$ . The results are obtained from random initial conditions and depicted after  $5 \cdot 10^5$  iterations. Periodic boundary conditions are considered. The space size is chosen to be 100. (a)  $D = 0.01$ , (b)  $D = 0.1$ , (c)  $D = 0.2$ . (d) Black:  $D = 0.01$ , red:  $D = 0.1$ , and green:  $D = 0.2$ .

In addition, the nonsynchronized periodic cases with other delay variations are studied. In Fig.3.40, one can see the dependence of the Lyapunov exponent on the nonlinear parameter  $a$  under different couplings for two other examples. Similar phenomena as those in Fig.3.38 can be observed. The bifurcation point is not the same for different coupling strengths. Because delay can induce spatial transitions, for large delay, stable traveling waves (the maximal Lyapunov exponent  $\lambda = 0$ ) can be observed instead of nonsynchronized periodic states. For instance, for  $T_1 = 2$ ,  $T_2 = 5$ ,  $T_p = 2$ ,  $T_{p1} = 1$ ,  $a = 1.5$ , and  $D = 0.01$  the structure in Fig.3.41(a) can be obtained. The system has a maximal Lyapunov exponent  $\lambda = 0$ . The corresponding dynamic structure factor is shown in Fig.3.41(b). The amplitude of the spectrum analysis is shown on a logarithmic scale represented with different colors. Here

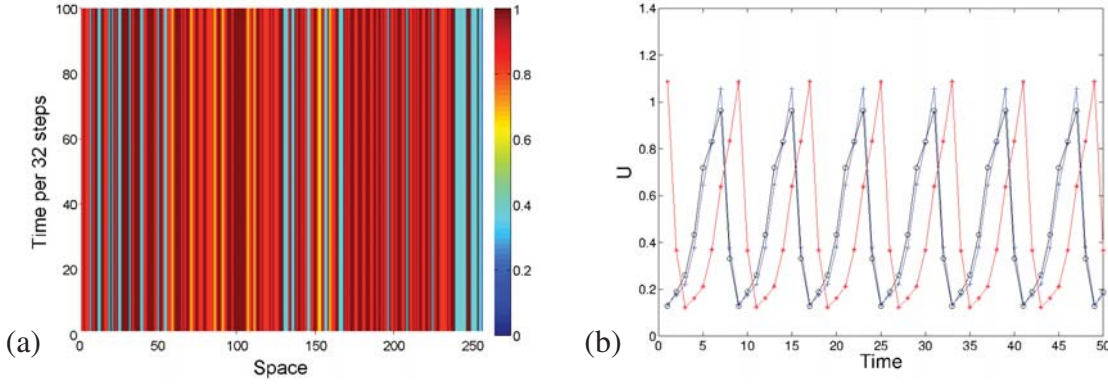


Figure 3.39: (a) Space-time plot and (b) the related temporal trajectories at different sites for Eq.(3.12) with nonsynchronized periodic delay,  $T_1 = 1$ ,  $T_2 = 2$ ,  $T_p = 2$ ,  $T_{p1} = 1$ ,  $a = 2.06$ , and  $D = 0.01$ . The pattern is generated from random initial conditions and depicted after  $2 \cdot 10^5$  iterations. The time is plotted in 32-step intervals. Periodic boundary conditions are considered. The space size is chosen to be 256.

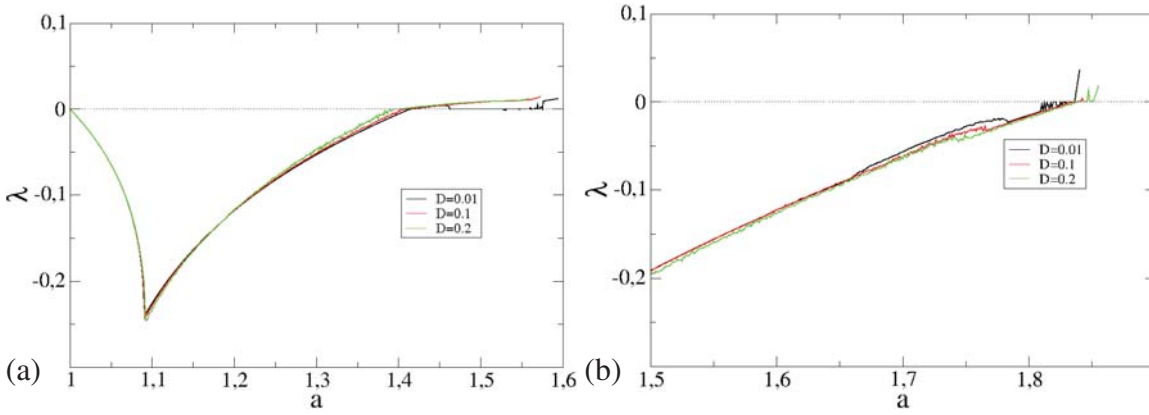


Figure 3.40: Maximal Lyapunov exponent as a function of the nonlinear parameter  $a$  for a coupled map lattice with nonsynchronized periodic delay. (a)  $T_1 = 2$ ,  $T_2 = 5$ ,  $T_p = 2$ , and  $T_{p1} = 1$ , black:  $D = 0.01$ , red:  $D = 0.1$ , green:  $D = 0.2$ . (b)  $T_1 = 1$ ,  $T_2 = 2$ ,  $T_p = 8$ , and  $T_{p1} = 4$ , black:  $D = 0.01$ , red:  $D = 0.1$ , green:  $D = 0.2$ .

some centrosymmetric peaks can clearly be observed, which proves the existence of traveling waves. For cases with slowly fluctuating delays, due to the complexity of the bifurcation, sequence patterns with kinks can hardly be found. Instead, quasi-periodic states appear. For instance, for  $T_1 = 1$ ,  $T_2 = 2$ ,  $T_p = 8$ ,  $T_{p1} = 4$ , and  $D = 0.01$ , after the bifurcation, there are some regions where the maximal Lyapunov exponent is nearly zero. An example is shown



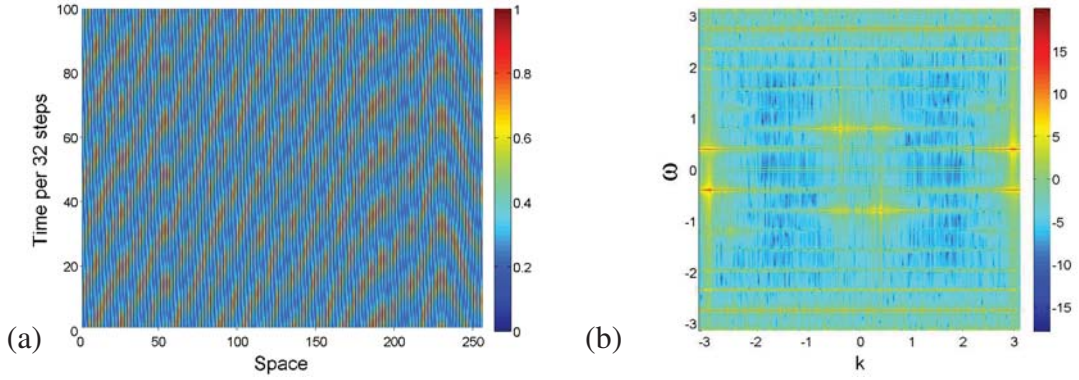


Figure 3.41: (a) Space-time plot and (b) the related dynamic structure factor for Eq.(3.12) with nonsynchronized periodic delay,  $T_1 = 2$ ,  $T_2 = 5$ ,  $T_p = 2$ ,  $T_{p1} = 1$ ,  $a = 1.5$ , and  $D = 0.01$ . The pattern is generated from random initial conditions and depicted after  $2 \cdot 10^5$  iterations. The time is plotted in 32-step intervals. Periodic boundary conditions are considered. The space size is chosen to be 256. The amplitudes of the spectrum analysis is shown on a logarithmic scale represented with different colors.

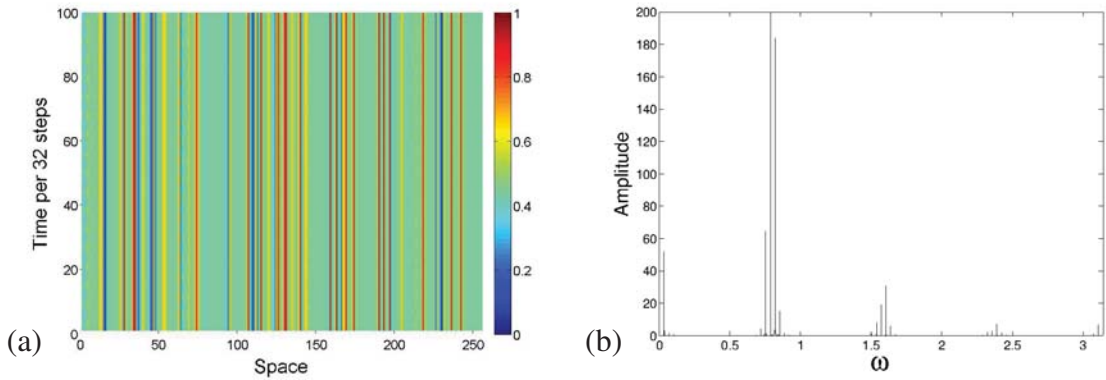


Figure 3.42: (a) Space-time plot for Eq.(3.12) with nonsynchronized periodic delay,  $T_1 = 1$ ,  $T_2 = 2$ ,  $T_p = 8$ ,  $T_{p1} = 4$ ,  $a = 1.82$ , and  $D = 0.01$ . The pattern is generated from random initial conditions and depicted after  $2 \cdot 10^5$  iterations. The time is plotted in 32-step intervals. Periodic boundary conditions are considered. The space size is chosen to be 256. (b) Spectrum analysis for the temporal trajectory of the state (a) at site  $x = 5$ . A Hamming window is used to reduce spectral leakage.

### 3.3. COUPLED MAP LATTICES WITH FLUCTUATING DELAY

---

in Fig.3.42. One can see that in the space-time plot in Fig.3.42(a), which is plotted per 32 time steps, the bands are located at fixed positions, which means there are no traveling waves in the structure. But one can notice that some bands are not temporally stationary in this structure, for instance, at site  $x = 5$ . Thus, the spectrum analysis for the temporal trajectory at site  $x = 5$  is calculated and shown in Fig.3.42(b). The length of the sample is  $2 \cdot 10^5$ . A Hamming window is applied to reduce spectral leakage. Here one can observe several fundamental frequencies, indicating that the temporal trajectory is quasi-periodic. And the system has a maximal Lyapunov exponent  $\lambda = 0$ .

## 4 Partial Differential Equations

The second part of this study investigates the space-time continuous system. A Fisher-KPP-type reaction-diffusion equation with delay is considered in this part of study.

### 4.1 Necessary conditions for Turing instability

The focus of this part of the study is the existence of a Turing bifurcation. In Chapter 2, the cause of Turing instability was already discussed. The classic Turing instability is introduced in two-component reaction-diffusion systems and is found only in multiple-component reaction-diffusion systems. Since the considered system is a one-component reaction-diffusion system with delay, it is helpful to connect our considered system to a multiple-component reaction-diffusion system. For the occurrence of Turing instability, the following two conditions are necessary:

- There are *activators* and *inhibitors* in the system.
- The propagation of *inhibitor* is faster than *activator* ( $D_V > D_U$  in Eq.(2.25) in Chapter. 2).

So in the considered system (1.4), the reaction term is based on the Hutchinson's equation. Since the delay term is considered as another variable  $v(x, t) = u(x, t - \tau)$ , the system in Eq.(1.4) can be rewritten as

$$\frac{\partial u(x, t)}{\partial t} = au(x, t)(1 - v(x, t)) + D\Delta u(x, t) \quad (4.1)$$

$$v(x, t) = u(x, t - \tau). \quad (4.2)$$

The larger  $u(x, t)$  is, the larger  $\frac{\partial u(x, t)}{\partial t}$  is. And the larger  $v(x, t)$  is, the less  $\frac{u(x, t)}{\partial t}$  is. Thus,  $u(x, t)$  can be considered as an *activator*, and the delay variable  $v(x, t) = u(x, t - \tau)$  can be considered as an *inhibitor*.

For the propagation, two possibilities can be considered. One is that the velocity depends on the time and position. For this case, it is always possible to find some states where the velocity of  $u(t - \tau)$  is larger than that of  $u(t)$ . Therefore, the second necessary condition is fulfilled in this case. The other possibility is to treat the velocity as constant, which is common in the study of front propagation problems in reaction-diffusion systems. Through the efforts of many scientists, the asymptotic constant propagation velocity in reaction-diffusion system is now well understood [9, 56, 57]. Assuming that  $u$  has a constant propagation velocity  $v_u$ , and  $x_0$  is the location of  $u$  at  $t = 0$ , then at time  $t$ ,  $u$  is located at  $x_0 + v_u t$ , and  $v$  is located at  $x_0 + v_u \cdot (t - \tau)$ . When the delay  $\tau$  is constant,  $v(t)$  also propagates with the same velocity  $v_u$ . But when the delay  $\tau$  temporally fluctuates, the average propagation velocity of  $v(t)$  between times  $t_1$  and  $t_2$  can be described as

$$v_v = \frac{x_0 + v_u \cdot (t_2 - \tau(t_2)) - (x_0 + v_u \cdot (t_1 - \tau(t_1)))}{t_2 - t_1} = v_u \left(1 + \frac{\tau(t_1) - \tau(t_2)}{t_2 - t_1}\right). \quad (4.3)$$

Here the velocity  $v_v$  is larger than  $v_u$  if  $\tau(t_1)$  is larger than  $\tau(t_2)$ . Thus, although the propagation of the *inhibitor* is not always faster than the *activator*, it can be intermittently faster in the case with fluctuating delays. Therefore, the considered system satisfies the necessary conditions of Turing instability.

## 4.2 Influence of fluctuating delay in ODE's

In Chapter 2, the dynamics of the Hutchinson's equation are discussed, but to the best of my knowledge, the influence of fluctuating delay on this system is still unknown. So before the study of the reaction-diffusion system with delay, the dynamics of the Hutchinson's equation with fluctuating time delay are investigated and discussed in this section. The Hutchinson's equation with delay reads:

$$\dot{u}(t) = au(t)(1 - u(t - \tau(t))) \quad (4.4)$$

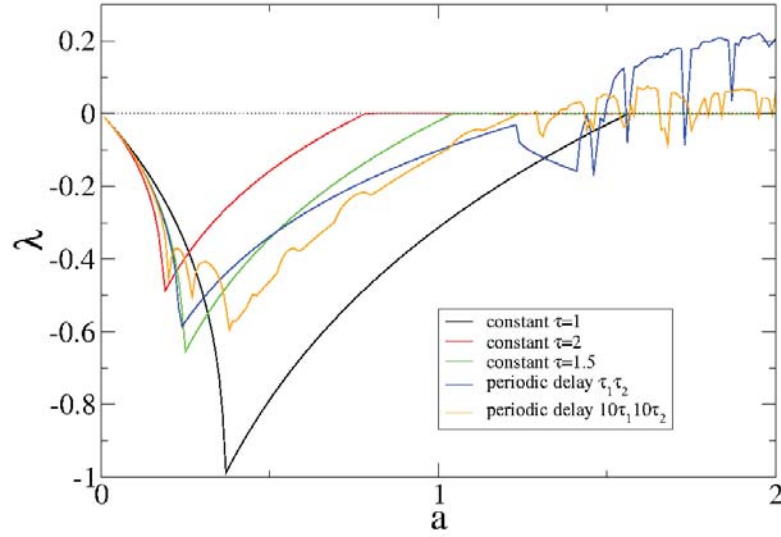


Figure 4.1: The dependence of maximal Lyapunov exponent on the parameter  $a$  for Eq.(4.4) with a step-shaped time-varying delay.

As discussed in the background chapter, the Hutchinson equation has only two states. The first is the stable fixed point  $x^* = 1$  with a maximal Lyapunov exponent  $\lambda < 0$  for  $a\tau < \frac{\pi}{2}$ . The other is a stable periodic orbit with a maximal Lyapunov exponent  $\lambda = 0$ . But when the delay fluctuates in time, more states can be generated. In this study, two different types of fluctuating delays are considered. One is according to the unit step function; more precisely, the variation of the delay can be generally described as

$$\tau(t) = \begin{cases} \tau_1 & \text{if } t \bmod T_p < T_1 \\ \tau_2 & \text{otherwise.} \end{cases} \quad (4.5)$$

The other is a sine-shaped delay, which can be described as

$$\tau(t) = \tau_M + \tau_A \sin(\omega t), \quad (4.6)$$

where  $\tau_M$  is the mean value of the delay,  $\tau_A$  is the amplitude of the delay variation, and  $\omega$  is the frequency of the variation.

Fig. 4.1 shows the Lyapunov exponents for the case with a step-shaped delay. Here the delay times are  $\tau_1 = 1$  and  $\tau_2 = 2$ , and two different cases of fluctuation are selected. One is a fast fluctuation (blue line), where  $T_p = 2$  and  $T_1 = 1$ , and the other is a slow fluctuation (orange

## 4.2. INFLUENCE OF FLUCTUATING DELAY IN ODE'S

line), where  $T_p = 20$  and  $T_1 = 10$ . For comparison, the Lyapunov exponents for cases with constant delays  $\tau = 1$  (black line),  $\tau = 2$  (red line), and  $\tau = 1.5$  (green line) are also represented in the figure. Although the average value of delay is 1.5, the bifurcation points for the cases with fluctuating delay are not the same as for the case with a constant delay  $\tau = 1.5$ . Furthermore, after the  $P1 \rightarrow P2$  bifurcation, the system dynamics are rather complex for the cases with periodic fluctuating delays. Only for the cases with slow fluctuating delays can zero Lyapunov exponents be found in a small region after the first bifurcation. Moreover, the Lyapunov exponent for the case with a step-shaped periodically fluctuating delay can be either positive, which corresponds to chaotic behaviors, or negative, which corresponds to a stable state.

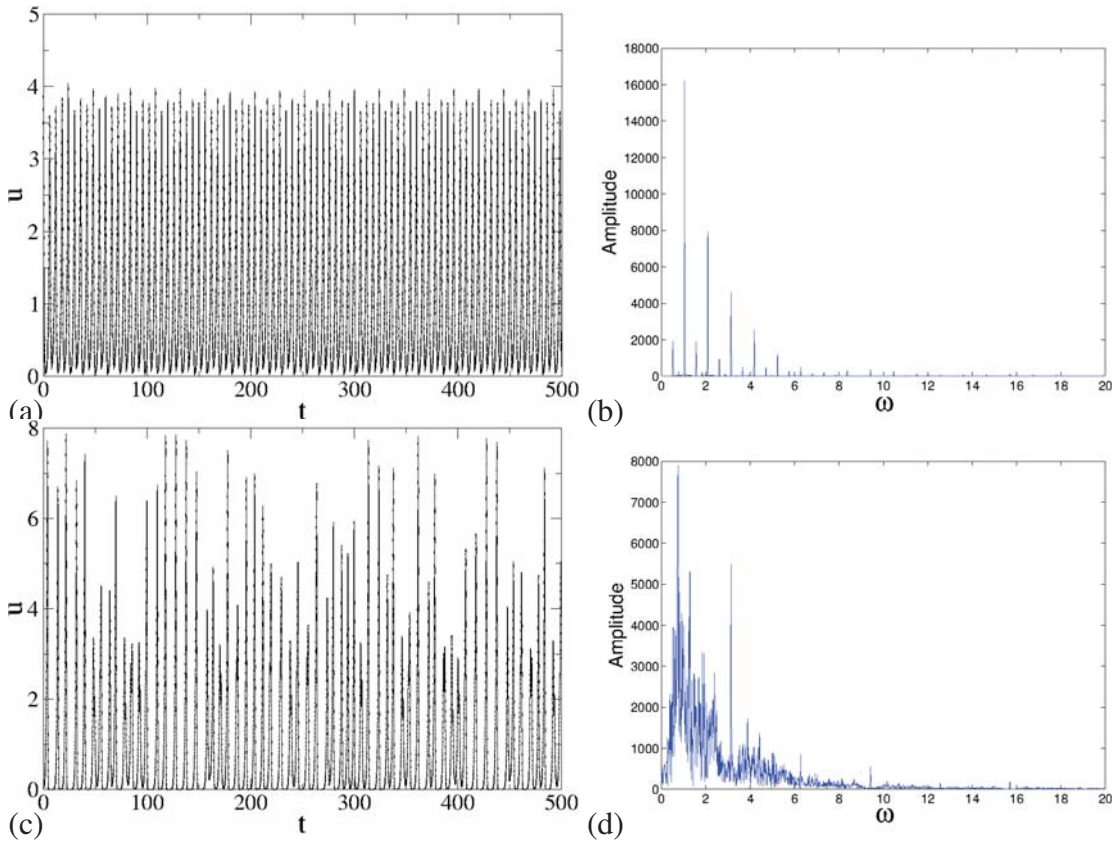


Figure 4.2: Trajectories of examples for Eq.(4.4) with a step-shaped fluctuating delay ( $\tau_1 = 1$ ,  $\tau_2 = 2$ ,  $T_p = 2$ , and  $T_1 = 1$ ), and the corresponding power spectra. (a)(b):  $a = 1.485$ , (c)(d):  $a = 1.8$ .

In Fig.4.2, two examples for the trajectories in cases with step-shaped fluctuating delay ( $\tau_1 = 1$ ,  $\tau_2 = 2$ ,  $T_p = 2$  and  $T_1 = 1$ ) are shown. One is for the case  $a = 1.485$ , where the Lyapunov exponent  $\lambda \approx -0.03$ . One can observe a periodic orbit. The other is for

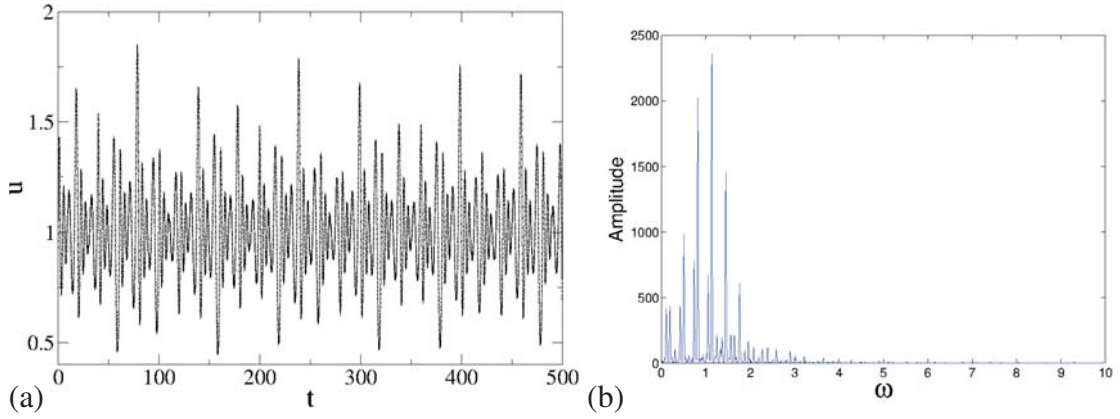


Figure 4.3: Trajectory of an example for Eq.(4.4) with a step-shaped fluctuating delay ( $\tau_1 = 1$ ,  $\tau_2 = 2$ ,  $T_p = 20$ , and  $T_1 = 10$ ) and the corresponding power spectrum.  $a = 1.25$ .

the case  $a = 1.8$ , where the Lyapunov exponent  $\lambda \approx 0.20$ . Here the represented orbit is chaotic. Additionally, in Fig.4.3, an example for the quasiperiodic orbit is shown, which can be found in the case with a slow fluctuating delay ( $\tau_1 = 1$ ,  $\tau_2 = 2$ ,  $T_p = 20$ , and  $T_1 = 10$ ). Here the nonlinear parameter  $a = 1.25$  and the maximal Lyapunov exponent  $\lambda \approx 0$ . The trajectories are obtained from random initial conditions and depicted after  $2 \cdot 10^5$  time units. To confirm the periodicity of the trajectories, the corresponding power spectra are also calculated. The sample is selected with a size of 500 time units. The Hamming window is applied in the analysis. One can see that in the case with fast fluctuating delays for  $a = 1.485$ , the fundamental frequency for the periodic orbit can be clearly identified in the power spectrum. And for  $a = 1.8$ , the trajectory looks irregular and the spectrum is rough, indicating that it is a chaotic state. In the case with a slow fluctuating delay for  $a = 1.25$ , a spectrum with three fundamental frequencies are obtained, which are related to a quasiperiodic orbit.

For the case with a sine-shaped fluctuating delay, similar results are obtained. Fig.4.4 shows the Lyapunov diagram for the cases with a sine-shaped delay with  $\tau_M = 1.5$ ,  $\tau_A = 0.5$ , and  $\omega = \pi$  (fast fluctuating) or  $\omega = \frac{1}{\pi}$  (slow fluctuating). One can see that the first bifurcation point for the case with a fluctuating delay is shifted away from the bifurcation point for the case with a constant delay  $\tau = 1.5$ , which is the average value of the fluctuating delays. The dynamic behavior is also complex after the first bifurcation. Both stable states and chaotic states can be seen. The quasi-periodic state can only be found in cases with a slow fluctuating delay.



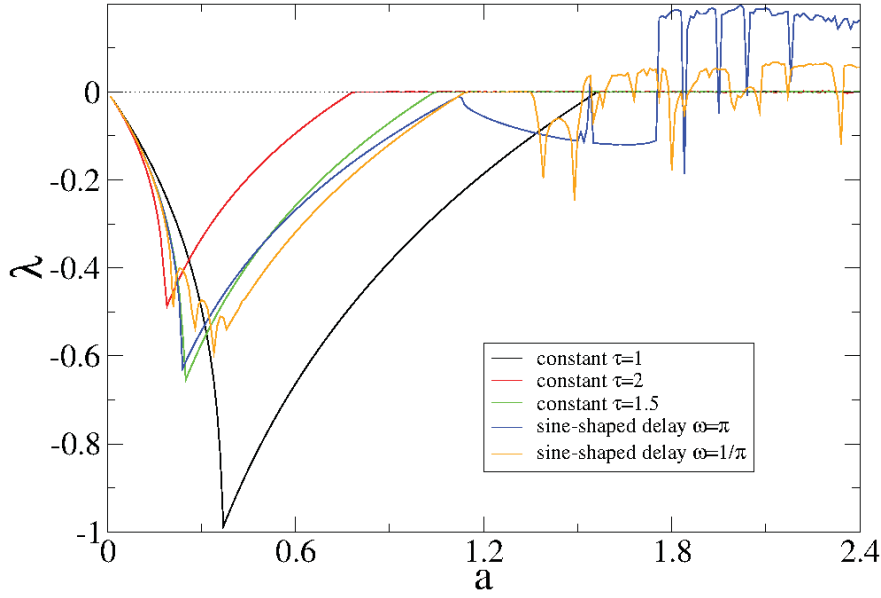


Figure 4.4: The dependence of maximal Lyapunov exponent on the parameter  $a$  for Eq.(4.4) with a sine-shaped delay.

As in the case with a step-shaped delay, examples for different types of trajectories and the corresponding power spectra in cases with a sine-shaped fluctuating delay  $\tau_M = 1.5$ ,  $\tau_A = 0.5$ , and  $\omega = \frac{1}{\pi}$  are shown in Fig.4.5. After the  $P1 \rightarrow P2$  bifurcation, in cases with a slow fluctuating delay one can obtain a small region where quasiperiodic orbit can be found. For instance, three fundamental frequencies can be found in the power spectrum for  $a = 1.3$ . The Lyapunov exponent is  $\lambda \approx 0$ . When  $a$  further increases, the state can be stable or chaotic. For instance, a periodic orbit is obtained for  $a = 1.45$ . In the related spectrum, the fundamental frequency can be seen. And for  $a = 1.6$ , a chaotic orbit is observed.

For Hutchinson's equation with fluctuating delay, the stable states after the bifurcation are no longer fixed points but periodic orbits. Generally, in autonomous systems, the periodic orbits have a maximal Lyapunov exponent of 0. Here due to the time fluctuation of the delay, the system changes from autonomous to nonautonomous. Thus, the periodic orbits have a negative maximal Lyapunov exponent.



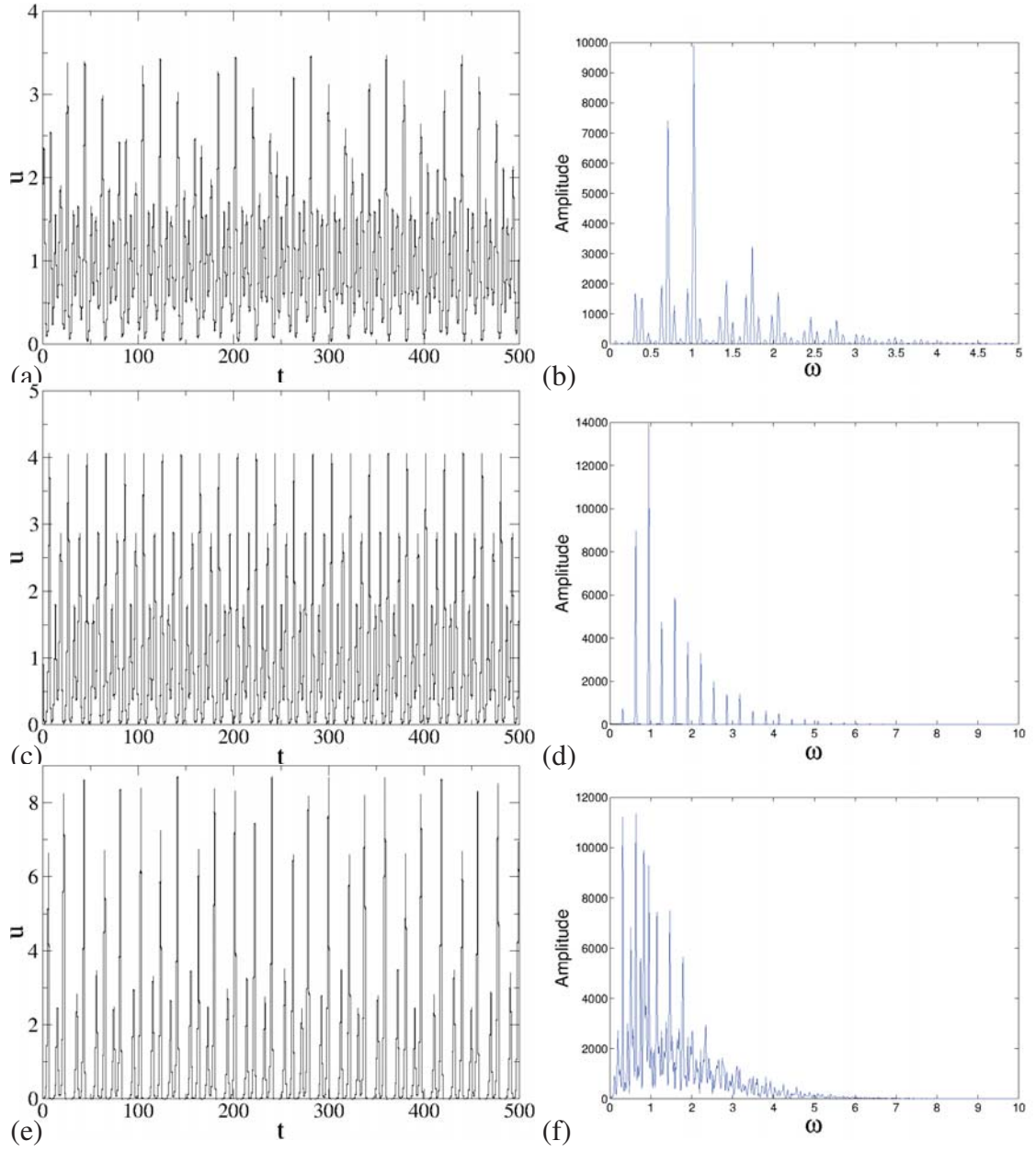


Figure 4.5: Trajectories of examples for Eq.(4.4) with a sine-shaped fluctuating delay ( $\tau_M = 1.5$ ,  $\tau_A = 0.5$ , and  $\omega = \frac{1}{\pi}$ ) and the corresponding power spectra. (a)(b):  $a = 1.3$ , (c)(d):  $a = 1.45$ , (e)(f)  $a = 1.6$ .

### 4.3 Linear stability analysis for PDE's

In order to determine the occurrence of the Turing instability, linear stability analysis is necessary. In this section, several forms of linear stability analysis are studied. Both of the

general form, which can be used to characterize the stability of certain solutions for a one-component reaction-diffusion system with delay, and the form for the Fisher-KPP equation with delay are investigated.

#### 4.3.1 General form and linear stability analysis for stable equilibria

The one-component reaction-diffusion equation with delay is considered:

$$\frac{\partial u(x,t)}{\partial t} = f(u(x,t), u(x, t - \tau(t))) + D\Delta u(x,t), \quad (4.7)$$

where  $t$  and  $x$  are the time and space variables, respectively. The linearized equation for this system is

$$\frac{\partial \delta u(x,t)}{\partial t} = \frac{\partial f}{\partial u(x,t)} \delta u(x,t) + \frac{\partial f}{\partial u(x, t - \tau(t))} \delta u(x, t - \tau(t)) + D\Delta \delta u(x,t). \quad (4.8)$$

According to the discussion in Section 2.3, the perturbation  $\delta u(x,t)$  can be assumed to have the form

$$\delta u(x,t) = \delta u_0 e^{st+ikx}. \quad (4.9)$$

Plugging this into Eq.(4.8) leads to the equation

$$s = \frac{\partial f}{\partial u(t)} + \frac{\partial f}{\partial u(t - \tau)} e^{-s\tau} - Dk^2. \quad (4.10)$$

This equation is an extension of the characteristic equation for delay differential equations [39], which can be numerically solved to obtain the Lyapunov spectrum. Formally, the maximal stability exponent can also be calculated from Eq.(4.10) and reads as

$$s = \frac{f_t \tau - Dk^2 \tau + W(f_t \tau e^{(Dk^2 - f_t)\tau})}{\tau}, \quad (4.11)$$

where  $f_t = \frac{\partial f}{\partial u(t)}$ ,  $f_\tau = \frac{\partial f}{\partial u(t-\tau)}$ , and  $W(\dots)$  is the Lambert W function. For a fixed point  $u^*$ ,

$f_l$  and  $f_\tau$  are constant. Assuming a new control parameter  $K = Dk^2 - f_l$ , which characterizes the spatial perturbation, Eq.(4.10) can be written as

$$s = f_\tau e^{-s\tau} - K, \quad (4.12)$$

and Eq.(4.11) can be simplified as

$$s = -K + \frac{W(f_\tau \tau e^{K\tau})}{\tau}. \quad (4.13)$$

Since the formula for stability exponent (Eq.(4.13)) contains a Lambert-W function, which is not an elementary function and is therefore complex to investigate, other analytical methods are considered here. With a complex notation of stability exponent  $s = l + i\omega$ , the characteristic equation for the stable fixed point Eq.(4.12) in a general one-component reaction-diffusion equation can be rewritten as

$$l + i\omega + K = f_\tau e^{-l\tau} (\cos \omega\tau - i \sin \omega\tau). \quad (4.14)$$

Equating the real part and imaginary part on both sides yields

$$l + K = f_\tau e^{-l\tau} \cos \omega\tau, \text{ and} \quad (4.15)$$

$$\omega = -f_\tau e^{-l\tau} \sin \omega\tau. \quad (4.16)$$

From the second equation (4.16) one can obtain

$$e^{-l\tau} = -\frac{1}{\tau} \frac{\phi}{f_\tau \sin \phi}, \quad (4.17)$$

with  $\phi = \omega\tau$ . The left-hand side of this equation is always positive, limiting the domain of  $\phi$  to  $[2k\pi, 2k\pi + \pi]$  or  $[-2k\pi, -2k\pi - \pi]$  with  $k = 0, 1, 2, 3, \dots$ . Furthermore, from Eqs.(4.15) and (4.16),  $l$  and  $K$  as functions of  $\phi$  can be separately derived:

$$\begin{aligned} l &= \frac{1}{\tau} (\ln \tau + \ln \frac{-f_\tau \sin \phi}{\phi}), \text{ and} \\ K &= \frac{1}{\tau} (\ln \frac{\phi}{-f_\tau \sin \phi} - \ln \tau - \phi \cot \phi). \end{aligned} \quad (4.18)$$

As the parameter  $f_\tau$  and the delay  $\tau$  do not include in trigonometric functions, they cannot influence the monotonicity and domain of the functions. Hence, one can understand the

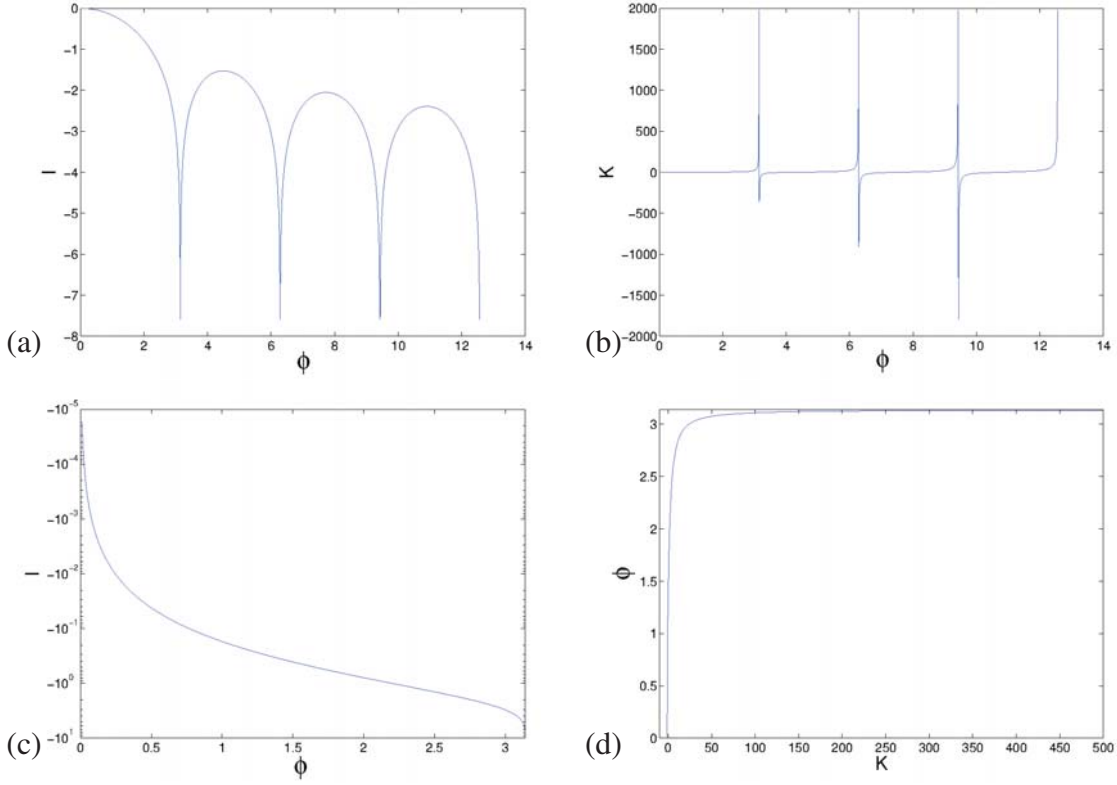


Figure 4.6: Diagram of the relationship between (a)(c)  $l$  and  $\phi$  and between (b)(d)  $K$  and  $\phi$  with  $f_\tau = -1$  and  $\tau = 1$ . (c) is the enlarged diagram of (a) in the interval  $\phi \in [0, \pi]$  with a logarithmic axis of  $l$ , and (d) is the enlarged diagram of (b) in the interval  $\phi \in [0, \pi]$  with an inverse axis.

behavior of Eq.(4.18) from an example. Diagrams of an example for these relationships are shown in Fig.4.6. The parameter  $f_\tau$  is chosen to be  $-1$ , and the delay  $\tau$  is 1. Notice that the delay variable is an *inhibitor*, so  $f_\tau$  should be negative. One can find that  $l$  and  $K$  vary smoothly in the intervals  $\phi \in [2k\pi, 2k\pi + \pi]$ . In the first domain  $[0, \pi]$  of  $\phi$ , which is generally related to the maximal stability exponent,  $l$  monotonically decreases and  $K$  monotonically increases. A director diagram for the relationship between  $K$  and  $\phi$  is shown in Fig.4.6(d). Thus Fig.4.6(c) and (d) indicate that as  $K$  increases,  $\phi$  also increases, which leads  $l$  to decrease. The monotonic decrease of  $l$  with the increase of  $K$  means that the maximum of  $l$  is at  $K = 0$ . Therefore, there is no possibility of Turing instability for the fixed point of a one-component reaction-diffusion system with a constant delay.

For the fluctuating delays, there are two limiting cases. One is the case with very slowly fluctuating delays, because the time is enough for the system to relax according to a partic-

ular temporal evolution, the Lyapunov exponent for the system can be simply calculated as a weighted mean of the Lyapunov exponent for all the involved temporal states [21, 22]. In this sense, the relationship between  $l$  and  $K$  is similar to the constant delay case. Hence for very slowly fluctuating delay, the Turing instability is also not possible for fixed points.

The other is the case with very fast fluctuating delay. In this case, fluctuating delays can be considered as distributed delays [58]. This is another research area in the study of delay system, but it is out of the scope of this study.

For a case with a general fluctuating delay, the dynamic behavior can be complex. A direct conclusion cannot be reached with analytical calculations. The following text describes some numerical results.

### 4.3.2 Linear stability analysis for the Fisher-KPP equation with delay

For Fisher-KPP equation with delay, the reaction term is the Hutchinson's equation. The partial differential reads as

$$f_t = \frac{\partial f}{\partial u(t)} = a(1 - u(t - \tau)), \quad (4.19)$$

and

$$f_\tau = \frac{\partial f}{\partial u(t - \tau)} = -au(t). \quad (4.20)$$

The fixed point is  $u^* = 1$ . Thus, one obtains  $f_t = 0$  and  $f_\tau = -a$ . Then Eq.(4.12) can be simplified as

$$s = -ae^{-s\tau} - K, \quad (4.21)$$

and the solution of Eq.(4.13) can be rewritten as

$$s = \frac{-K\tau + W(-a\tau e^{K\tau})}{\tau}. \quad (4.22)$$

This formula can be used to investigate the stability of the fixed point  $u^* = 1$ . For instance, when  $K = 0$ , the equation becomes

$$s = \frac{W(-a\tau)}{\tau}, \quad (4.23)$$

which characterizes the stability of the fixed point in Hutchinson's equation. Fig.4.7 indicates how the real part of  $W(-a\tau)$  varies with increasing  $a\tau$ . Here the value of the real part is positive for  $a\tau > \frac{\pi}{2}$ , where the dynamic of the Hutchinson's equation changes from a fixed point to a periodic orbit.

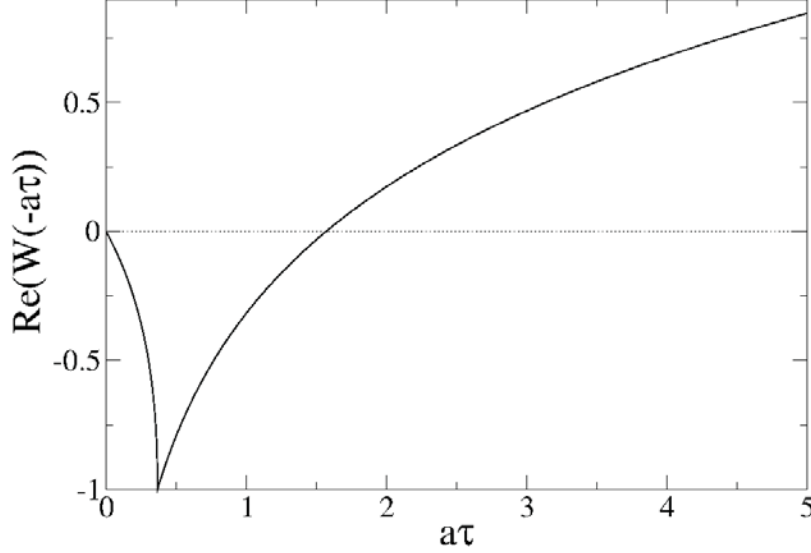


Figure 4.7: The dependence of the real part of  $W(-a\tau)$  on  $a\tau$ .

Because in this considered case, the delay is no longer constant and the investigated state can also be periodic, the Lyapunov exponent cannot be solved from one equation. Hence, with this method, huge calculation resources and time are necessary. Since the maximal Lyapunov exponent is at the core of stability analysis, another numerical method which only calculates the maximal Lyapunov exponent is preferable. Referring back to the description of perturbation  $\delta u(t, s)$  (Eq.(4.9)), one finds that the variation of the perturbation can be decomposed into two parts: One is the local time perturbation  $\delta \hat{u}(t) = \delta u_0 e^{\lambda t}$ . The other is the spatial perturbation  $e^{iks}$ . The governing equation for the local time perturbation  $\delta \hat{u}(t)$  can be obtained as

$$\delta \dot{\hat{u}}(t) = \frac{\partial f}{\partial u(t, s)} \delta \hat{u}(t) + \frac{\partial f}{\partial u(t - \tau(t), s)} \delta \hat{u}(t - \tau(t)) - Dk^2 \delta \hat{u}(t). \quad (4.24)$$

Numerically, the real part of the stability exponents can be calculated as

$$Re(s) = \lim_{T \rightarrow \infty} \frac{1}{T} \log \left| \frac{\delta \hat{u}(T)}{\delta u_0} \right|. \quad (4.25)$$

## 4.4 Results for PDEs

After understanding the influence of fluctuating delays on the behavior of the Hutchinson's equation, one can start investigating the governing equation of the proposed reaction-diffusion system with fluctuating delays, which reads

$$\frac{\partial u(t)}{\partial t} = au(t)(1 - u(t - \tau(t))) + D\Delta u(t). \quad (4.26)$$

To facilitate the comparison of current results with previous results for the Hutchinson's equation with fluctuating delays, the same four different delay fluctuations are used here.

### 4.4.1 Step-shaped delay with $\tau_1 = 1$ , $\tau_2 = 2$ , $T_p = 2$ , and $T_1 = 1$

The study of this system begins with fast fluctuating step-shaped delay with  $\tau_1 = 1$ ,  $\tau_2 = 2$ ,  $T_p = 2$ , and  $T_1 = 1$ . First, the maximal Lyapunov exponents for the considered system with different diffusion coefficients are numerically calculated and shown in Fig.4.8. Periodic boundary conditions are considered and the space size is 10. For the discretization, the time step is chosen to be  $\delta t = 0.01$  and the space step is  $\delta s = 0.2$ . Here a small space size and large discretization steps are chosen to obtain an overview of the dynamics of the considered system with a periodically fluctuating delay. Further investigations with large space size and fine discretization steps will follow.

Fig.4.8 shows that the Lyapunov exponents for the reaction-diffusion system are different under different diffusion coefficients, indicating that Turing instability may appear. Furthermore, for some values of the nonlinear parameter  $a$  the system becomes unstable with the presence of diffusion.

In contrast, in the left side of Fig.4.8 there is a region where the maximal Lyapunov exponents for cases with different diffusion coefficients are identical. This region corresponds to the fixed-point solution. This result indicates that in that region, the Turing instability cannot be found from the fixed point  $u^* = 1$ . Furthermore, before the  $P1 \rightarrow P2$  bifurcation point, there is a region where the maximal Lyapunov exponents are different for different diffusion coefficients. The dynamics for the case without diffusion is also a fixed point there. Here,  $a = 1.3$  is chosen as an example (see the first vertical dotted line in Fig.4.8). The temporal trajectory and the stability exponent of this state are calculated and shown in Fig.4.9. Here

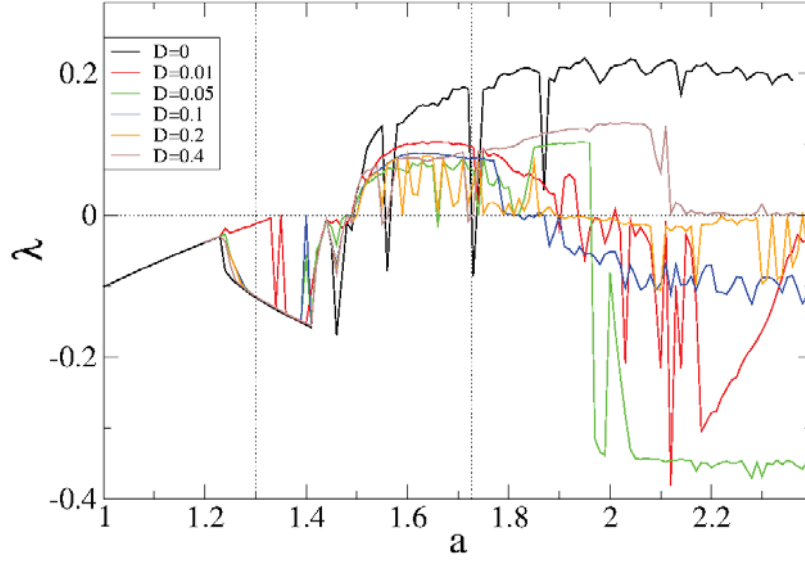


Figure 4.8: Maximal Lyapunov exponents as functions of the nonlinear parameter  $a$  for Eq.(4.26) with a step-shaped varying delay under different diffusion coefficients,  $\tau_1 = 1$ ,  $\tau_2 = 2$ ,  $T_p = 2$ , and  $T_1 = 1$ . The dotted lines indicate the values used for examples in the following text. The discretization is  $\Delta t = 0.01$  for time and  $\Delta s = 0.2$  for space. Random initial conditions and periodic boundary conditions are used, and the space size is 10. Black:  $D = 0$ , red:  $D = 0.01$ , green:  $D = 0.05$ , blue:  $D = 0.1$ , orange:  $D = 0.2$ , and brown:  $D = 0.4$ .

one can obtain a stable fixed point (see Fig.4.9(a)), and in this case, the maximum of the real part of the stability exponent, which is negative, is located at  $k = 0$ . The system is thus always stable under perturbations with any wavenumber  $k$ . Based on the numerical results, the Turing instability is not possible in this case when starting from fixed points.

Now the stable periodic orbits will be investigated. In Fig.4.8, some periodic windows can be found after the  $P1 \rightarrow P2$  bifurcation point for  $D = 0$ . There, the dynamics of Hutchinson's equation with periodic fluctuating delay behave periodically and the maximal Lyapunov exponent is negative. This fulfills one condition of Turing instability, namely, that the state for  $k = 0$  is stable. Next, the Turing instability in such periodic windows is investigated.

In Fig.4.10, the real part of the stability exponent for a periodic orbit as a function of the parameter  $Dk^2$  is shown for the case with  $a = 1.727$  (see the second dotted line in Fig.4.8). Here one can find that for  $Dk^2 = 0$ , the Lyapunov exponent is negative. This means that in the absence of diffusion, the system has a stable periodic orbit. The trajectory and the related



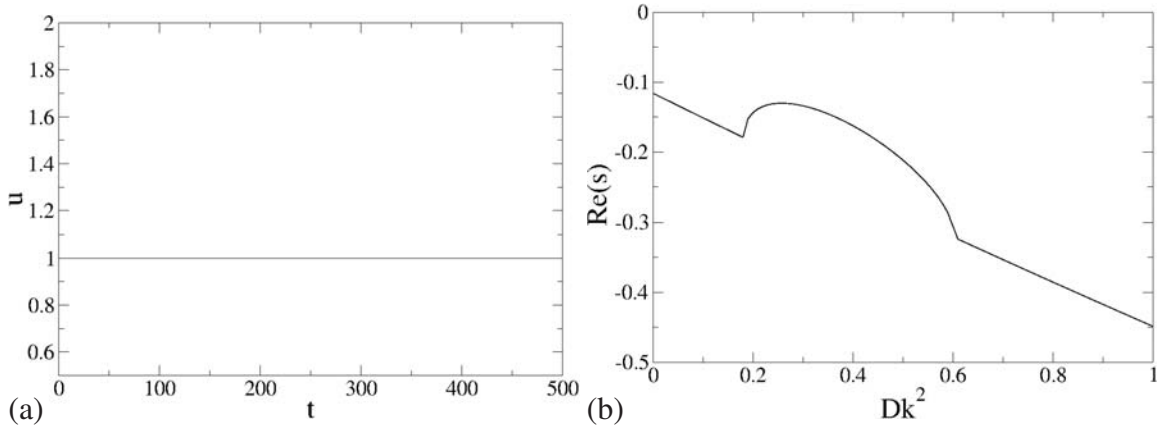


Figure 4.9: (a) A trajectory for Eq.(4.4) with a step-shaped delay,  $\tau_1 = 1$ ,  $\tau_2 = 2$ ,  $T_p = 2$ ,  $T_1 = 1$ , and  $a = 1.3$ . (b) The real part of the stability exponent of a spatial homogeneous state with the same dynamics as in the figure (a) as a function of  $Dk^2$ .

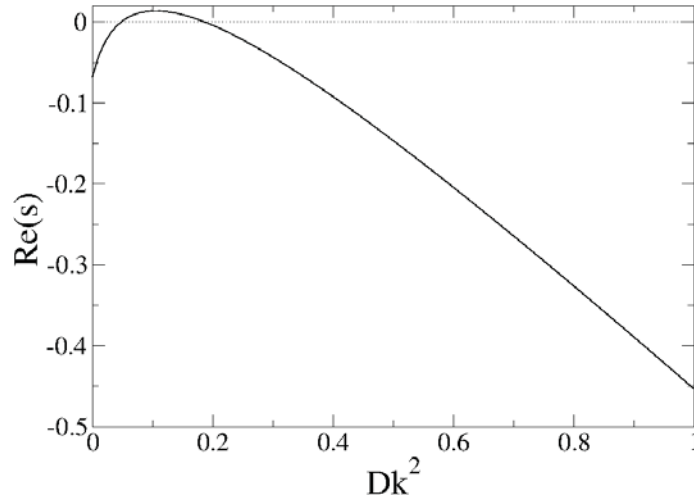


Figure 4.10: The real part of the stability exponent as a function of  $Dk^2$ ,  $a = 1.727$ .

spectrum analysis are shown in Fig.4.11. The state variable varies periodically, and in the corresponding spectrum, the fundamental frequency for the periodic orbit can be found. With increasing  $Dk^2$ , the real part of the stability exponent increases at first and becomes positive at  $Dk^2 \approx 0.04$ . With further increasing  $Dk^2$  a maximum of  $\text{Re}(s)$  is obtained around  $Dk^2 = 0.11$ . After that, the real part of the stability exponent starts to decrease and becomes negative again after  $Dk^2 \approx 0.18$ . This indicates that in the presence of diffusion, the periodic orbit can lose its stability under the influence of perturbations with certain wavenumbers.

#### 4.4. RESULTS FOR PDES

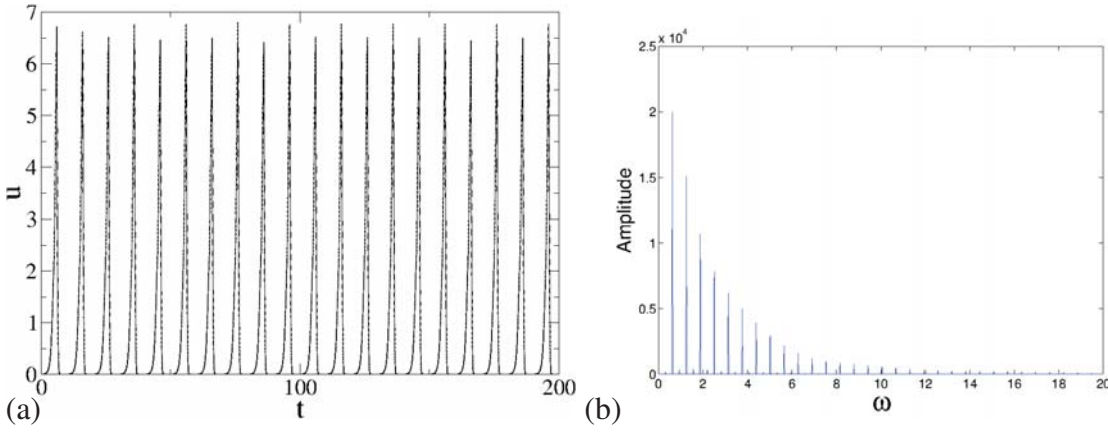


Figure 4.11: Trajectory of the Hutchinson's equation with fluctuating delay and the related spectrum analysis,  $a = 1.727$ .

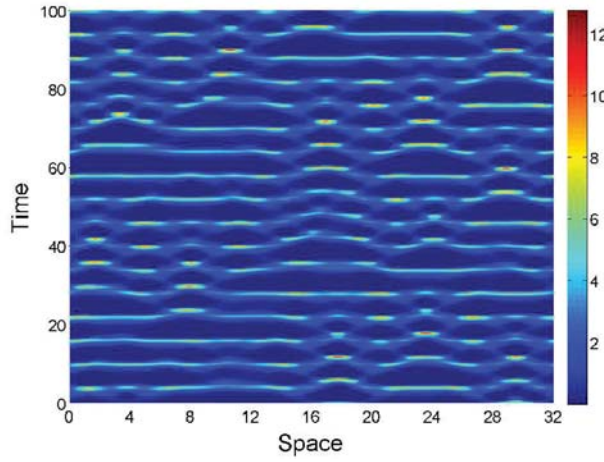


Figure 4.12: Space-Time plot for the considered reaction-diffusion system with periodic fluctuating delay,  $a = 1.727, D = 0.1$ .

In Fig.4.12, an example of the state when the periodic orbit is unstable is shown. Here the nonlinear parameter  $a = 1.727$  and the diffusion coefficient  $D = 0.1$ . The structure is not in an ordered state. The temporal variation of the state at any site is no longer periodic. In Fig.4.13, the temporal variation of the state variable for this structure at three different sites is shown, and additionally, the spectrum analysis for one trajectory is calculated. Here for this state, the local temporal evolution is also not periodic, but chaotic.

Generally, for the Turing instability in spatially one-dimensional systems, when the stable state loses its stability under perturbations with certain specific wavenumbers, one can ex-

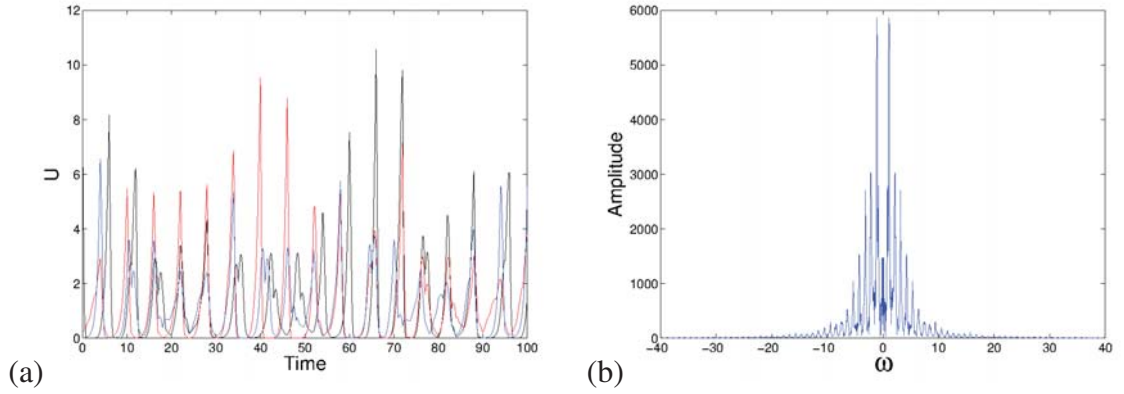


Figure 4.13: (a) Temporal trajectories for Fig.4.12 at three different selected sites. Black:  $x = 5$ , blue:  $x = 17.15$ , and red:  $x = 25$ . (b) Spectrum analysis for the temporal trajectory at  $x = 17.15$ .

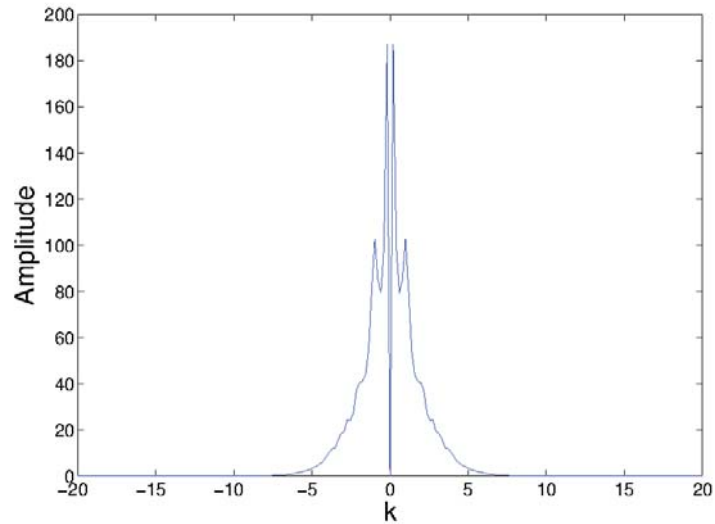


Figure 4.14: Spatial spectrum analysis of the structure in Fig.4.12, averaged over 2000 profiles at different moments in time.

pect that some patterns or structures with these wavenumbers can be observed. The spatial spectrum analysis for the structure in Fig.4.12 is calculated and shown in Fig.4.14. Fig.4.10 shows that for  $D = 0.1$  the wavenumber  $k$  should be between 0.632 and 1.342. But the spectrum analysis does not conform to expectations. The time evolution of state variables at local sites in this state (Fig.4.13(a)) is totally different from the periodic trajectory for the local process without diffusion (Fi.4.11(a)). The reason for this phenomenon is the stability

#### 4.4. RESULTS FOR PDES

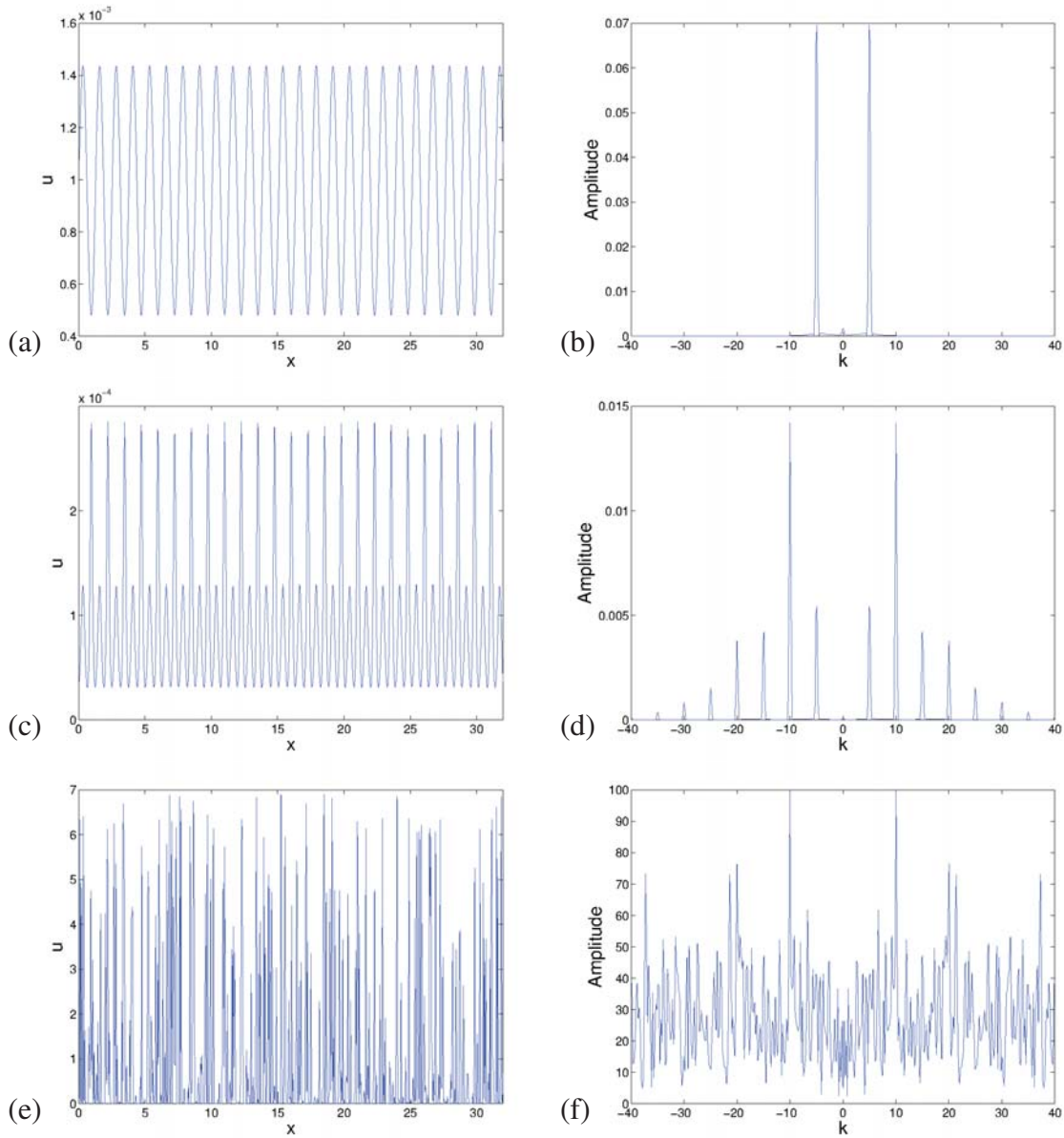


Figure 4.15: Profiles of the spatial state and the corresponding spectrum for the parallel process with a spatial sine-shaped initial perturbation; the initial perturbation is given by  $\delta u(x) = 0.1 \cdot \sin(5x)$  at  $t = 0$ . (a)(b)  $t = 0$ , (c)(d)  $t = 10$ , and (e)(f)  $t = 50$ .

of the Turing pattern and that the states after the Turing bifurcation cannot be determined by the stable state before the Turing bifurcation. In addition, the sensitivity to the initial conditions for periodic orbit also has an influence.

In general, for a Turing instability, the stable state, which loses its stability by perturbations with specific wavenumbers, is a fixed point. The ideal one-dimensional Turing pattern can be described by

$$c = c_0 + Ae^{ik_c x} + \bar{A}e^{-ik_c x}, \quad (4.27)$$

where  $k_c$  is the critical value of the wavenumber  $k$ . In the current case, the stable state studied is periodic orbits. Thus  $c_0$  in Eq.(4.27) is not constant, but dependent on time  $t$  and space  $x$ . Because of the diffusion process, the perturbation can then influence not only the spatial structure, but also the local temporal evolution. For this reason, in addition to the perturbation, there are also phase shifts between different sites in the generated structures or patterns. In this case, in the spatial spectrum analysis, one does not obtain peaks only in the expected wavenumber region. An example is shown in Fig.4.15. Here the phase shift due to initial conditions is studied, and the diffusion coefficient  $D$  is therefore chosen to be 0. The initial condition is the synchronized periodic orbit plus a sine-shaped perturbation  $\delta u = 0.1 \cdot \sin(5x)$ . The state and the corresponding spatial spectrum are shown in Fig.4.15(a)(b). In the beginning, the spatial profiles is a periodic curve, and in the spectrum, peaks can be found at  $k = \pm 5$ . As time continuous, one can observe how the tiny perturbations influence the initial periodic orbit. Fig.4.15(c)(d) shows a complicated periodic profile at  $t = 10$ ; the fundamental wavenumber is still  $k = 5$ . Furthermore, at  $t = 50$ , the spatial profile is no longer periodic, but chaotic (see Fig.4.15(e)(f)). In addition, the temporal evolution at two different sites are plotted (see Fig.4.16). Here the perturbation is observed to affect the phase of the final periodic state, and different perturbations need different time, to achieve the stable state. This can lead to phase shifts between the sites in the spatially extended system, shifts which are responsible for the disordered spatial structure.

Beside the Turing instability in Fig.4.8, one can observe another interesting phenomenon: For a fixed value of the nonlinear parameter  $a$ , first some chaotic states are obtained for a weak diffusion. Then as the diffusion strength increases, stable structures are generated. But if the diffusion strength further increases, chaotic structure occurs again. For instance, for the case with  $a = 1.9$ , a chaotic orbit is obtained for the local process without diffusion. Since the uncoupled local process is already unstable, the discussed bifurcation scenario is not related to the Turing instability. The cause of such phenomena is the stabilization through diffusion and the existence of a multiattractor.

Fig.4.17 shows the relationship between the maximal Lyapunov exponent and the coupling strength  $D$  with fixed  $a = 1.9$ . Six different initial conditions are selected. One can see that

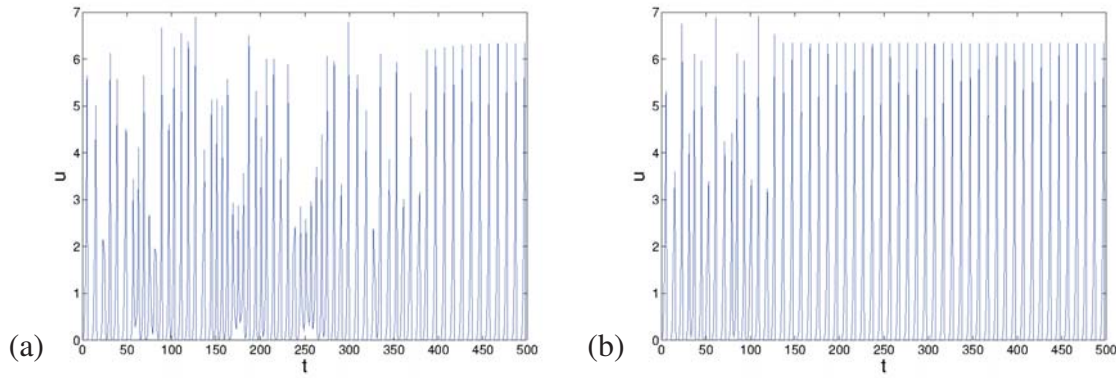


Figure 4.16: Temporal evolution at different sites of parallel process with spatially sine-shaped initial perturbation, (a)  $x = 0.5$ , and (b)  $x = 15.5$ .

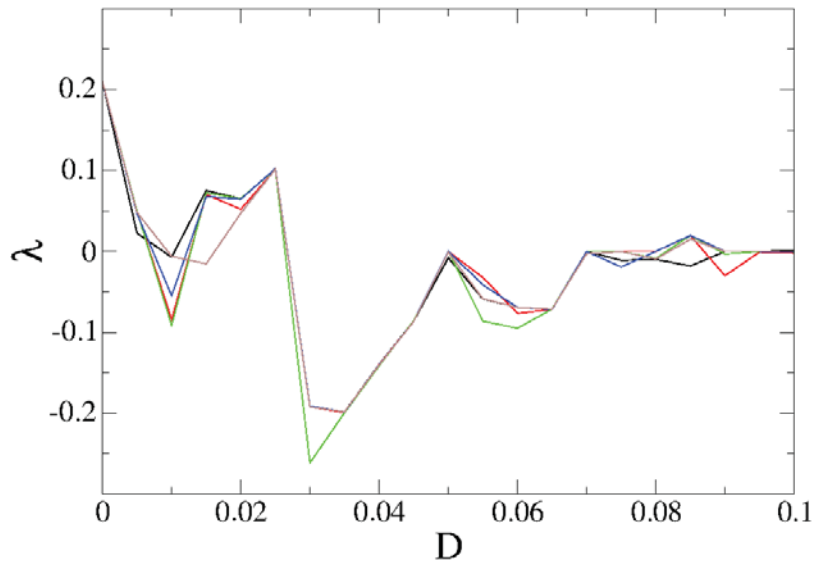


Figure 4.17: Maximal Lyapunov exponents as functions of  $D$  with  $a = 1.9$ . The space size is selected to be 10, and the numerical discretizations are  $\Delta_t = 0.005$  and  $\Delta_s = 0.1$ . Random initial conditions and periodic boundary conditions are considered. Six samples are denoted with different colors.

for a very weak diffusion coefficient, the diffusion cannot stabilize the system completely. The Lyapunov exponent is less than that in the case without diffusion but is still positive. When the diffusion coefficient is further increased, the system can be stable. Under such a situation with different initial conditions, the system may go to different final states. An example is shown in Fig.4.18 with the parameters fixed at  $a = 1.9$  and  $D = 0.1$ . With different initial conditions, two different states are obtained as shown in the figure. The



state on the left side is space-time periodic and has a negative Lyapunov exponent, while the one on the right side contains an irregular band and has a slightly positive Lyapunov exponent  $\approx 10^{-5}$ , which can be treated as  $\lambda \approx +0$ .

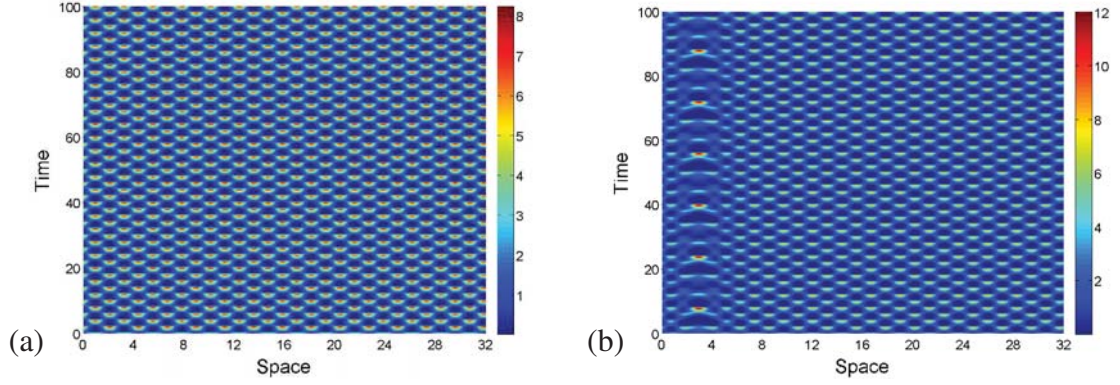


Figure 4.18: Space-time plot of two different final states with the same parameters  $a = 1.9$  and  $D = 0.1$ . (a)  $\lambda = -0.001$  and (b)  $\lambda \approx +0$ .

#### 4.4.2 Step-shaped delay with $\tau_1 = 1$ , $\tau_2 = 2$ , $T_p = 20$ , and $T_1 = 10$

Now a slowly fluctuating case is studied. The fluctuating delay is selected to be  $\tau_1 = 1$ ,  $\tau_2 = 2$ ,  $T_p = 20$ , and  $T_{p1} = 10$ . The Lyapunov exponent as a function of the nonlinear parameter  $a$  for different diffusion coefficients  $D$  is shown in Fig.4.19. The black curve denotes the Lyapunov exponent for the case without diffusion. Here one can see that until the first zero point for the case without diffusion, where the fixed point  $u^* = 1$  is still stable, the curves with different colors, corresponding to the cases with different diffusion coefficients, collapse on a single curve. Thus, the Turing instability of the fixed point cannot be observed in this case. After the threshold for the fixed point  $u^* = 1$ , one can observe many periodic windows for the case without diffusion. In contrast, the Lyapunov exponents for the case with diffusion are different there. Therefore, Turing instability of stable periodic orbits may be found in this case. An example is given to show this possibility.

For  $a = 1.45$ , which is denoted in Fig.4.19 by a dashed line, a periodic orbit is observed for the case without diffusion (see Fig.4.20(a)). From this stable state, the stability exponent can be calculated as a function of  $k$ . Fig.4.20(b) shows the relationship between the real part of the stability exponent and  $Dk^2$ . As can be seen, the real part of the stability exponent is negative for  $Dk^2 = 0$ . And as  $Dk^2$  increases, it becomes positive for  $Dk^2 \in (0.04, 0.21)$ . Two

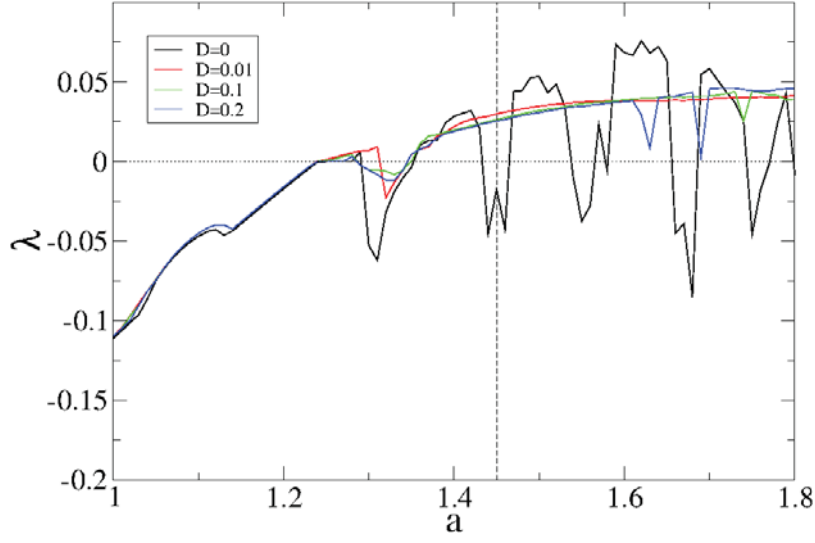


Figure 4.19: Maximal Lyapunov exponents as functions of the nonlinear parameter  $a$  for Eq.(4.26) with a step-shaped varying delay under different diffusion coefficients,  $\tau_1 = 1$ ,  $\tau_2 = 2$ ,  $T_p = 20$ , and  $T_1 = 10$ . The dotted line indicates the values used for examples in the following text. The discretization is  $\delta t = 0.01$  for time and  $\delta s = 0.2$  for space. Periodic boundary conditions and random initial conditions are used, and the space size is 10. Black:  $D = 0$ , red:  $D = 0.01$ , blue:  $D = 0.1$ , green:  $D = 0.2$

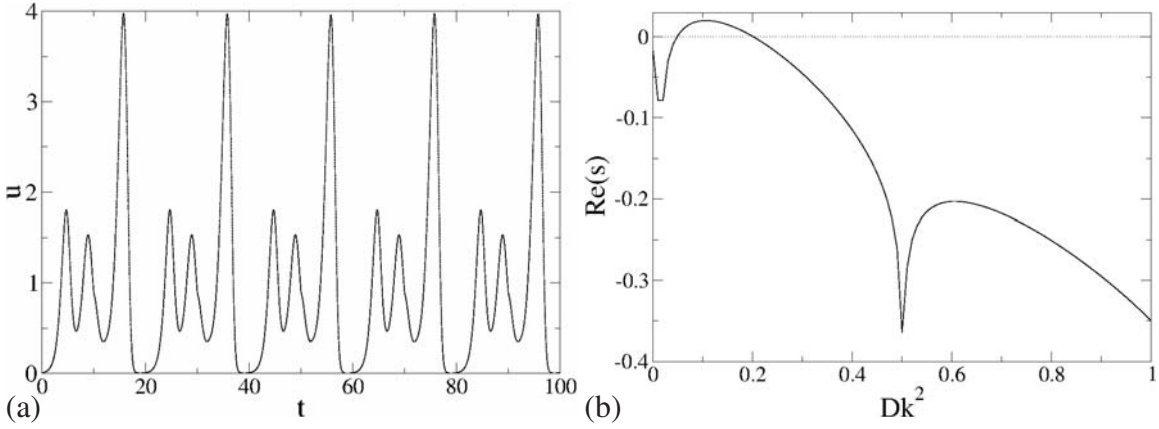


Figure 4.20: (a) A temporal trajectory for Hutchinson's equation with a step-shaped fluctuating delay,  $\tau_1 = 1$ ,  $\tau_2 = 2$ ,  $T_p = 20$ ,  $T_1 = 10$ , and  $a = 1.45$ . (b) The real part of the stability exponent for a spatially homogeneous state with the same dynamics as in (a) as a function of  $Dk^2$ .



examples of the spatio-temporal evolution are shown in Fig.4.21. The diffusion coefficient is selected as  $D = 0.01$  in panel (a) and  $D = 0.1$  in panel (b). Although the evolution of the state is rather irregular here, one can observe some wave-like structures in the plots. When the real part of the stability exponent is positive in a certain region of  $Dk^2$ , for a larger  $D$ , the unstable wavenumber  $k$  is smaller, which means the wavelength will be longer. Fig.4.21 clearly demonstrates this phenomenon. The wave structure in panel (a) has a shorter wavelength than that in panel (b).

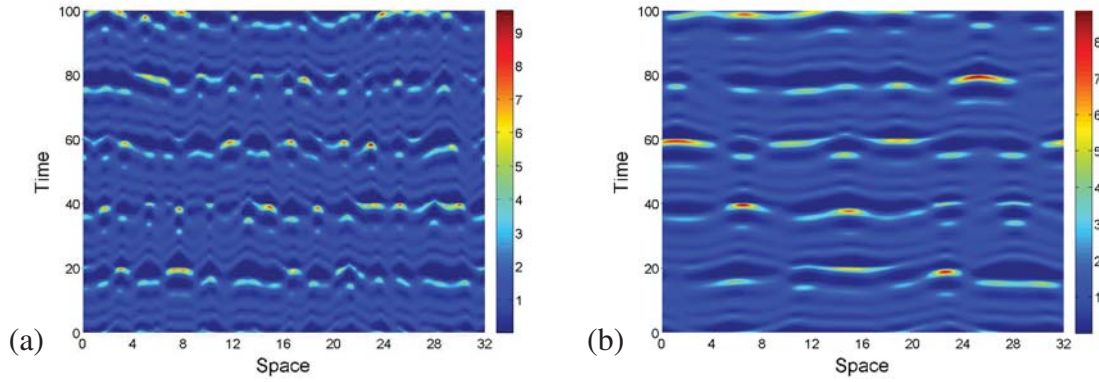


Figure 4.21: Spatio-temporal structures of states after the Turing instability in Fig.4.20 with  $a = 1.45$ . (a)  $D = 0.01$ , and (b)  $D = 0.1$ .

#### 4.4.3 Sine-shaped delay with $\tau_M = 1.5$ , $\tau_A = 0.5$ , and $\omega = \pi$

Now the case with a sine-shaped fluctuating delay is considered. The delay setting  $\tau_M = 1.5$ , and  $\tau_A = 0.5$  is selected, so that the average delay and the maximum and minimum delay lengths are identical to the case with the step-shaped delay. As discussed in the first section, the angular frequency is first chosen to be  $\omega = \pi$ . Fig.4.22 shows the dependence of the maximal Lyapunov exponent on the nonlinear parameter  $a$  in this case for different diffusion coefficients. Similar as in the case with the step-shaped delay, starting from the fixed point  $u^* = 1$ , Turing instability is not possible. The maximal Lyapunov exponent is negative for all diffusion coefficients before the maximal Lyapunov exponent achieves its first zero value. After this bifurcation point, some zigzags are apparent for  $D = 0.01$  and  $D = 0.1$ . As discussed above for the case with a step-shaped delay, such a phenomenon is due to the existence of a multiattractor.

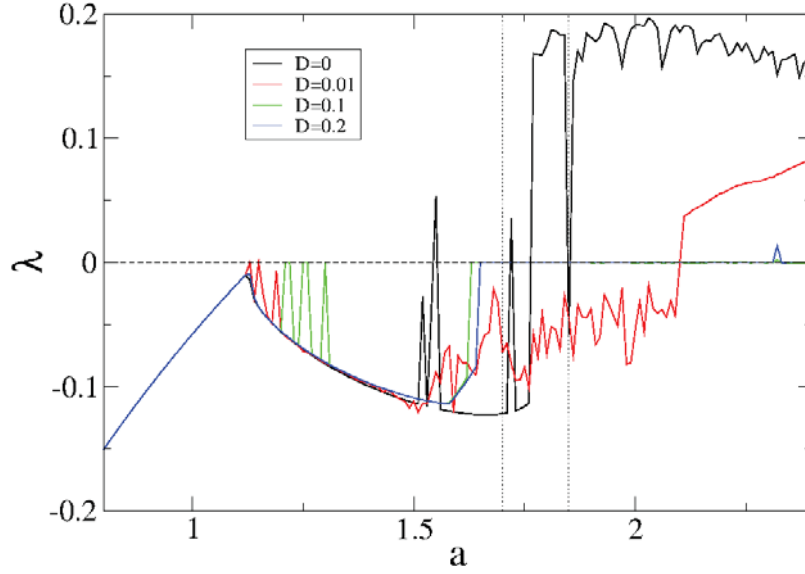


Figure 4.22: Maximal Lyapunov exponent as a function of the nonlinear parameter  $a$  for Eq.(4.26) with a sine-shaped varying delay under different diffusion coefficients,  $\tau_M = 1.5$ ,  $\tau_A = 0.5$ , and  $\omega = \pi$ . The dotted lines indicate the values used for examples in the following text. The discretization of time is selected to be  $\delta t = 0.005$  for the case without diffusion and  $\delta t = 0.01$  for the case with diffusion. And for space,  $\delta s = 0.2$  is chosen. Periodic boundary conditions and random initial conditions are considered, and the space size is 10. Black:  $D = 0$ , red:  $D = 0.01$ , green:  $D = 0.1$ , and blue:  $D = 0.2$ .

However, in Fig.4.22, one cannot find any state which is stable in the absence of diffusion but unstable in the presence of diffusion. Directly after the fixed point loses its stability, a stable region is found for both the case with and the case without diffusion. In the chaotic region of the case without diffusion, although there are some valleys, stable states can hardly be observed. But in such stable regions, the maximal Lyapunov exponents are different for different diffusion coefficients. Thus, from these regions, two examples are chosen to determine the existence of Turing instability.

For the first example, the nonlinear parameter is chosen to be  $a = 1.7$  (see the first vertical dotted line in Fig.4.22). In the absence of diffusion, a stable periodic orbit can be observed (see Fig.4.23(a)). For a large diffusion coefficient, the maximal Lyapunov exponent is zero. The stability exponent of the stable periodic state is calculated, and the relationship between the real part of the stability exponent and  $Dk^2$  is depicted in Fig.4.23(b). One can see that there are no regions where the real part of the stability exponent is positive.

For the second example, the nonlinear parameter is selected to be  $a = 1.85$ . It is located in a periodic window in the chaotic region for the case without diffusion (see the second vertical dotted line in Fig.4.22). For the case without diffusion, a stable periodic orbit can be observed (see Fig.4.24(a)). For this state, the stability exponent is calculated. And the relationship between the real part of the stability exponent and  $Dk^2$  is shown in Fig.4.24(b). One can see that the real part of the stability exponent is always negative for any  $Dk^2$ . Turing instability is thus not possible for this stable periodic state.

Although the real part of the stability exponent is always negative in both of these examples, its maximum is located at a certain  $Dk^2 > 0$ . This means that for certain parameters, the Turing instability for stable periodic orbits is possible.

#### 4.4.4 Sine-shaped delay with $\tau_M = 1.5$ , $\tau_A = 0.5$ , and $\omega = \frac{1}{\pi}$

Now a case with a relatively slowly fluctuating sine-shaped delay is considered. The delay parameters are chosen to be  $\tau_M = 1.5$ ,  $\tau_A = 0.5$ , and  $\omega = \frac{1}{\pi}$ . The length of the period is therefore  $2\pi^2 \approx 19.74$ . First, the relationship between the maximal Lyapunov exponent and the nonlinear parameter  $a$  for different diffusion coefficients is shown in Fig.4.25. Before the maximal Lyapunov exponent achieves the first value, the curves with different colors

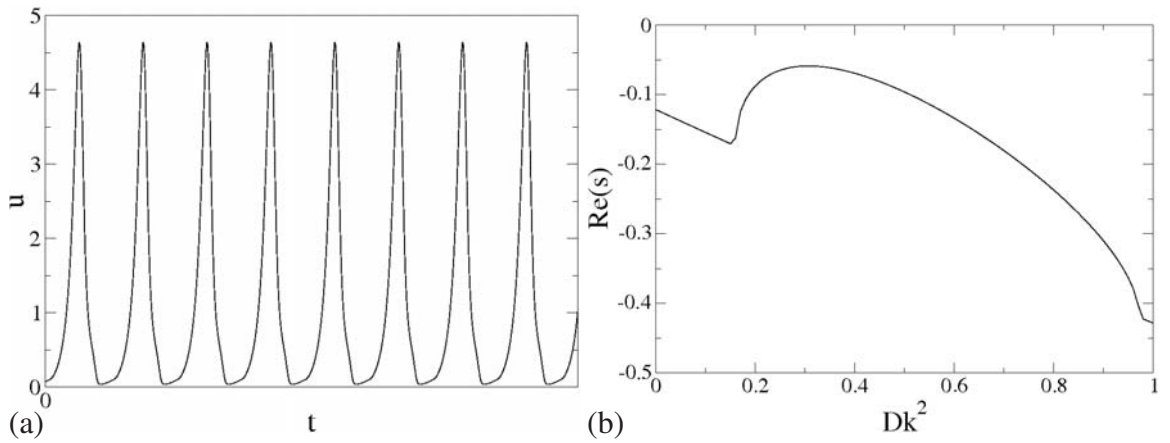


Figure 4.23: (a) A temporal trajectory for Hutchinson's equation with a sine-shaped fluctuating delay,  $\tau_M = 1.5$ ,  $\tau_A = 0.5$ ,  $\omega = \pi$ , and  $a = 1.7$ . (b) The real part of the stability exponent for a spatially homogeneous state with the same dynamics as in (a) as a function of  $Dk^2$ .

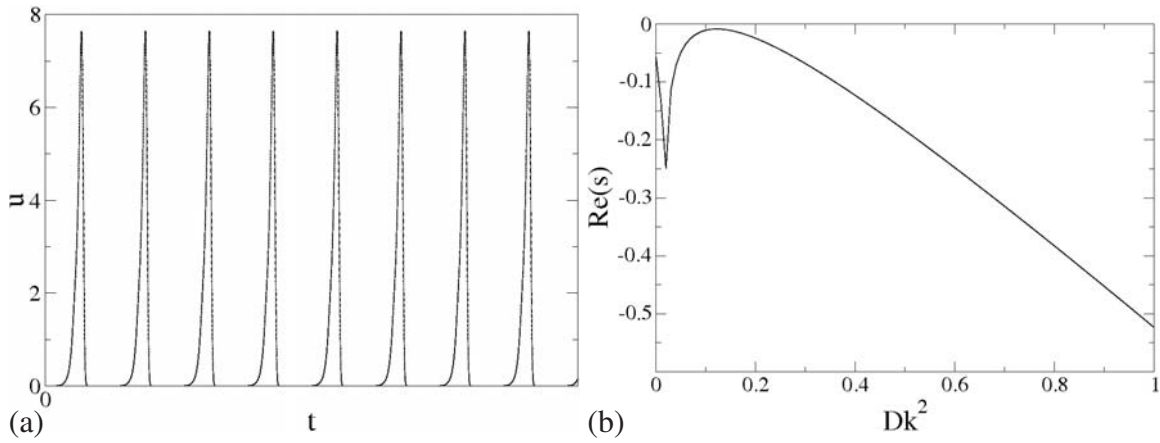


Figure 4.24: (a) A temporal trajectory for Hutchinson's equation with a sine-shaped fluctuating delay,  $\tau_M = 1.5$ ,  $\tau_A = 0.5$ ,  $\omega = \pi$ , and  $a = 1.85$ . (b) The real part of the stability exponent for a spatially homogeneous state with the same dynamics as in (a) as a function of  $Dk^2$ .

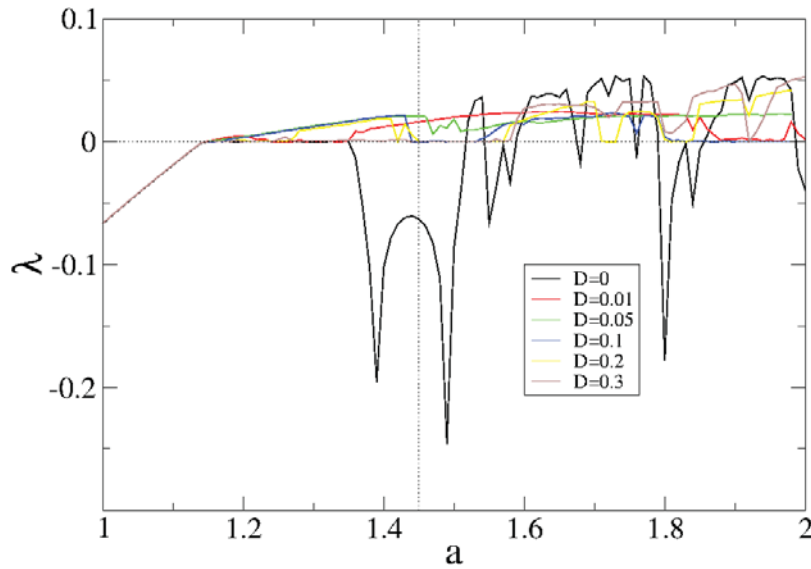


Figure 4.25: Maximal Lyapunov exponents in dependence of the nonlinear parameter  $a$  for Eq.(4.26) with a sine-shaped varying delay under different diffusion coefficients,  $\tau_M = 1.5$ ,  $\tau_A = 0.5$  and  $\omega = \frac{1}{\pi}$ . The dotted line indicates the values used for examples in the following text. The discretization of time is selected to be  $\delta t = 0.01$  for the case with diffusion. And for space  $\delta s = 0.2$  is chosen. Periodic boundary conditions and random initial conditions are considered and the space size is 10. black:  $D = 0$ , red:  $D = 0.01$ , green:  $D = 0.1$ , blue:  $D = 0.2$

collapse to a single curve. Thus, starting from the fixed point  $u^* = 1$ , Turing instability is not possible in this case. After the  $P1 \rightarrow P2$  bifurcation point, one can see some periodic windows for the case without diffusion. In these windows, the case with diffusion can be unstable or have a zero value for the maximal Lyapunov exponent. As a result, the Turing instability may be found.

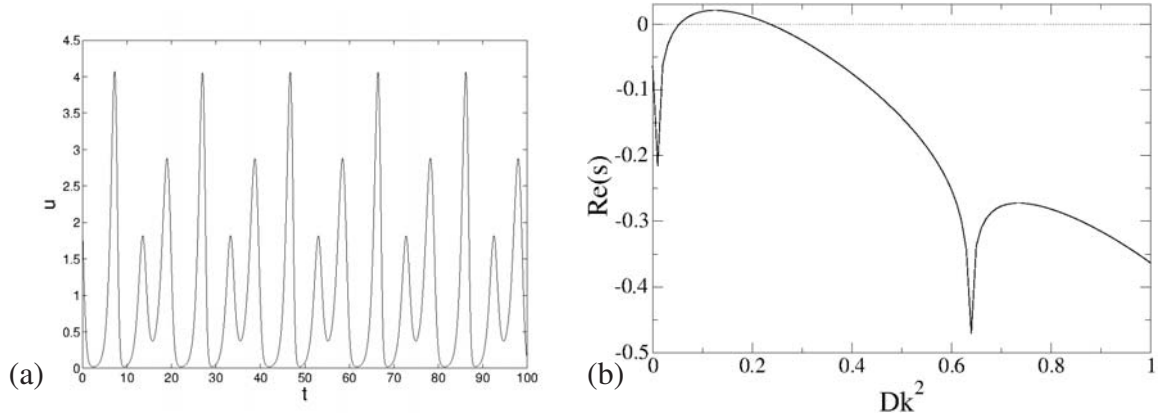


Figure 4.26: (a) A temporal trajectory for Hutchinson's equation with a sine-shaped fluctuating delay,  $\tau_M = 1.5$ ,  $\tau_A = 0.5$ ,  $\omega = \frac{1}{\pi}$ , and  $a = 1.45$ . (b) The real part of the stability exponent of a spatially homogeneous state with the same dynamics as in figure panel (a) as a function of  $Dk^2$ .

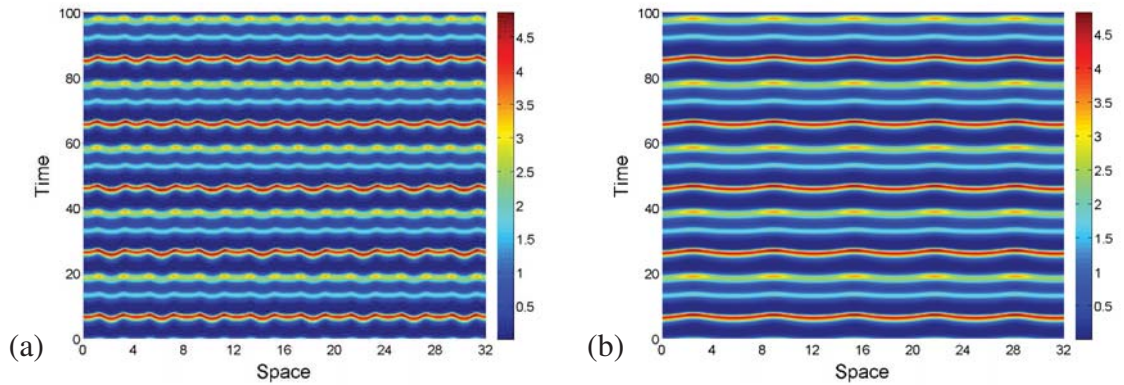


Figure 4.27: Space-time plots of the states after the Turing instability (in Fig.4.25) with  $a = 1.45$ . (a)  $D = 0.01$ , and (b)  $D = 0.1$ .

As an example, the nonlinear parameter is chosen to be  $a = 1.45$ . The maximal Lyapunov exponent is now negative for the case without diffusion. The corresponding stable periodic orbit is shown in Fig.4.26(a). For this state, the stability exponent is calculated. The relationship between the real part of the stability exponent and  $Dk^2$  is shown in Fig.4.26(b). The

real part of the stability exponent is positive only for  $Dk^2 \in (0.05, 0.24)$ . Turing instability can hence be found in this case.

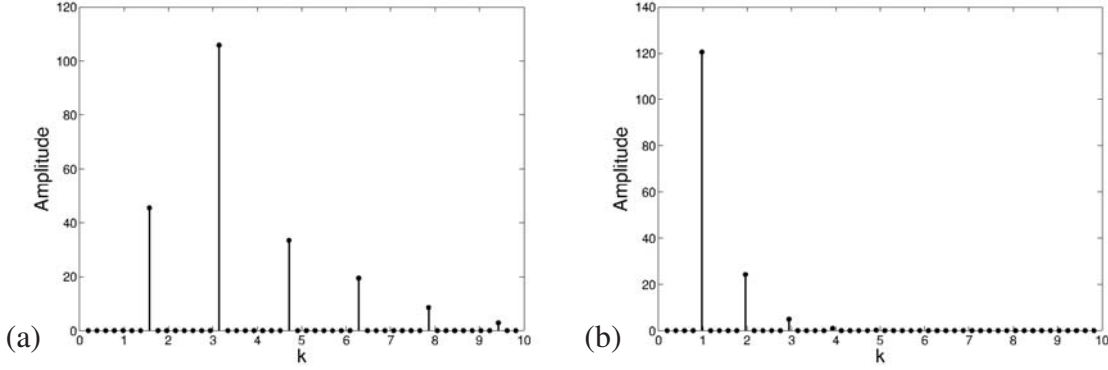


Figure 4.28: Spatial spectra for structures in Fig.4.27. The spectra are obtained by averaging over 10000 spatial profiles of the states. (a)  $D = 0.01$ , and (b)  $D = 0.1$ .

In Fig.4.27, the space-time plots beyond the Turing instability with  $a = 1.45$  are shown. Here different diffusion coefficients are chosen. One is  $D = 0.01$  (Fig.(a)); the other is  $D = 0.1$  (Fig.(b)). Regular spatio-temporal periodic structures are observed for both cases. The maximal Lyapunov exponent is equal to zero for both case. In the spatio-temporal plot, one can see some wave structures. For a larger diffusion coefficient, the wavelength is also larger. As the structure is regular, it is essential to investigate if the spatial wavelength of the structure is related to the positive region of stability exponent. Thus, the spatial power spectra for the structures are calculated and shown respectively in Fig.4.28. The panel (a) is for  $D = 0.01$ , and (b) is for  $D = 0.1$ . Peaks in the spectrum confirm the spatial periodicity in the structure. It is not hard to find out the fundamental wavenumber for the spatial periodicity. Since the real part of the stability exponent is positive for  $Dk^2 \in (0.05, 0.24)$ , the unstable wavenumber  $k$  is expected to be in  $(2.24, 4.90)$  for  $D = 0.01$  and  $(0.71, 1.55)$  for  $D = 0.1$ . It is clear that in both cases, the highest peak lies in the expected region.

## 5 Summary and Outlook

In this dissertation, spatially extended diffusive systems with fluctuating delays are studied. Diffusively coupled map lattices and reaction-diffusion systems are considered as examples. As a novel point, the fluctuating delay in the reaction term of the considered systems is introduced. Through comparing the cases without diffusion and the cases without delay or with constant delay, the influence of fluctuating delays and the influence of spatial extension of the system are investigated.

### Coupled map lattices

The first part of this thesis investigates the coupled map lattice as an example for discrete systems. The delayed logistic map is considered as representative of the local dynamics in this case. To facilitate the introduction of delay, a different type of diffusive coupling is used than that in the typical model introduced by K. Kaneko. Therefore, before starting to investigate the case with a fluctuating delay, the newly considered model was compared with Kaneko's model. The space-time patterns which can be generated in Kaneko's model are also found in the newly considered model. Furthermore, in the new model, one can observe patterns with kinks and chaotic boundaries.

In the cases with a *constant* delay: (1) The  $P1 \rightarrow P2$  bifurcation point was shown to be fixed in the presence of delay. With the help of a master stability function, the mechanism responsible for this is shown analytically. For cases with a constant delay, the bifurcation point is fixed up to a certain value of the coupling strength. (2) In the presence of constant delay, the dynamics after the  $P1 \rightarrow P2$  bifurcation point are simple. Chaotic structures are hardly found in the case with constant delay. (3) Additionally, delays are found to induce spatial movement of the state. While traveling waves can only be found for large coupling



---

strengths in coupled map lattices without delay, in coupled map lattices with a constant delay, a traveling wave can already be found for weak coupling strengths.

After comparing diffusively coupled map lattices without delay and with a constant delay, the case with a periodically fluctuating delay is considered. In this case, only the case with delay as a step-shaped function is considered. Spatially synchronized delay and nonsynchronized delay are considered respectively in the study.

In the cases with a *spatially synchronized periodic* delay: (1) The movement of the first bifurcation point is also studied with the help of the master stability function. Cases with different delay variations are studied. One can find phenomena similar to the phenomena in the cases with a constant delay. The  $P1 \rightarrow P2$  bifurcation point is fixed up to a given coupling strength. (2) Due to the fluctuating delay, the system becomes more complex. Different patterns can be generated in this case. (3) Additionally, two different stable states are found in this case. One is the fully synchronized stable state in which all sites have identical behavior at the same time. The existence and the conditions under which such a state occurs can also be determined with the help of the master stability function. Furthermore, the maximal Lyapunov exponent and the eigenfrequency of the associated Lyapunov vector for such a state can also be determined by the master stability function. The other stable state is spatially nonsynchronized. The related spatio-temporal state looks like patterns with kinks. Temporal orbits at different sites are different and do not behave as the periodic orbit in the case without spatial coupling. Such a state results from the interaction between the spatial coupling and the periodic orbit of a local process. The coupling strength cannot be large. (4) In addition, one can also find traveling waves in this case. When the same properties are used in the case with a constant delay, one can also find traveling waves in the case with a weak coupling. Due to the fluctuation of the delay, it is easy to find a multiattractor in the considered system. For instance, stable periodic state and a traveling wave can coexist.

In the cases with a *spatially nonsynchronized periodic* delay: Due to the phase shift of the delay at different sites, the master stability function method can no longer be used. The bifurcation point is not fixed for different coupling strengths. Fully synchronized stable periodic states cannot be generated, but nonsynchronized stable periodic states can still be found under a weak coupling. Traveling waves can still be observed when the coupling strength is weak.



---

## Reaction-diffusion system

The second part of this thesis investigates reaction-diffusion systems as an example for continuous systems. Delay is introduced into the famous Fisher-KPP equation. In this part, two different types of periodically fluctuating delay are used. One is the step-shaped delay; the other is the sine-shaped delay. These two functions are typical and fundamental for many periodic functions. The reaction term can be considered as Hutchinson's equation with a fluctuating delay.

Since the dynamic behaviors for the Hutchinson's equation with fluctuating delay are not known, in this part, the investigation of this model serves as a starting point. Even for cases where Hutchinson's equation only has equilibrium points or periodic orbits (the maximal Lyapunov exponent is equal to zero), when the delay fluctuates temporally, one can observe chaotic orbits and periodic orbits with negative maximal Lyapunov exponents. Due to the fluctuation of the delay, the Hutchinson's equation becomes nonautonomous. For a nonautonomous system, a periodic orbit can result in a negative value for the maximal Lyapunov exponent.

Comparing the maximal Lyapunov exponent as a function of the nonlinear parameter  $a$  for different diffusion coefficients in the considered model, some values of  $a$  can be found where the system is stable in the absence of diffusion but has a different value of the maximal Lyapunov exponent for some diffusion coefficients. This indicates the possible presence of *Turing instability*. With the introduction of fluctuating delays, a one-component reaction-diffusion system can fulfill the necessary conditions for Turing instability, which is generally only possible in multiple-component reaction-diffusion systems.

The stability exponent as a function of the wavenumber of the spatial perturbations is calculated to determine the existence of a Turing instability. (1) For cases with a *constant* delay, it is possible to analytically prove that starting from fixed points, a Turing instability is not possible. (2) For the case with a *fluctuating* delay, the stability exponent is numerically evaluated. The numerical result indicates that the fixed point will not become unstable in the presence of diffusion. (3) Yet for some stable periodic orbits, Turing instability can be obtained in the presence of diffusion. Because the related stable state is temporally periodic, the related Turing pattern can be unstable even though the occurrence of the Turing instability has been confirmed. Thus, the Turing pattern may not be observed. The perturbations can cause temporal phase shifts for different locations and lead the temporal trajectory in the

---

system with diffusion being far different from the periodic orbit in the system without diffusion. In the case with a sine-shaped delay, some regular Turing patterns are obtained. With the help of spatial spectrum analysis, the numerical results and the stability exponent can be confirmed. Therefore, fluctuating delays provide new possibilities for Turing instability in *one-component* reaction-diffusion systems.

## Outlook

This thesis has investigated simple one-component spatially extended models with fluctuating delay times. For future research multiple-component spatially extended systems could be an interesting topic of research. The spatial coupling could also be anisotropic. Much more complex delay fluctuations and extreme cases of delay fluctuation, such as very fast and very slow fluctuations, could be considered. Furthermore, cases with distributed delay are also a focus in the study of delay systems. The pattern dynamics for a higher dimension are also an interesting direction of research. As this work has proven that a uniform periodic orbit can become unstable via a Turing instability, it is important to study the stability of the Turing pattern of periodic orbits. The possible Turing patterns for a higher dimension, for instance, the striped pattern, hexagonal pattern, and spotted pattern, are also interesting topics for future research.

# Bibliography

- [1] K. Ikeda, H. Daido, and O. Akimoto. Optical turbulence: Chaotic behavior of transmitted light from a ring cavity. *Phys. Rev. Lett.*, 45:709, 1980.
- [2] J. Tlustý, A. Poláček, C. Danek, and J. Špacek. *Selbsterregte Schwingungen an Werkzeugmaschinen*. WEB Verlag Technik, Berlin, 1962.
- [3] S.A. Tobias. *Machine tool vibration*. Blackie, London, 1965.
- [4] R. Bellman. *Adaptive control processes: A guided tour*. Princeton Univ. Press, Princeton, 1961.
- [5] K. Pyragas. Continuous control of chaos by self-controlling feedback. *Phys. Lett. A*, 170:421, 1992.
- [6] L. Glass and M. C. Mackey. *From clocks to chaos, the rhythms of life*. Princeton University Press, Princeton, NJ, 1988.
- [7] D. J. Amit. *Modeling brain function: The world of attractor neural networks*. Cambridge University Press, New York, 1989.
- [8] V. A. Vasil'ev, Y. M. Romanovski, and V. G. Yachno. *Autowave processes*. Nauka, Moscow, 1987.
- [9] M.C. Cross and P.C. Hohenberg. Pattern formation outside equilibrium. *Rev. Mod. Phys.*, 65:851, 1993.
- [10] D. Yue, Q.L. Han, and C. Peng. State feedback controller design of networked control systems. *IEEE Trans. Circuits Syst.*, 51:640, 2004.
- [11] J.D. Cao and J.Q. Lu. Adaptive synchronization of neural networks with or without

- time-varying delay. *Chaos*, 16(013133), 2006.
- [12] J.P. Hespanha, P. Naghshtabrizi, and Y.G. Xu. A survey of recent results in networked control systems. *Proc. IEEE*, 95:138, 2007.
- [13] M. Bestehorn, E. V. Grigorieva, and S. A. Kaschenko. Spatiotemporal structures in a model with delay and diffusion. *Phys. Rev. E*, 70:026202, 2004.
- [14] Z.C. Wang, W.T. Li, and S.G. Ruan. Travelling wave fronts in reaction-diffusion systems with spatio-temporal delays. *J Differ Equations*, 222:185, 2006.
- [15] S.A. Gourley and N.F. Britton. A predator-prey reaction-diffusion system with nonlocal effects. *J Math Biol*, 34:297, 1996.
- [16] A.S. Mikhailov and K. Showalter. Control of waves, patterns and turbulence in chemical systems. *Phys. Rep.*, 425:79, 2006.
- [17] G. Radons, H.L. Yang, J. Wang, and J.F. Fu. Complex behavior of simple maps with fluctuating delay times. *Eur. Phys. J. B*, 71:111, 2009.
- [18] G. Radons, editor. *Materialien zum Forschungsseminar Delay Differential Equations*. Verlag Wissenschaftliche Scripten, Auerbach, 2009.
- [19] A. Otto and G. Radons. Lyapunov spectrum of linear delay differential equations with time-varying delay. *Time Delay Systems*, 9, 2010.
- [20] J. Wang, G. Radons, and H.L. Yang. Dimensional collapse and fractal attractors of a system with fluctuating delay times. *arXiv:1112.1269*, 2011.
- [21] A. Otto, G. Kehl, M. Mayer, and G. Radons. Stability analysis of machining with spindle speed variation. *Adv. Mat. Res.*, 223:600, 2011.
- [22] A. Otto and G. Radons. Application of spindle speed variation for chatter suppression in turning. *CIRP J. Manuf. Sci. Technol.*, 6:102, 2013.
- [23] G. E. Hutchinson. Circular cause systems in ecology. *Ann. N. Y. Acad. Sci.*, 50:221, 1948.
- [24] A.N. Kolmogorov, I. Petrovskii, and N. Piskunov. A study of the diffusion equation

- with increase in the amount of substance and its application to a biology problem. *in Selected works of A.N. Kolmogorov, ed. V.M. Tikhomirov* Kluwer Academic Publishers, London 1991, original work *Bull. Univ. Moscow, Ser. Int. A, 1, 1, 1:242, 1937.*
- [25] R.A. Fisher. The wave of the advance of advantageous genes. *Ann. Eugenics*, 7:353, 1937.
- [26] K. Kaneko. *Theory and applications pf coupled map lattices, nonlinear science, theory and applications*. Wiley, Chichester, 1993.
- [27] A.M. Lyapunov. The general problem of the stability of motion (in russian). *Doctoral dissertation, Univ. Kharkov*, 1892 English translations: (1) Stability of motion, Academic Press, New-York & London, 1966 (2) The general problem of the stability of motion, (A.T. Fuller trans.) Taylor & Francis, London 1992. Included is a biography by Smirnov and an extensive bibliography of Lyapunov's work.
- [28] A. Guinier. *X-ray diffraction. In crystals, imperfect crystals, and amorphous bodies*. W. H. Freeman and Co., 1963.
- [29] D. Chandler. *Introduction to modern statistical mechanics*. Oxford University Press, 1987.
- [30] L. van Hove. Correlations in space and time and born approximation scattering in systems of interacting particles. *Phys. Rev.* 95, 1:249, 1954.
- [31] J.P. Hansen; I.R. McDonald. *Theory of simple liquids*. Academic Press, 1986.
- [32] K. Helbig, W. Just, G. Radons, and H.L. Yang. Dynamic structure factors and Lyapunov modes in disordered chains. *Phys. Rev. E*, 82:026206, 2010.
- [33] Leon W. Couch II. *Digital and analog communications systems (sixth ed. ed.)*. Prentice Hall, New Jersey, 2001.
- [34] D.W. Ricker. *Echo signal processing*. Springer, 2003.
- [35] M.B. Priestley. *Spectral analysis and time series*. London, New York : Academic Press, 1982.
- [36] L.M. Pecora and T.L. Carroll. Master stability functions for synchronized coupled

- systems. *Phys. Rev. Lett.*, 80:2109, 1998.
- [37] Verhulst and Pierre-François. Notice sur la loi que la population poursuit dans son accroissement. *Correspondance mathématique et physique*, 10:113, 1838.
- [38] Verhulst and Pierre-François. Recherches mathématiques sur la loi d'accroissement de la population [mathematical research into the law of population growth increase]. *Nouveaux Mémoires de l'Académie Royale des Sciences et Belles-Lettres de Bruxelles*, 18:1, 1845.
- [39] W. Michiels and S.I. Niculescu. *Stability and stabilization of time-delay systems. An eigenvalue based approach*. SIAM Publications, Philadelphia, 2007.
- [40] R.M. May. Simple mathematical models with very complicated dynamics. *Nature*, 261:459, 1976.
- [41] Wikipedia. Logistic map.
- [42] J. M. Smith. *Mathematical ideas in biology*. Cambridge University Press, 1968.
- [43] D.G. Aronson, M.A. Chory, G.R. Hall, and R. McGehee. Bifurcations from an invariant circle for two-parameter families of maps of the plane: a computer assisted study. *Commun. Math. Phys.*, 83:303, 1982.
- [44] A. M. Turing. The chemical basis of morphogenesis. *Phil. Transact. Royal Soc. B*, 37:237, 1952.
- [45] I. Prigogine and G. Nicolis. *Self-organization in non-equilibrium systems*. Wiley, 1977.
- [46] P. Collet and I. P. Eckmann. *Iterated maps on the interval as dynamical systems*. Birkhauser, 1980.
- [47] E. Ott. *Chaos in dynamical systems*. Cambridge Univ. Press, 2002.
- [48] F.H. Willeboordse. The frozen random pattern in the diffusively coupled logistic lattice. *Phys. Lett. A*, 183:187, 1993.
- [49] H. Weyl. Das asymptotische Verteilungsgesetz der Eigenwerte lineare partieller Dif-

- ferentialgleichungen. *Math. Ann.*, 71:441, 1912.
- [50] H. Wielandt. On eigenvalues of sums of normal matrices. *Pacific J. Math.*, 5:633, 1955.
- [51] A. Knutson and T. Tao. Honeycombs and sums of Hermitian matrices. *N. AMS.*, 48:174, 2001.
- [52] D. Armbruster and G. Dangelmayr. Coupled stationary bifurcations in non-flux boundary value problems. *Math. Proc. Camb. Philos. Soc.*, 101:167, 1987.
- [53] J. F. Heagy, T. L. Carroll, and L. M. Pecora. Synchronous chaos in coupled oscillator systems. *Phys. Rev. E*, 50:1874, 1994.
- [54] S. Lepri, G. Giacomelli, A. Politi, and F. T. Arecchi. High-dimensional chaos in delayed dynamical systems. *Physica D*, 70:235, 1993.
- [55] Jian Wang. Iterierte Abbildungen mit variabler Gedächtnislänge. Master's thesis, TU Chemnitz, 2008.
- [56] E. Ben-Jacob, H.R. Brand, G. Dee, L. Kramer, and J.S. Langer. Pattern propagation in nonlinear dissipative systems. *Physica D*, 14:348, 1985.
- [57] W. van Saarloos. Front propagation into unstable states. ii. linear versus nonlinear marginal stability and rate of convergence. *Phys. Rev. A*, 39:6367, 1989.
- [58] W. Michiels, V. V. Assche, and S.I. Niculescu. Stabilization of time-delay systems with a controlled time-varying delay and applications. *IEEE Trans. Autom. Control*, 50(4):493, 2005.